TECHNICAL TRANSACTIONS
CZASOPISMO TECHNICZNE

CHEMISTRY
CHEMIA

ISSUE 1-Ch (17)
ZESZYT 1-Ch (17)

YEAR 2015 (112)
ROK 2015 (112)

WYDAWNICTWO POLITECHNIKI KRAKOWSKIEJ

TECHNICAL TRANSACTIONS | CZASOPISMO TECHNICZNE

CHEMISTRY | CHEMIA

ISSUE 1-Ch (17) | ZESZYT 1-Ch (17)
YEAR 2015 (112) | ROK 2015 (112)

The authors bear full reponsible for the text, quotations and illustrations
Za tekst, powołania i materiały ilustracyjne odpowiadają autorzy

Basic version of each Technical Transactions magazine is its online version
Pierwotną wersją każdego zeszytu Czasopisma Technicznego jest jego wersja online
www.ejournals.eu/Czasopismo-Techniczne www.technicaltransactions.com www.czasopismotechniczne.pl

Chemistry Series
1-Ch/2015

Editorial Board

TECHNICAL TRANSACTIONS | CZASOPISMO TECHNICZNE
CHEMISTRY | CHEMIA
1-Ch/2015

MONIKA GWADERA, KRZYSZTOF KUPIEC*

MODELING OF ADSORPTION IN A MIXING TANK

MODELOWANIE ADSORPCJI W ZBIORNIKU Z MIESZANIEM

Abstract

Computational models for adsorption in a tank are presented. The approximate model provides the same results as the exact model. The diffusion coefficient of a dye in an adsorbent pellet and the mass transfer coefficient in a fluid phase were determined on the basis of the measurements of dye adsorption on the activated carbon. It was determined how the fraction of the resistance to mass transfer in the fluid to the overall mass transfer resistance changes during adsorption. It was found that, for the examined system, the main resistance to mass transfer is located in the liquid phase.

Keywords: adsorption kinetics, resistance to mass transfer

Streszczenie

Przedstawiono modele obliczeniowe adsorpcji w zbiorniku. Stwierdzono, że model przybliżony daje identyczne wyniki z modelem ścisłym. Na podstawie przeprowadzonych pomiarów adsorpcji barwnika na węglu aktywnym określono wartość współczynnika dyfuzji w ziarnie oraz współczynnika wnikania masy w fazie ciekłej. Wyznaczono czasowe zmiany udziału oporu wnikania masy w fazie ciekłej w sumarycznym oporze przenoszenia masy w trakcie adsorpcji. Stwierdzono, że dla badanego układu główny opór przenoszenia masy jest zlokalizowany w fazie ciekłej.

Słowa kluczowe: kinetyka adsorpcji, opór przenoszenia masy

DOI: 10.4467/2353737XCT.15.100.4048

* Ph.D. Eng. Monika Gwadera, Ph.D. Eng. Krzysztof Kupiec, prof. CUT; Faculty of Chemical Engineering and Technology, Cracow University of Technology.

Nomenclature

Bi (= $k_l R/(K\rho_p D_s)$)	–	Biot number
C	–	adsorbate concentration in solution [kg/m^3]
C_0	–	initial adsorbate concentration in solution [kg/m^3]
D_s	–	solid diffusion coefficient [m^2/s]
$J_0(a)$	–	Bessel function of the first kind of order 0
$J_1(a)$	–	Bessel function of the first kind of order 1
k_l	–	mass transfer coefficient in liquid phase [m/s]
K	–	adsorption equilibrium constant [m^3/kg]
L	–	characteristic pellets dimension [m]
m_s	–	adsorbent mass [kg]
q_m	–	adsorbate concentration in solid phase [kg adsorbate/kg solid]
q_{m0}	–	adsorbate concentration in solid phase in equilibrium with C_0 [kg adsorbate/kg solid]
Q	–	dimensionless adsorbate concentration in solid phase
R	–	pellet radius [m]
t	–	time [s]
V	–	volume of liquid solution [m^3]
x	–	spatial coordinate [m]
Y	–	dimensionless adsorbate concentration in liquid phase
α	–	adsorbent load factor
β_i	–	roots of algebraic equation
η	–	dimensionless spatial coordinate
ρ_p	–	density of pellets [kg/m^3]
τ	–	dimensionless time
ζ	–	geometric factor
χ	–	fraction of resistance to mass transfer in liquid phase
1 (index)	–	pellet surface

1. Introduction

The presence of dyes from different branches of industry in water is a significant environmental problem. Even if a dye concentration is low, it affects the organisms living in water. Some of the dyes are carcinogenic or mutagenic.

Wastewater containing dyes comes from the following industries: food industry, fat industry, cosmetics industry and plastics industry. Such wastewater changes the color of water in a receiver, which leads to a reduction of its usefulness in industry and in households. The existing color reduces light transmittance, and thus interferes with the growth and biological activity of bacteria and delays the self-cleaning process. Furthermore, coloring substances consume oxygen dissolved in water, which results in chemical and biological changes of the aquatic environment. The consequence of dyes decomposition is the appearance of substances that are toxic, carcinogenic and mutagenic to living organisms.

Adsorption on activated carbon is one of the most effective and reliable technologies for the treatment of water and wastewater that contain hazardous compounds [1]. It is necessary to know the equilibrium and kinetics of adsorption in order to design an efficient installation for adsorption on activated carbon.

Adsorption in a liquid phase can be performed, for example, by contacting a mixture containing an adsorbate with adsorbent pellets in a mixing tank. Adsorption in a tank is an important step in the treatment of drinking water.

Most commercial adsorbents are porous and the rate of discharge of a component from a solution is limited by the adsorbate molecules diffusion to the interior of adsorbent pellets. An adsorbate must, however, first be transferred from the bulk of the fluid to the surface of a pellet. The relationship between internal and external mass transfer resistance is expressed by the Biot number Bi. When the resistance in a fluid phase can be neglected, then Bi $\rightarrow \infty$; otherwise Bi has a finite value.

The purpose of this paper is to present the principles of modeling of adsorption in a tank of finite volume and to analyze the mass transfer resistance during this process. An exact model of the process based on a differential equation containing partial derivatives and an approximate model based on a system of ordinary differential equations are presented. Contributions of mass transfer resistances in both phases of the system were determined on the basis of the study of kinetics of dye adsorption on activated carbon. The dominant mass transfer resistance must be known for modeling and design of adsorption processes. Systems with linear adsorption equilibrium and adsorbent pellets with the shape of an infinite plate, infinite cylinder and sphere are considered.

2. An exact model of adsorption in a finite-volume tank

The equation of diffusion and adsorption will be presented in a dimensionless form. The dimensionless quantities are defined as follows: the concentration of an adsorbate in a pellet $Q = q_m/q_{m0}$, the average concentration in a pellet $\bar{Q} = \bar{q}_m/q_{m0}$, the spatial coordinate in a pellet $\eta = x/L$, time $= D_s t/L^2$, the concentration in a fluid $Y = C/C_0$. The formula that relates Q and $\bar{Q}$ has the form:

$$\bar{Q} = (\zeta + 1)\int_0^1 \eta^{\zeta} Q \, d\eta \tag{1}$$

where the geometric factor is: for a slab $\zeta = 0$, for a cylinder $\zeta = 1$, for a sphere $\zeta = 2$. The equation of diffusion and adsorption is:

$$\frac{\partial Q}{\partial \tau} = \frac{\partial^2 Q}{\partial \eta^2} + \frac{\zeta}{\eta} \cdot \frac{\partial Q}{\partial \eta} \tag{2}$$

The initial condition for pellets that do not contain an adsorbate:

$$\tau = 0 \qquad Q = 0 \tag{3}$$

One of the boundary conditions refers to the symmetry of a pellet:

$$\eta = 0 \qquad \frac{\partial Q}{\partial \eta} = 0 \tag{4}$$

The form of a boundary condition at the surface of a pellet depends on the relation between the internal and external mass transfer resistance. When the resistance outside a pellet can be neglected (Bi $\rightarrow \infty$), the condition has the form:

$$\eta = 1 \qquad Q = Y_b \tag{5}$$

If the external resistance must also be taken into account, the boundary condition at the pellet surface is:

$$\eta = 1 \qquad \frac{\partial Q}{\partial \eta} = \mathrm{Bi}\left(Y_b - Y\right) \tag{6}$$

Values of Y_b are dimensionless concentrations of an adsorbate in the bulk of a fluid phase. For Bi $\rightarrow \infty$ the concentration is constant i.e. it does not change with time. Then it is $Y_b = 1$ for adsorption and $Y_b = 0$ for desorption with an inert.

When a tank that contains a liquid has a finite volume, then concentration of an adsorbate in the liquid changes during adsorption. The model of the process must include not only the balance for a solid phase but also the balance of an adsorbate in a fluid. This equation has the form:

$$\bar{Q} = \alpha\left(1 - Y\right) \tag{7}$$

where the adsorbent load factor is given by the formula:

$$\alpha = \frac{V}{m_s K} \tag{8}$$

For the linear equilibrium of adsorption it can be proved that the ratio of mass of adsorbed component at a given moment m_t to the mass of adsorbed component at equilibrium m_∞ is:

$$\frac{m_t}{m_\infty} = \frac{\bar{Q}}{\lim\limits_{\tau \to \infty} \bar{Q}} = \frac{1+\alpha}{\alpha}\ \bar{Q} \tag{9}$$

For Bi → ∞ the analytical solutions for all the considered shapes can be written in the generalized form [2, 3, 7]:

$$\frac{m_t}{m_\infty} = 1 - \sum_{i=1}^{\infty} \frac{2(1+\zeta)\alpha(1+\alpha)}{(1+\zeta)^2 + (1+\zeta)^2\alpha + \alpha^2\beta_i^2} \exp\left(-\beta_i^2\tau\right) \tag{10}$$

where β_i are consecutive roots of the following algebraic equations. For a slab:

$$\tan\beta + \alpha\beta = 0 \tag{10a}$$

For a cylinder:

$$\alpha\beta J_0(\beta) + 2J_1(\beta) = 0 \tag{10b}$$

For a sphere:

$$\tan\beta - \frac{3\beta}{3+\alpha\beta^2} = 0 \tag{10c}$$

From formulas (7), (9) and (10) one can obtain:

$$Y = 1 - \frac{1}{1+\alpha}\left[1 - \sum_{i=1}^{\infty} \frac{2(1+\zeta)\alpha(1+\alpha)}{(1+\zeta)^2 + (1+\zeta)^2\alpha + \alpha^2\beta_i^2} \exp\left(-\beta_i^2\tau\right)\right] \tag{11}$$

For short times the rates of convergence of the infinite series in equations (10), (11) are slow and a large number of terms must be taken into account, which is burdensome. However, in such cases, some other forms of solutions that do not contain infinite series may be used [2].

For Bi < ∞, i.e. when the resistances to mass transfer are in both phases, the analytical solution for adsorption in a finite volume tank is known only for a sphere.

Temporal variations of dimensionless concentrations of an adsorbate in a solid and liquid phases for different values of α are presented in Fig. 1. The graph refers to spherical pellets and to the lack of the mass transfer resistance in a fluid. The courses (in the form of symbols) were determined on the basis of relations (11) and (7). After some time, the system reaches equilibrium and the dimensionless concentrations become equal to each other. The values of the equilibrium concentrations depend on the coefficient α.

The Bessel functions are present in the solution for an infinite cylinder instead of trigonometric functions occurring in the solutions for a slab and a sphere (eq. (10b)). Some difficulties lie in finding the roots of an equation that contains the Bessel function which are periodic functions with variable period. To find a root, the range in which it will be searched for should be determined. In order to do it, the zeroes of the Bessel function of order zero $J_0(\beta) = 0$ should be known. The problem is illustrated in Fig. 2. The curves for the functions y_1 and y_2 defined as follows:

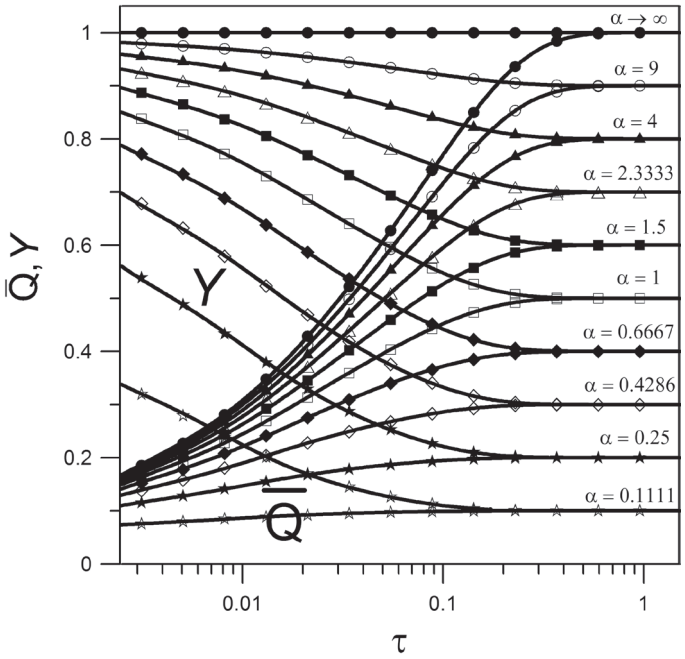

Fig. 1. The effect of the parameter α on adsorbate concentrations in both phases in a finite-volume tank. Spherical pellets, Bi → ∞

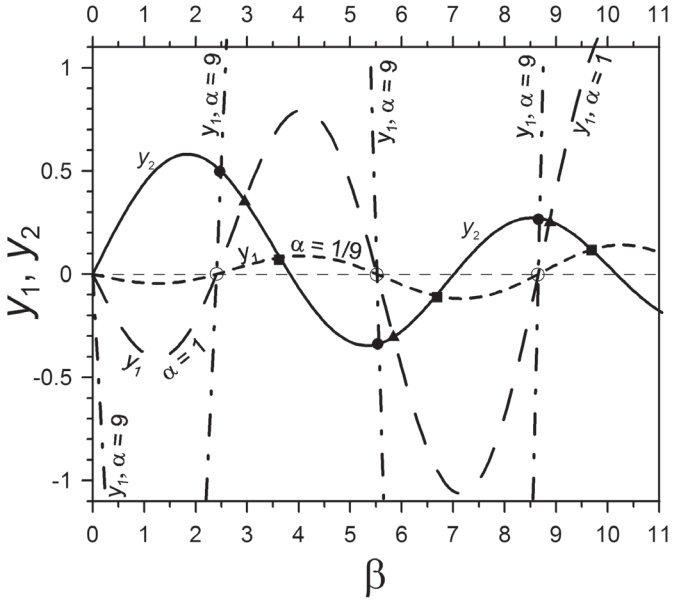

Fig. 2. The roots of formula (10b)

$$y_1 = -\frac{\alpha}{2}\beta J_0(\beta) \tag{12a}$$

$$y_2 = J_1(\beta) \tag{12b}$$

are presented.

The shape of the function y_1 depends on the value of the parameter α; in Fig. 2 the graphs for α = 1/9, α = 1 and α = 9 were presented. The zeroes of function y_1 (not shaded points) coincide with the zeros of function $J_0(\beta)$. They are equal to: β_1^0 = 2.4048, β_2^0 = 5.5201; β_3^0 = 8.6537 etc. Therefore, the first solution of equation (10b) is in the range (2.4048, 5.5201), the second is in the range (5.5201, 8.6537) etc. Abscissae of the points of intersection of functions $y_1(\beta)$ and $y_2(\beta)$ are the sought roots of equation (10b) (shaded points). For example, for α = 1/9 the first solution is 3.6374, for α = 1 the first solution equals 2.9496, and for α = 9 the first solution is 2.4922.

3. Computational relationships for the approximate model

In the approximate model of adsorption kinetics, based on the continued fractions approximation, the general form of the kinetic equation is as follows:

$$\dot{\mathbf{x}} = \mathbf{d}^{-1}\left(\mathbf{a} - \frac{1}{\alpha}\mathbf{bq}\right)\mathbf{x} + \mathbf{d}^{-1}\mathbf{b} \tag{13}$$

Hence, a system of ordinary differential equations must be solved.

The vector **b** is defined in the form: $\mathbf{b} = [\zeta + 1, \zeta + 1, ..., \zeta + 1]^T$. The elements of matrix **a** are: $a_{ij} = -p_i q_j$ for $j > i$, $a_{ij} = -p_j q_j$ for $j < i$ and $a_{ij} = -p_i q_i$ for $j = i$, where p_i and q_i are defined as follows: $p_i = 2i^2 - i + \zeta i$, $q_i = 4i + \zeta - 1$ where $i = 1, 2, ..., n$. The elements of matrix **d** depend on the Biot number: $d_{ij} = q_j/\mathrm{Bi}$ for $j \neq i$ and $d_{ij} = 1 + q_j/\mathrm{Bi}$ for $j = i$. The number of equations in system (13) is the order of approximation n; the greater the order, the higher accuracy of approximation.

System of equations (13) has to be solved with the initial condition which for a pellet that do not contain an adsorbed component has the form:

$$\tau = 0 \qquad \mathbf{x} = 0 \tag{14}$$

As a result of solving system (13), one gets a vector function $\mathbf{x}(\tau)$ on the basis of which a scalar function $\bar{Q}(\tau)$ can be determined:

$$\bar{Q} = \mathbf{qx} \tag{15}$$

The form of a boundary condition at the pellet surface depends on the values of parameters α and Bi. Possible cases are discussed below. Since a linear form of adsorption equilibrium was assumed, it is $Q_1 = Y_1$ in each case.

In the simplest system, a pellet is contacted with a fluid of an infinite volume ($\alpha \to \infty$), which is mixed so intensely that the external mass transfer resistance can be neglected ($Bi \to \infty$). In this case, the concentration of an adsorbate in a fluid does not change over time and space. Therefore, it might be assumed that the surface of a pellet contacts with a fluid which has a constant and known concentration. The concentration at the pellet surface Q_1 (in equilibrium to the concentration of an adsorbate in a fluid that has a direct contact with the pellet surface) is also constant (Fig. 3a). The following equality is valid for such a case:

$$Q_1 = Y_b = 1 \tag{16}$$

The approximate kinetic model simplifies to the form:

$$\dot{\mathbf{x}} = \mathbf{a}\mathbf{x} + \mathbf{b} \tag{17}$$

Such a model was used by Lee and Kim [9].

For adsorption in a finite-volume tank ($\alpha < \infty$), the adsorbate concentration in a fluid contacting with the pellet surface changes over time, which results from changes of the adsorbate concentration in the bulk of a fluid. When diffusion resistance in a fluid is negligible ($Bi \to \infty$), the concentration of a component in a fluid at the solid-fluid boundary is equal to the bulk concentration (Fig. 3b). The following relationship is valid:

$$Q_1 = Y_b \le 1 \tag{18}$$

while the approximate kinetic model is:

$$\dot{\mathbf{x}} = \left(\mathbf{a} - \frac{1}{\alpha}\mathbf{b}\mathbf{q} \right)\mathbf{x} + \mathbf{b} \tag{19}$$

Such a form of a kinetic model was used in the paper [7].

When mass transfer resistance in the fluid phase cannot be neglected ($Bi < \infty$), the concentrations of an adsorbate in the bulk of a fluid and at the phase boundary are not equal (for adsorption it is: $Y_1 < Y_b$). If the process is conducted in a tank of an infinite volume ($\alpha \to \infty$), the concentration of an adsorbate in the bulk of a fluid does not change over time ($Y_b = 1$). However, the concentration at the surface $Y_1 = Q_1$ varies over time. For such a case (Fig. 3c), the following relationship is valid:

$$Q_1 \le Y_b = 1 \tag{20}$$

The following system of equations constitutes the approximate kinetic model:

$$\dot{\mathbf{x}} = \mathbf{d}^{-1}\mathbf{a}\mathbf{x} + \mathbf{d}^{-1}\mathbf{b} \tag{21}$$

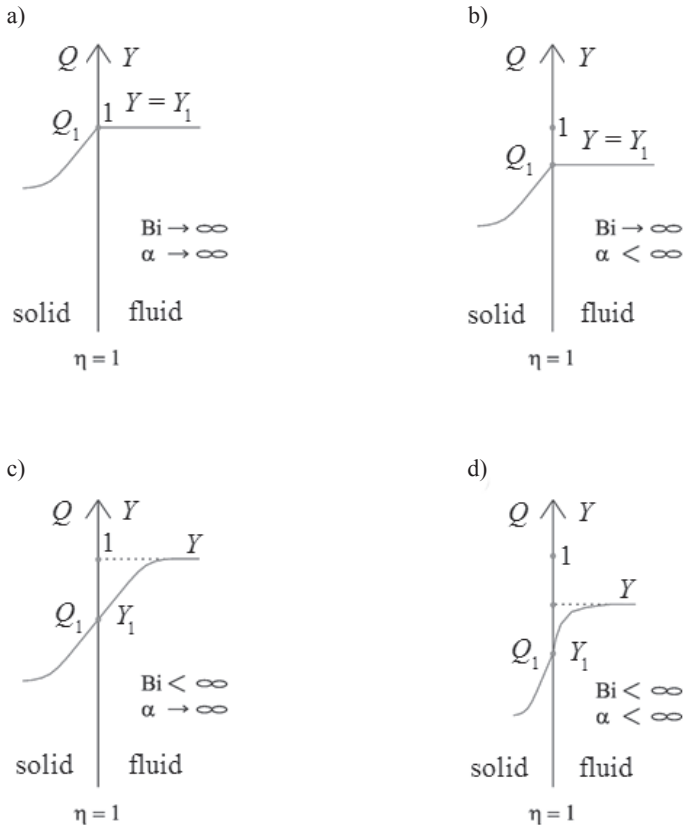

Fig. 3a, b, c, d. Distribution of concentrations at the solid-fluid boundary for different combinations of Bi and α

Such a case was considered in the paper [6].

The most difficult case is when the mass transfer resistance in the liquid phase is significant and the bulk concentration changes. This occurs when adsorption is conducted in a finite-volume tank ($\alpha < \infty$) and the intensity of fluid stirring does not ensure that the bulk concentration and the phase boundary concentration are equal ($Bi < \infty$). The changes of the surface concentration result from the mass transfer resistance in a fluid and from reduction of an adsorbate concentration in the bulk of a fluid because of adsorption. It can be written that (Fig. 3d):

$$Q_1 \le Y_b \le 1 \tag{22}$$

The system of equations (13) without any simplifications is the approximate kinetic model.

Calculations were conducted to verify whether the approximate model gives results consistent with the exact model. A number of calculations are presented in the works of authors [4, 5, 6, 8]. The results of an exemplary calculation are also presented in Fig. 1.

The solid lines in this Figure denote values obtained on the basis of the approximate model. The compliance between this values and the values designated on the basis of an analytical solution (symbols) is very good.

4. Mass transfer resistance

In order to intensify the adsorption process, one should reduce the mass transfer resistance. The overall resistance is influenced by partial resistances in a fluid phase and adsorbent pellets. These resistances are connected in series so the greater resistance, which has the main impact on the overall resistance, should be reduced. If the main resistance is in the fluid it can be reduced e.g. by the increase of the flow velocity. When the resistance in pellets dominates, one should consider reduction of pellets size. By knowing the values of the mass transfer coefficient in a fluid and the diffusion coefficient in pellets, one can determine the contribution (fraction) of each resistance to the overall resistance and in this way the dominant resistance can be determined. However, it should be noticed that mass transfer during adsorption is usually a transient process so the relations between resistances change when adsorption is conducted.

For pellets with the considered shapes, the dimensionless equation of mass transfer in a liquid phase has the form:

$$\frac{d\bar{Q}}{d\tau} = (1+\zeta)\,\mathrm{Bi}\,(Y - Y_1) \tag{23}$$

The rate of mass transfer was determined by differentiation of equation (15):

$$\frac{d\bar{Q}}{d\tau} = \mathbf{q}\dot{\mathbf{x}} \tag{24}$$

From the above relationships, a concentration $Y_1 = Q_1$ at the phase boundary was calculated:

$$Y_1 = Y - \frac{1}{(1+\zeta)\,\mathrm{Bi}}\,\mathbf{q}\dot{\mathbf{x}} \tag{25}$$

In Fig. 4, the concentrations for adsorption in a finite-volume tank with mass transfer resistance in both phases are presented. The graph refers to spherical pellets and Bi = 10. Temporal variations in a liquid phase Y, solid phase $\bar{Q}$ and at the phase boundary Y_1 are presented. Since there is equilibrium at the phase boundary, so it is $Y_1 = Q_1$. Moreover the following relationships are valid: $Y > Y_1$ and $Q_1 > \bar{Q}$.

A stream of an adsorbed component (component that is transferred from a liquid to a solid phase) is proportional to the mass transfer driving force and inversely proportional to the mass transfer resistance R. Comparison of the stream of a component transported in a liquid and the stream transferred between both phases leads to the formula:

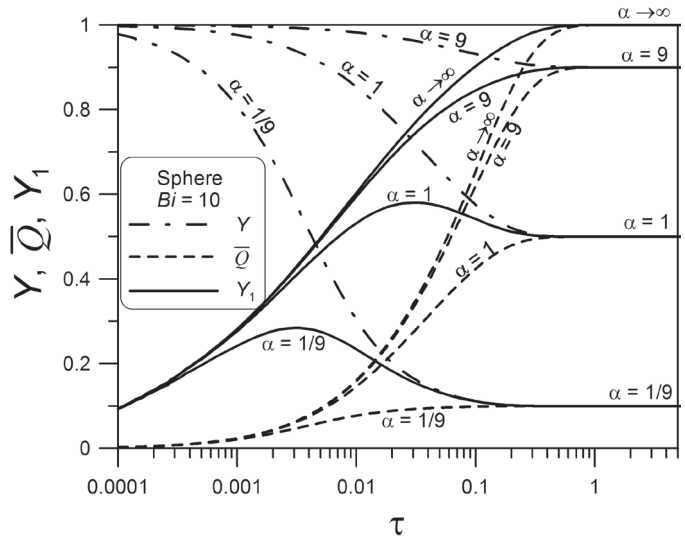

Fig. 4. Temporal variations of concentrations in a fluid Y, pellets $\overline{Q}$ and at the phase boundary $Y_1 = Q_1$

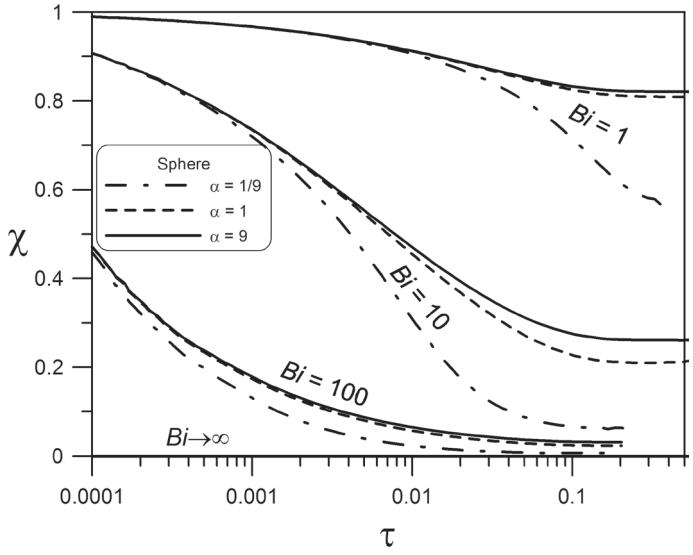

Fig. 5. The contribution of the mass transfer resistance in a fluid to the overall mass transfer resistance during adsorption in a tank

$$\frac{Y - Y_1}{R_L} = \frac{Y - Y^*}{R_{0L}} \tag{26}$$

Hence, the ratio between resistance to mass transfer in a liquid phase and the overall mass transfer resistance between phases $\chi = R_L/R_{0L}$ is:

$$\chi = \frac{Y - Y_1}{Y - \bar{Q}} \tag{27}$$

where it was substituted that $Y^* = \bar{Q}$.

Temporal variations of the quantity χ for different values of α and Bi are presented in Fig. 5. The graphs refer to spherical pellets and the quantity χ was determined from formula (27). As can be seen, the contribution (fraction χ) of the external resistance (in a liquid) to the overall resistance decreases. The greater the Biot number, the lower the fraction of the resistance to mass transfer in a liquid phase. For Bi $\rightarrow \infty$ resistance in a liquid phase disappears completely.

5. The analysis of measurement results

Experimental studies on kinetics of adsorption of a dye BR 200% from an aqueous solution on activated carbon BA-20 were conducted. The pellets had irregular shape, their average size was 2.0 mm. The experimental setup consisted of a tank with a stirrer, peristaltic pump and adsorber with a layer of adsorbent pellets of low height [8]. A dye concentration was measured by a UV-VIS Shimadzu spectrophotometer model UV-2600 at the 584 nm wavelength. A constant temperature of 23°C was kept during the measurements. The apparent velocity of the solution in the adsorber was $u = 0.0437$ m/s, adsorption equilibrium constant $K\rho_p = 426$, solution volume 0.25 dm^3, pellets mass 2.30 g. The results of measurements are presented in the form of symbols in Fig. 6. The Figure illustrates the relationship between the dye concentration in pellets and time.

On the basis of the measurement results, the diffusion coefficient of the dye referred to the concentration in pellets D_s and the mass transfer coefficient in the liquid phase k_l were determined. The following values were obtained: $D_s = 92.5 \cdot 10^{-12}$ m^2/s, $k_l = 18.0 \cdot 10^{-6}$ m/s [8]. These values were used to determine the computational relationship that is presented in Fig. 6 as a solid line. The good agreement with the experimental values indicates that the model of the process based on the equation of diffusion and adsorption corresponds to reality.

In Fig. 7, the interpretation of the process based on the dimensionless concentrations is presented. The symbols denote experimental values. The graph refers to the following values of parameters: Bi = 0.46 and $\alpha = 0.27$ which were determined for the conditions under which the experiments were conducted. For sufficiently long time lines corresponding to the concentrations converge to the value that refers to the equilibrium. The values of the concentrations for which the lines converge result from the relationship $\bar{Q} = Y = \alpha/(1 + \alpha)$. Temporal variations of the concentration at the phase boundary Y_1 and the contribution (fraction χ) of the mass transfer resistance in liquid to the overall resistance are also presented in the Figure. In the whole considered range of $\chi > 0.9$ it is clear that, for the considered system, the main mass transfer resistance is located in the liquid phase.

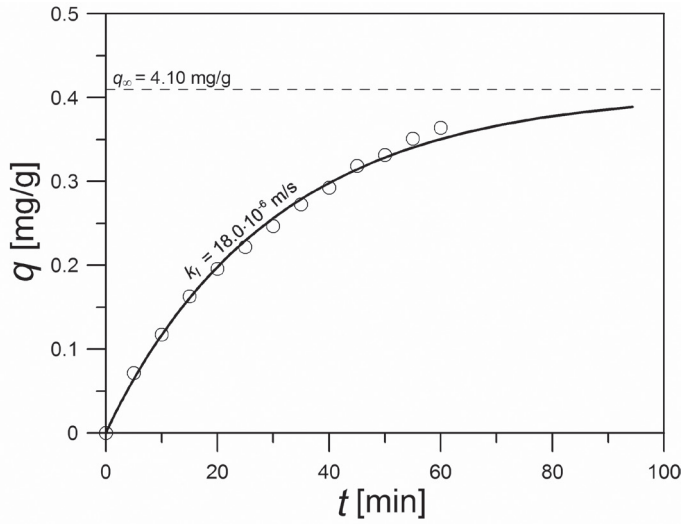

Fig. 6. Measurement results – the dependence of the dye concentration in pellets on adsorption time

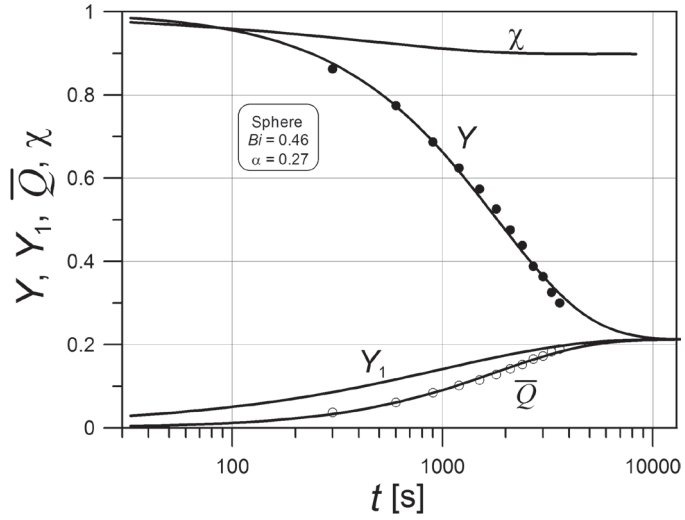

Fig. 7. Graphic interpretation of adsorption in a finite-volume tank

6. Conclusions

Using the approximate model of adsorption kinetics, one can easily determine the contribution of mass transfer resistance in the individual phases of a system. If one knows the dominant resistance, they can take the proper steps to intensify the adsorption process. For adsorption of a dye BR 200% on activated carbon of an average size 2 mm, the main

mass transfer resistance is located in a liquid phase. Therefore, the overall rate of the process can be increased by the intensification of flow of the liquid that contacts with adsorbent pellets.

The project was funded by The National Science Centre on the basis of the decision No. DEC-2011/03/N/ST8/04634.

References

[1] Chatzopoulos D., Varma A., *Activated carbon adsorption and desorption of toluene in the aqueous phase*, AIChE Journal 39, 1993, 2027–2041.
[2] Crank J., *The Mathematics of Diffusion*, Clarendon Press, Oxford 1975.
[3] Do D.D., *Adsorption Analysis: Equilibria and Kinetics*, ICP 1998.
[4] Gwadera M., *Zastosowanie przybliżonych równań kinetycznych w modelowaniu procesów adsorpcyjnych*, Rozprawa doktorska, Politechnika Krakowska, 2013.
[5] Gwadera M., Kupiec K., *Batch adsorption in a finite volume reservoir – application of approximate kinetic model*, Technical Transactions, 1-Ch/2014, 3–13.
[6] Kupiec K., Gwadera M., *Approximation for unsteady state diffusion and adsorption with mass transfer resistance in both phases*, Chemical Engineering and Processing 65, 2013, 76–82.
[7] Kupiec K., Gwadera M., Larwa B., *Adsorption in perfect mixing tank – comparison of exact and approximate kinetic models*, Chemical and Process Engineering 35, 2014, 277–291.
[8] Kupiec K., Gwadera M., Larwa B., *Kinetyka adsorpcji barwnika w zbiorniku z mieszadłem*, Inżynieria i Aparatura Chemiczna 4, 2014, 270–271.
[9] Lee J., Kim D.H., *Simple high-order approximations for unsteady-state diffusion, adsorption and reaction in a catalyst: a unified method by a continued fraction for slab, cylinder and sphere geometries*, Chemical Engineering Journal 173, 2011, 644–650.

TECHNICAL TRANSACTIONS | CZASOPISMO TECHNICZNE
CHEMISTRY | CHEMIA
1-Ch/2015

MONIKA GWADERA, KRZYSZTOF KUPIEC, ANDRZEJ MARSZAŁEK*

ON ADSORPTION OF WATER VAPOR ON SILICA GEL

BADANIE ADSORPCJI PARY WODNEJ NA SILIKAŻELU

Abstract

The aim of this work is to present the results of studies on heat and mass transfer in an adsorber, which is the main part of an adsorption chiller. The paper refers to adsorption of water vapor on silica gel grains. Adsorbent grains were coated on the outer surface of a copper pipe. The influence of grains diameter and flow rate of the gas phase on process intensity was considered.

Keywords: adsorption chiller, silica gel, water vapor

Streszczenie

Celem niniejszej pracy jest zaprezentowanie wyników badań dotyczących przenoszenia ciepła i masy w adsorberze stanowiącym podstawową część adsorpcyjnego urządzenia chłodniczego. Praca dotyczy adsorpcji pary wodnej na silikażelu. Ziarna silikażelu były naniesione na zewnętrzną powierzchnię miedzianej rurki. Badano wpływ wielkości ziaren oraz natężenia przepływu gazu na intensywność procesu.

Słowa kluczowe: chłodziarka adsorpcyjna, silikażel, para wodna

DOI: 10.4467/2353737XCT.15.101.4049

* Ph.D. Eng. Monika Gwadera, Ph.D. Eng. Krzysztof Kupiec, prof. CUT; M.Sc. Eng. Andrzej Marszałek (student), Faculty of Chemical Engineering and Technology, Cracow University of Technology.

1. Introduction

Nowadays, we can observe a steady increase in the level of pollution and the depletion of non-renewable energy sources. The development of new technologies that use environmentally friendly solutions is the answer to these problems. Refrigeration and air-conditioning are the fields where it is possible to reduce energy consumption. It was estimated that about 15% of world energy resources is used for cooling and refrigeration processes [5]. Because of this reason, an intensive development of chillers based on the adsorption process can be observed. They can be driven e.g. by solar energy, which can deliver the driving temperature difference.

The possibility of using environmentally friendly natural refrigerants is one the most important advantages of adsorption chillers. Water can be an example of such a refrigerant – it is ecologically clean, cheap and widely available. Moreover, automation and control of such systems is easy, the level of vibration and noise is low when compared with traditional compression systems and there are no corrosion problems as in the case of absorption chillers.

However, adsorption chillers have some disadvantages. The necessity to maintain vacuum in the system, their considerable size and weight, relatively low coefficient of performance COP and discontinuous operation resulting from alternating adsorption and desorption can be mentioned [2].

The aim of this paper is to present results of studies referring to enhancement of heat and mass transfer in an adsorber, which is one of the basic part of an adsorption chiller. Adsorption of water on silica gel was considered.

2. Operating principle of an adsorption chiller

Two adsorbent beds (adsorber and desorber), a condenser and an evaporator are the main components of an adsorption chiller. Heat exchangers are installed inside both beds. The operation of the chiller is cyclic. A cooling cycle is comprised of two adsorption/desorption steps and two switching steps.

In the adsorption period, adsorbate molecules are transported from evaporator to the adsorbent bed. This process is spontaneous as adsorbate molecules move from a gaseous phase to an adsorbed phase which is characterized by lower energy level and is more thermodynamically stable [4]. Transport of vapor molecules from the evaporator reduces the pressure. This causes boiling of the refrigerant and the production of the chilling effect. Adsorption is an exothermic process so it results in heat rejection. Therefore, in order to maintain the process, the adsorbent bed must be cooled by a cooling agent flowing in the heat exchanger and removing the rejected heat.

At the same time, the desorber, i.e. the second bed that is saturated with water vapor, interacts with the condenser. The bed is heated by a heating agent flowing in the heat exchanger as a result of which, the adsorbate molecules are desorbed from the bed and flow to the condenser where the vapor condenses. The liquid adsorbate flows back from the condenser to the evaporator.

When the adsorption/desorption period is complete, the switching step starts. The two reactor beds swap the roles. The path of the cooling and heating agent is changed. At this stage, there is no connection between the adsorber/desorber and the evaporator/condenser.

The adsorption pairs used in adsorption chillers can be divided in view of the adsorption type. The following pairs, based on physical adsorption, can be mentioned: activated carbon/ammonia, activated carbon/methanol, activated carbon/ethanol, zeolite/water, silica gel/water. Chemical adsorption occurs in the case of e.g. the metal chlorides/ammonia pair or metal hydrides/hydrogen pair. Adsorption can be enhanced by application of the pair with consolidated adsorbents e.g. zeolite and chlorides/water, porous substances and chlorides/ammonia or silica gel and chlorides/water.

3. Experimental setup

In this work, the silica gel/water pair is considered. Heat of adsorption, in this case, is equal to 2800 kJ/kg [6]. The degree of coverage (concentration of water in adsorbent grains) reported in literature is 0.2 g/g for typical working conditions of adsorbent chillers [7]. One of the advantages of silica-gel water pair is that such a system is non-toxic. Moreover, experiments were conducted under ambient temperature so there was no need to use adsorbates with evaporating point below 0ºC. Silica gel can be regenerated after it has been used so the sample can be used many times.

The experimental setup was built from scratch. Its scheme is presented in Fig. 1. A 12×1 mm copper pipe of a length of 220 mm was the measuring element. Inside of the pipe, there was a coaxial PTFE rod of diameter 8.5 mm. The external surface of the pipe was covered with the commercial *Wikol* glue based on polyvinyl alcohol and then it was coated with silica gel grains [1]. The pipe was put into a glass pipe with double walls as presented in Fig. 2. Internal diameter of the glass pipe was 23 mm and the external one – 46 mm. Static air between the walls of the glass pipe played the role of insulation. The operation of the system is similar to the double pipe heat exchanger. There are two circuits – a circuit of air saturated with water vapor and a circuit of cooling water (Fig. 2c). Cooling water flows through the annular cross-section between the copper pipe and PTFE rod. Air flows between the copper pipe covered with silica gel grains and the internal wall of the glass pipe. Before it enters the system, it is saturated with water vapor in humidifiers. When the air flows around the adsorbent grains, water is adsorbed.

Adsorption in pellets covering the surface is much different from the classic adsorption in a bed. The size of pellets plays an important role when adsorption occurs in a bed. The smaller the grains, the faster the process, but on the other hand, the greater the pressure drop. In the considered case the thickness of an adsorbent grains layer is more important than the grains size. Actually, the size of grains does not influence the pressure drop of gas flowing along the surface covered with grains.

The setup was equipped with measuring and control instruments. Flow rate of the air was adjusted by the controller 4850 produced by Brooks Instruments. Sensors PC52 (Michell Instruments) allowed one to measure relative humidity and temperature at the inlet and outlet of the air. A Cu-CuNi thermocouple was used to measure temperature in the central point of the adsorbent layer (Fig. 2b). Sensors PC52 and the thermocouple were connected to a multi-channel electronic recorder MPI-D manufactured by Metronic.

Silica gel samples were regenerated in the chamber dryer Wamed with digital temperature controller. The mass of the adsorbent was measured with the use of an electronic laboratory AS/X produced by Radwag.

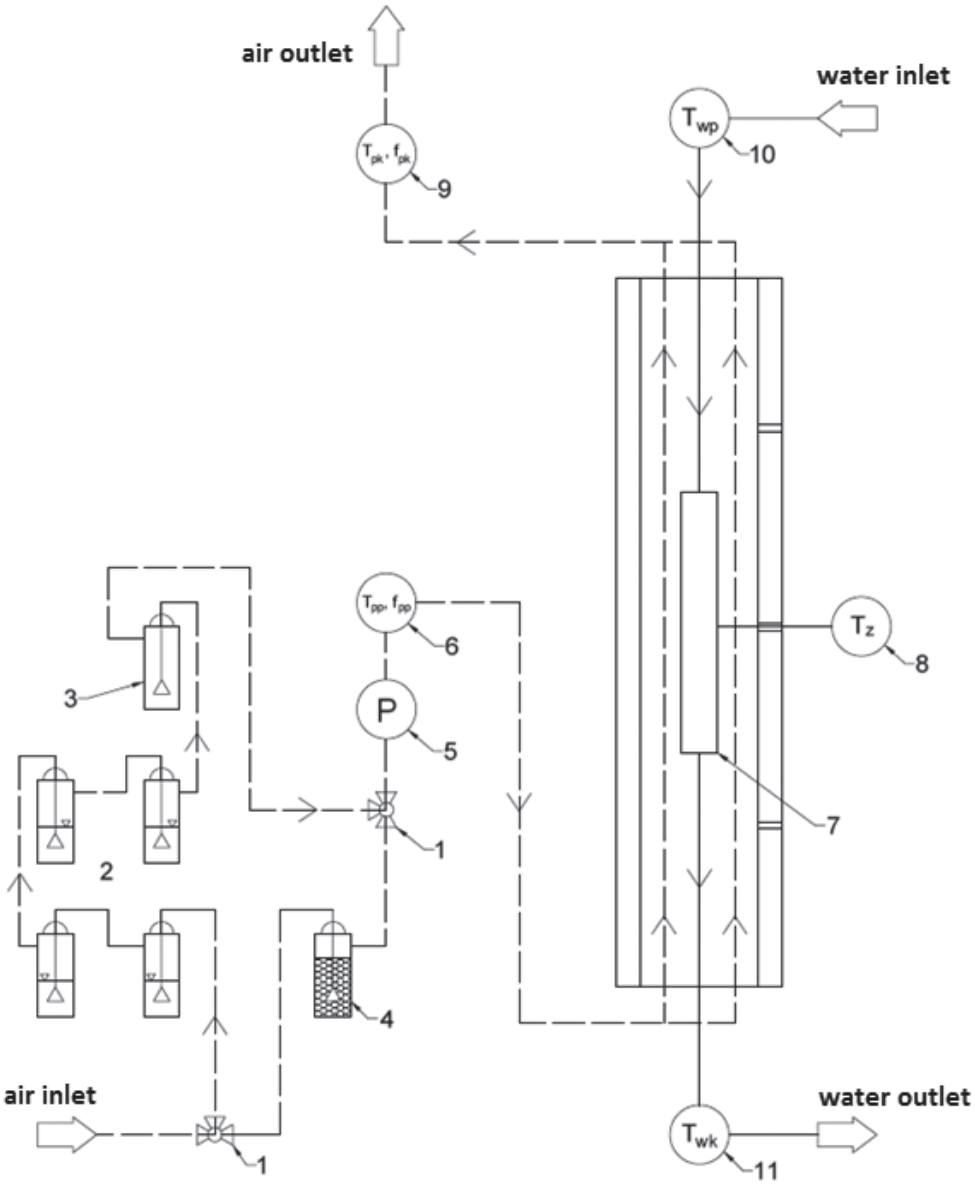

Fig. 1. Schematic diagram of the experimental setup: 1 – three-way valve, 2 – humidifiers, 3 – safety vessel, 4 – by-pass dryer, 5 – pressure converter, 6, 9 – air humidity and temperature sensors, 7 – measuring element, 8 – thermocouple measuring adsorbent temperature, 10, 11 – thermocouples measuring cooling water temperature

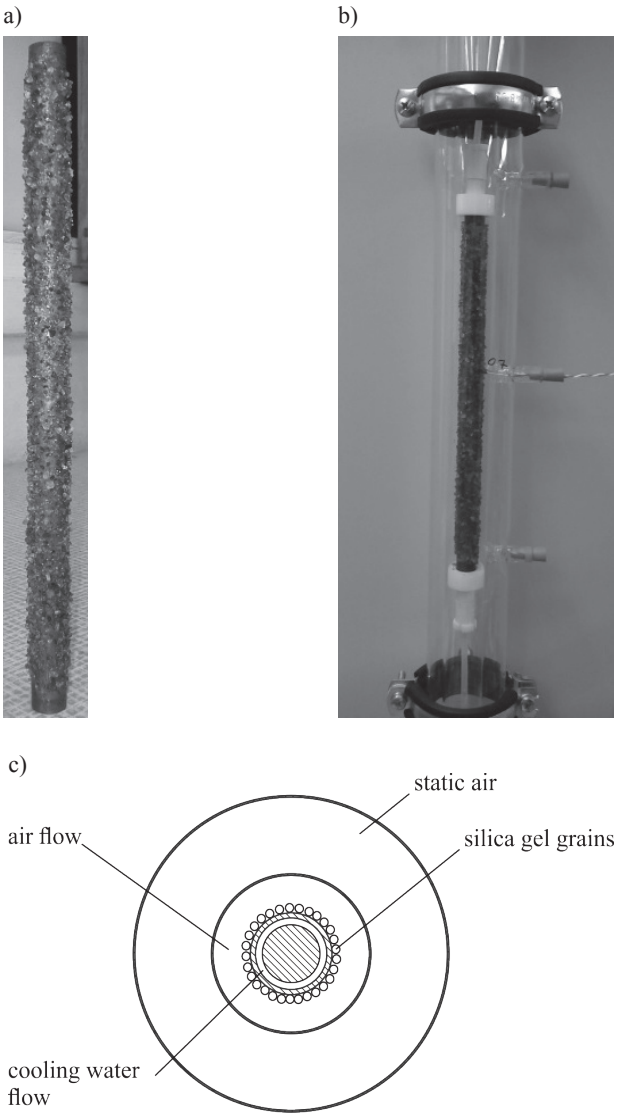

Fig. 2. Measuring element: a) after drying, b) after installation in the experimental setup, c) cross-sectional view

4. Experimental procedure

In the first step of the experimental procedure, the copper pipe was prepared. The pipe was weighed, its surface was degreased with acetone and then covered with glue and adsorbent grains. The pipe was then dried for 3 hours at 150°C in order to remove water from silica gel and glue. Then it was placed into the glass double-wall pipe. Before the measurements, air

flowing through the by-pass dryer packed with silica gel entered the installation in order to remove humid air from it. Then, the air flowed through humidifiers with water where it was saturated with water vapor and the measurements started. Recording of sensors indications was finished when the difference between inlet and outlet air humidity was steady for 10 min. The humid sample was then weighed and placed in the dryer to regenerate the adsorbent grains.

During the measurements, air temperature and humidity as well as mass of silica gel before and after adsorption of water was measured. Mass of adsorbed water was determined. Grains of diameters 0.63–0.8 mm, 0.8–1.0 mm and 1.5–2.0 mm were used. Inlet air humidity was 85%.

5. Measurement results

Two series of measurements were conducted. In the first series, the diameter of grains was constant. Air flow rate was the controllable parameter. The second series was based on changing grains diameter for the constant flow rate of inlet air. The obtained results are presented on the graphs in the form of symbols, however, only some of the results are depicted because of a high sampling frequency – sensors indications were recorded every 10 seconds.

In Fig. 3, the breakthrough curves (e.g. the relationships between outlet air relative humidity and time) for the first series of measurements are presented. Grains diameters are in the range 0.8–1.0 mm and air flow rates equal to 1 dm^3/min, 3 dm^3/min and 5 dm^3/min (these

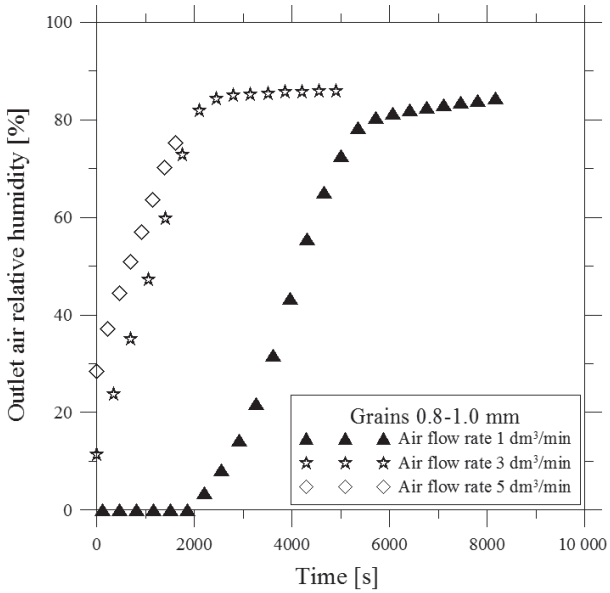

Fig. 3. Temporal variation of the outlet air relative humidity for different values of air flow rate and constant range of adsorbent grains diameters (breakthrough curves)

values refer to the air before saturation with water vapor in humidifiers). The flow rates refer to the air before saturation in humidifiers. On the basis of the graph, it might be concluded that in the case of flow rates equal to 3 dm^3/min and 5 dm^3/min the medium flows around the grains too fast so water vapor cannot be adsorbed effectively. When the flow rate was 1 dm^3/min, in the initial stage of the process there was no water vapor in the outlet air so there was no breakthrough at the very beginning of the process (i.e. for $t = 0$ s).

In Fig. 4, the graph for the second series of measurements is presented. It refers to the constant flow rate of air equal to 1 dm^3/min and different diameters of grains. It may be concluded that for this value of flow rate, the breakthrough was not observed for $t = 0$ s regardless of the grains size. Moreover, it should be noticed that the greater the grains, the longer the time after which the breakthrough of the bed occurs.

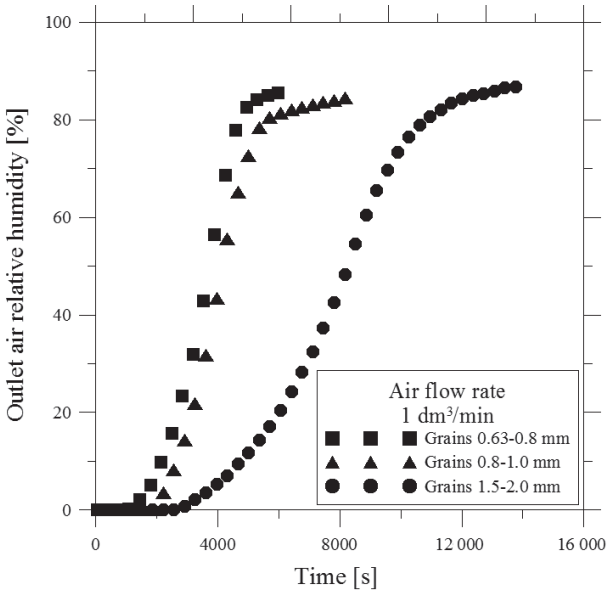

Fig. 4. Temporal variation of the outlet air relative humidity for different ranges of adsorbent grains diameters and constant air flow rate (breakthrough curves)

Graphs in Figs. 5 and 6 present temporal variations of the difference between the inlet and outlet air humidity. Fig. 5 refers to the constant grains size (0.8–1.0 mm) and different flow rates of air. According to the figure, the difference between inlet and outlet air humidity decreases over adsorption time. The result for grains 0.8–1.0 mm and air flow rate 1 dm^3/min at the initial stage of the process is distorted, which is caused by the fluctuations of inlet air humidity and by the humid air that was left in the installation after a previous measurement. It may also be concluded that the greater the flow rate of air, the smaller the difference between inlet and outlet air humidity at a certain moment of time. In the case of flow rates 3 dm^3/min and 5 dm^3/min, the initial humidity difference was relatively low because for high gas flow rates (high velocities) time of contact of the gas phase with the grains is too short to adsorb all of the water vapor contained in the air.

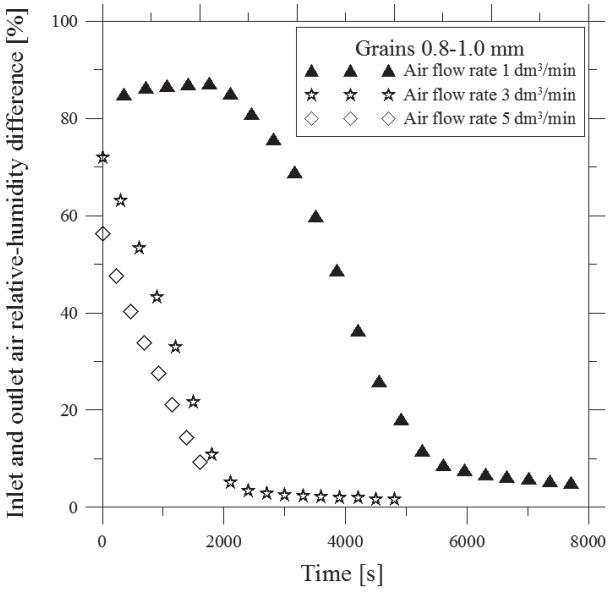

Fig. 5. Temporal variation of the differnece between inlet and outlet air relative humidity for different values of air flow rate and constant range of adsorbent grains diameters

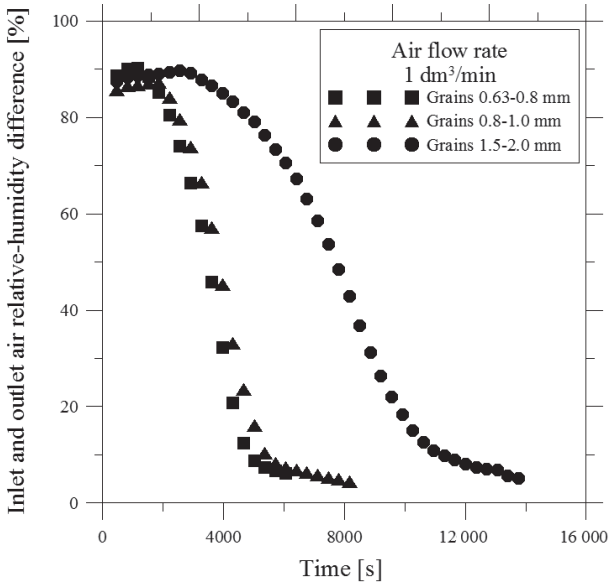

Fig. 6. Temporal variation of the difference between inlet and outlet air relative humidity for different ranges of adsorbent grains diameters and constant value of air flow rate

Fig. 6 refers to the constant flow rate of inlet air (1 dm^3/min) and different sizes of grains. It comes from the figure that the inlet and outlet air humidity difference at a certain moment of time is the greater, the greater the grains size.

Therefore, on the basis of Figs. 5 and 6, it may be stated that the time after which the relative humidity difference reaches values close to zero is longer, the greater diameters of the grains and the lower flow rate of the air.

Fig. 7 presents variations of temperature in the central point of the adsorbent layer. It may be noticed that temperature increases at the initial phase of the process, which is consistent with predictions [3]. It is caused by the generation of the heat of adsorption. Then, the temperature decreases because the grains are cooled by the flowing stream of gas. The greatest temperature increase, in relation to the initial adsorbent temperature, was observed in the case of the flow rate equal to 3 dm^3/min. If the flow rate was high enough, the adsorbent would be cooled efficiently by the flowing stream and the shape of the curve would differ (temperature would only decrease).

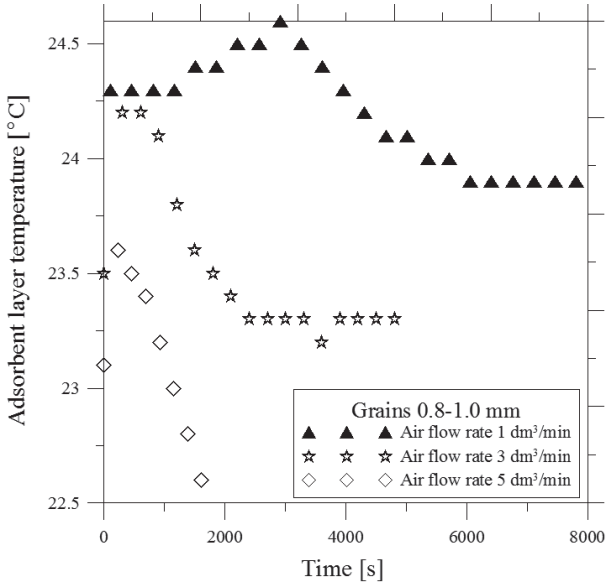

Fig. 7. Temporal variations of the adsorbent layer temperature for different values of air flow rate and constant range of adsorbent grains diameters

Results of measurements of mass of the adsorbed water are presented in Tables 1 and 2. It comes from the data contained in Table 1 that the final degree of coverage does not depend on the flow rate of the humid air. However, values from Table 2 allow one to conclude that greater size of grains gives the opportunity to adsorb greater amount of water regardless of the fact that the pipe cannot be covered with such grains as precisely as in the case of grains with smaller diameters.

Table 1

Results for the 1st series of measurements (constant range of grains diameters: 0.8–1.0 mm)

Air flow rate [dm^3/min]	Air velocity [m/s]	Mass of dry silica gel covering the copper pipe [g]	Mass of adsorbed water [g]	Degree of coverage (concentration of water in grains) [g/g]
1	0.058	3.34	0.87	0.26
3	0.174	3.58	0.96	0.27
5	0.290	3.22	0.85	0.26

Table 2

Results for the 2nd series of measurements (constant inlet air flow rate: 1 dm^3/min)

Grains diameters range [mm]	Mass of dry silica gel covering the copper pipe [g]	Mass of adsorbed humidity [g]	Degree of coverage (concentration of water in grains) [g/g]
0.63–0.8	3.06	0.79	0.26
0.8–1.0	3.34	0.87	0.26
1.5–2.0	5.96	1.70	0.29

6. Conclusions

On the basis of the collected data, one may state that for the air velocities that were under consideration the best results were obtained for low velocities (less than 0.174 m/s). Higher gas velocities reduce the adsorption effectiveness due to the short contact time. The contact time must be in the proper relation to the rate of adsorbate transport from the surface of grains to adsorption sites. Lower air velocities ensured the greatest temperature of the adsorbent, which is important because of the fact that the operation of adsorption chillers is based on thermal effects of the adsorption process.

The experimental data lead also to the conclusion that, for a certain velocity of air, the best results were obtained for grains diameters range between 1.5 mm and 2.0 mm. For such grains the breakthrough did not occur for the longest period of time. Moreover, in this case, a greater degree of coverage was observed.

The project was funded by The National Science Centre on the basis of the decision No. DEC-2011/03/N/ST8/04634.

References

[1] Gwadera M., *Adsorpcja wody na silikażelu*, Inżynieria i Aparatura Chemiczna 4, 2013, 317–318.

[2] Kim D.S., Infante Ferreira C.A., *Solar refrigeration options – a state-of-art review*, International Journal of Refrigeration 31, 2008, 3–15.

[3] Kupiec K., Rakoczy J., Gwadera M. *Zmiany temperatury w złożu adsorbentu w początkowych cyklach procesu adsorpcyjno-desorpcyjnego*, Inżynieria i Aparatura Chemiczna 5, 2011, 64–65.

[4] Li A., Bin Ismail A., Thu K., Ng K.C., Loh W.S, *Performance evaluation of a zeolite-water adsorption chiller with entropy analysis of thermodynamic insight*, Applied Energy 130, 2014, 702–711.

[5] Pridasawas W., *Solar-driven refrigeration systems with focus on the ejector cycle*, PhD Thesis, Royal Institute of Technology, KTH, Denmark, 2006.

[6] Srivastava N.C., Eames I.W., *A review of adsorbents and adsorbates in solid – vapour adsorption heat pump systems*, Applied Thermal Engineering 18, 1998, 707–714.

[7] Wang L.W., Wang R.Z., Oliveira R.G., *A review on adsorption working pairs for refrigeration*, Renewable and Sustainable Energy Reviews 13, 2009, 518–534.

TECHNICAL TRANSACTIONS | CZASOPISMO TECHNICZNE
CHEMISTRY | CHEMIA
1-Ch/2015

JOLANTA JAŚKOWSKA*, KAROLINA CHORABIK*, ZBIGNIEW MAJKA**

EFFICIENT METHODS FOR SYNTHESIS OF FLOROL AND ITS DERIVATIVES

OPRACOWANIE WYDAJNEJ METODY SYNTEZY FLOROLU I JEGO POCHODNYCH

Abstract

The paper describes and compares the two methods of synthesis of florol (**1**) (4-methyl-2-(2-methylpropyl) tetrahydro-2H-pyran-4-ol) by the Prins reaction. The first method involves the reaction for obtaining **1** in methylene chloride as solvent at 60°C. The second method applies the preparation of florol (**1**) and other tetrahydrofuran derivatives in solvent-free conditions in room temperature.

Keywords: fragrances, florol, florifol, synthesis of tetrahydropyran derivatives, Pins cyclisations

Streszczenie

W pracy opisano i porównano dwie metody syntezy florolu (**1**) (4-methyl-2-(2-methylpropyl)tetrahydro-2H-pyran-4-ol) na drodze reakcji Prinsa. Pierwsza metoda dotyczyła reakcji otrzymywania **1** w chlorku metylenu jako rozpuszczalniku w 60°C. Druga metoda, w warunkach bezrozpuszczalnikowych w temperaturze pokojowej, obejmowała zarówno syntezę florolu, jak i innych pochodnych tetrahydrofuranu.

Słowa kluczowe: związki zapachowe, florifol, florol, synteza pochodnych tetrahydrofuranu, cyklizacja Prins'a

DOI: 10.4467/2353737XCT.15.102.4050

* Ph.D. Eng. Jolanta Jaśkowska, M.Sc. Eng. Karolina Chorabik Institute of Organic Chemistry and Technology, Cracow University of Technology.

** Ph.D. Eng. Zbigniew Majka, Adamed Pharmaceuticals, Scientific Department.

1. Introduction

Florol (**1**) is also known as Floriffol, Floros, Floral Pyranol, Muguetol. It belongs to fragrance compounds with floral (Lily of the Valley) scent. Floral (**1**) is found in many perfumes such as: "XS for her" (Paco Rabanne) 0.5%, "O oui" (Lancome) 5.5%, "Dazzling Gold" (Estee Lauder) 8.5%, "J'adore" (Dior) 5.6%, "Fragile" (Jean Paul Gaultier) 2.7%, "L'Eau d'Eden" (Cacharel) 0.16%, "Romance" (Ralph Lauren8) 3%, "L'Eau de Kenzo masc" (Kenzo) 1%. This compound exists as four isomers which have a slightly different intensity and odor [1]. Methods for the preparation of florol (**1**) are described in literature based on the reaction Prins [2, 3] or cyclization reaction of the corresponding derivatives [4]. Prins'a reaction is most commonly described in literature by synthesis systems containing system pyran or tetrahydropyran [5-8]. Florol (**1**) can also be used as a starting material to obtain another fragrance compound called Clarycet, which has a smell of herbal-floral with a hint of dried fruit [3, 10, 11].

2. Results and discussions

The aim of the research was to develop efficient methods for synthesis of florol (1) (4-methyl-2-(2-methylpropyl) tetrahydro-2H-pyran-4-ol) (Fig. 1) and its derivatives.

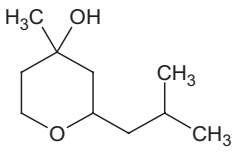

1

Fig. 1. Florol (4-methyl-2-(2-methylpropyl)tetrahydro-2*H*-pyran-4-ol)

Florol (**1**) was prepared by a Prins cyclization reaction between isovaleraldehyde (**2**) and isoprenol (**3**) (Fig. 2).

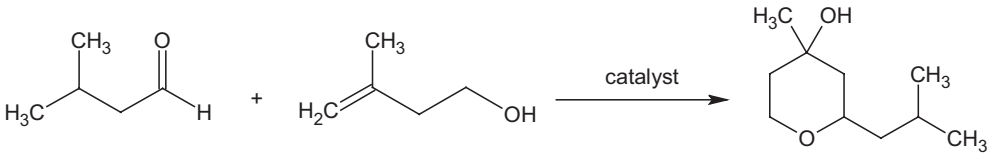

2 **3** **1**

Fig. 2. Florol (**1**) synthesis in Prins cyclization reaction

We started our research from the process carried out in dichloromethane as a solvent at a temperature of 60°C (method I), in the next step of the study, we assessed the solvent-free synthesis method at room temperature (method II). In each case, florol (**1**) was obtained in the form of two diastereoisomers (Fig. 3), which corresponds with literature data [3].

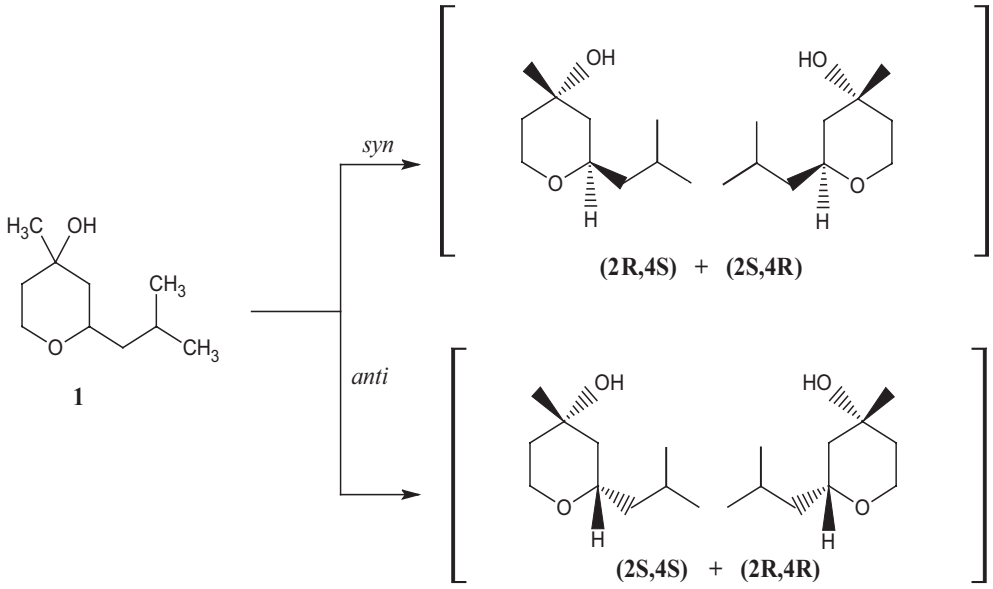

Fig. 3. Diastereoisomers of florol (**1**)

Separation on the chromatographic column (eluent: hexane/ethyl acetate – 3:1) and analysis of the results obtained by TLC, GC-MS and ^{1}H NMR led to the identification of isomers *syn* R_f = 0.20, RT = 5.35 oraz *anti* R_f = 0.35, RT = 5.58.

The synthesis according to method which was described in patent from 2005 [12] results in a 32% yield of the florol (**1**). The process took more than six hours, and the mixture, as already mentioned, required heating. Solvent-free reactions (method II) in the system SiO_2: *p*-toluenesulfonic acid gives a better yield over two hour (39%). This reaction mainly based on literature data, except thata different type was used there and the proportions of SiO_2 were changed [3]. Short reaction time and simplicity of method encouraged us to test the reaction in a wider range. First, the effect of the reaction time on the process was evaluated. It has been observed that the extension of the reaction time to 24 hours allows to increase the yield of florol (**1**) to 55%, and carrying out the process furthermore by 7 days results in a 63% yield. In a next step, the effect of a different catalysts was tested with a process for 24h (Table 1). Acids are most frequently recommended in literature for this type of synthesis catalysts, especially *p*-toluenesulfonic acid and methanesulfonic acid [3, 12]. We also tested other acid catalyst (sulfuric acid), and a catalyst which has a neutral pH (sodium sulfate). Studies show that, in addition to previously used *p*-toluenosulfonoego acid, the process can be carried out also by using methanesulfonic acid (64%) and sulfuric acid (43%) (Table 1). In the case of sodium sulfate, yield of **1** was very low (2%).

Table 1

The influence of the catalyst on the yield of florol (1).
Reaction time 24h

No.	Catalyst	Yield
1	*p*-toluenesulfonic acid	55
2	methanesulfonic acid	64
3	sulfuric acid	43
4	sodium sulfate	2

During the research, we also tested a series of reactions in which the isovalericaldehyde (**2**) is replaced by the other aldehydes **5-8**, to give the compounds based on 2-substituted--4-methyl-tetrahydropiranol **9-12** (Fig. 4). The synthesis was carried out at room temperature for 1h using a catalyst which was the *p*-toluenesulfonic acid.

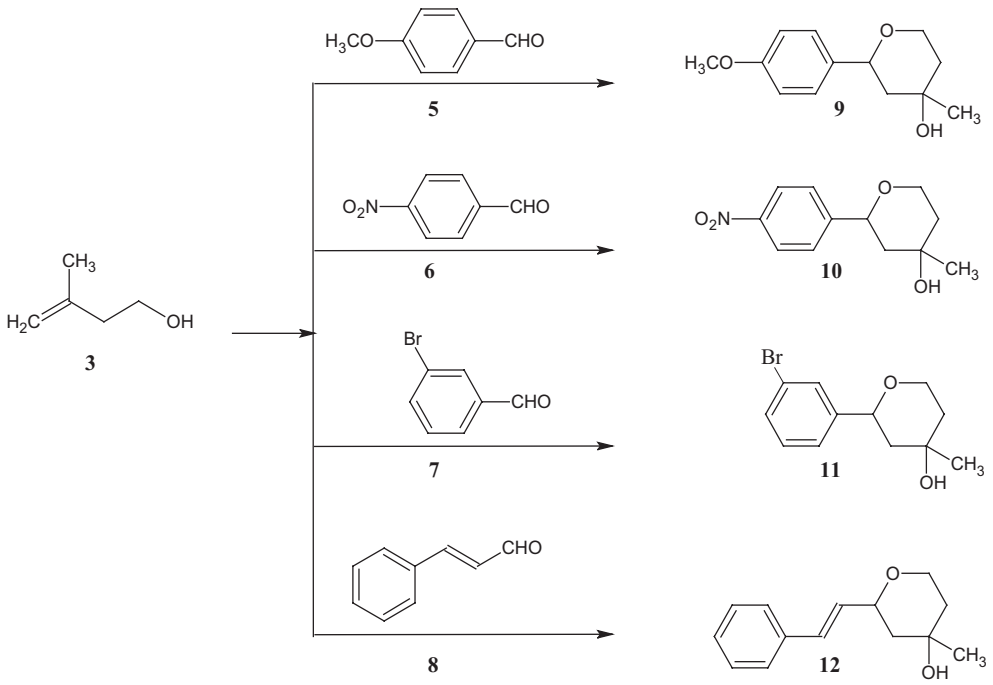

Fig. 4. Synthesis of tetrahydropyran derivatives

Expected compounds **9-12** were obtained with the high yields (Table 2) in comparison with data described in similar reactions in literature [3]. All the synthesized compounds were evaluated by TLC and GC, and their structures were confirmed on the basis of ^{1}H NMR spectra.

Table 2

Synthesis of tetrahydropyran derivatives

No.	Aldehyde structure	Compound	Yield
1	5	9	92
2	6	10	63
3	7	11	91
4	8	12	95

3. Experimental

The reactions were monitored by TLC on silica-gel plates (Merck 60F254) using chloroform/methanol (9:1) as eluent. TLC plates were visualized by exposure to solution *p*-anisaldehyde – sulfuric acid followed by heating on a hot plate. Starting materials, solvents, and reagents were purchased from commercial sources and were used without further purification. The structure of the obtained compounds was confirmed by ^{1}H-NMR, IR, and MS spectral data, and by comparing their physical properties to those described in literature. GC analyzes were performed on the: Varian 3800 GC with autosampler CP8400 and dispenser 1079 Split/splitless. The samples were dissolved in methanol. The prepared sample was injected onto the column of the gas chromatograph (0,5 µl). Column: VF-1 MS 30 m × 0,25 mm × 0,25 µm. Oven: initial temperature:60°C, kept for 1 min, accretion 25°C/min. do 220°C, kept for 4,6 min. Analysis time 12 minutes. An injection port temperature 250°C, split injection: 100:1, 0,5 µl. Carrier gas: helium 99.9995%, flow 1,2 ml/min. FID detector. Air 350 ml/min., hydrogen: 35 ml/min., auxiliary gas (He): 25 ml/min. Data recording with a frequency of 20 Hz. If the purity analysis recorded total ion current chromatogram "FID". Purity is calculated by summing up the area of all peaks in a chromagram and determining the percentage of the surface area of the analyte**.**

Synthesis of florol (**1**) (4-methyl-2-(2-methylpropyl)tetrahydro-2*H*-pyran-4-ol)

Method I

11.4 cm^3 (8.94 g, 0.1038 mol) isovaleraldehyde (**2**) and 0.034 cm^3 (0.051 g, 0.0053 mol) methanesulfonic acid were introduced into a 100 cm^3 flask and mixed at room temperature. Then, the mixture was heated to 60°C and after that 3.14 cm^3 (2.681 g, 0.0311 mol) isoprenol (**3**) was added dropwise to over 3 hours under stirring. After that, the mixture was kept at this temperature for another 3 hours. After cooling, the mixture was neutralized and extracted with methylene chloride. The organic layer was evaporated to give a yellow oil with a characteristic odor. Florol (**1**) as a mixture of two diastereomers was obtained in a yield of 32%.

Method II

General procedure: In a mortar containing silica gel (70-230 mesh) (12.5 g, 0.200 mol) and *p*-toluanesulfonic acid (0.5 g, 0.00029 mol) was added the aldehyde (**2**, **5**-**8**) (0.001 mol) and isoprenol (**3**) (0.0011mol). The resulting mixture was ground for appropriate time.

Reaction was monitored by TLC. After the reaction, the product was washed to remove by using a mixture of hexane/ethyl acetate (3:1). After evaporation of the solvent, the resulting compounds were subjected to TLC analysis, the GC-MS: 172 (*M+1*). Structures were confirmed by ^{1}H NMR.

Syn diastereoisomer: oil, R_f = 0.44, RT = 5,58; ^{1}H NMR σ 0.9 (d, 6H), 1.2 (ddd, 1H), 1.26 (s, 3H), 1.29 (dd, 1H), 1.4-1.5 (m, 3H), 1.61 (td, 1H), 1.71 (hept., 1H), (3.75-3.84 (m, 2H), 3.41 (td, 1H).

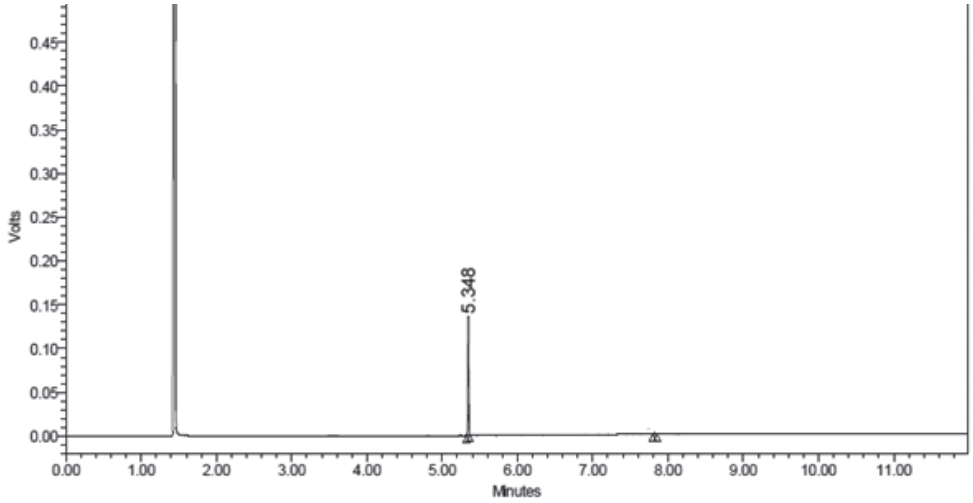

Fig. 5. GC spectra *syn diastereoizomer* (2S, 4S)+(2R, 4R)

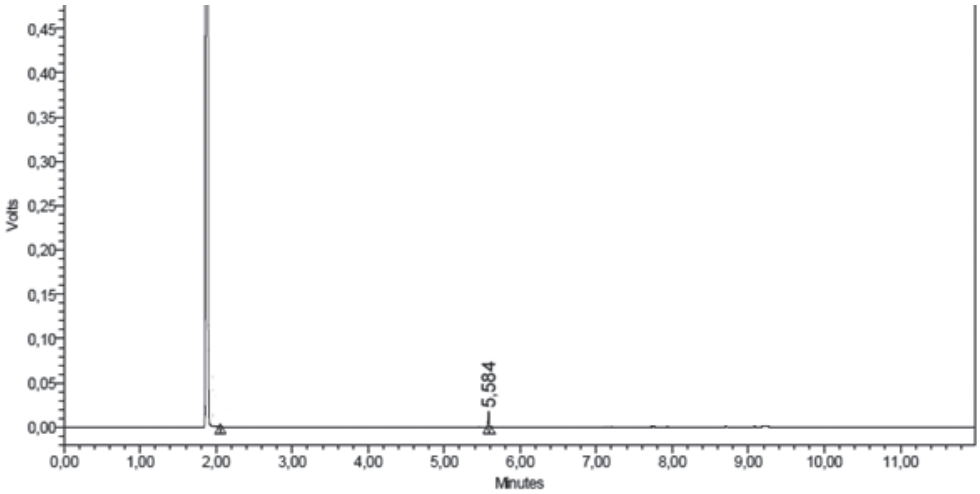

Fig. 6. GC spectra *anti diastereoizomer* (2R, 4S)+(2S, 4R)

Anti diastereoisomer: oil, R_f = 0.20, RT = 5.35, ^{1}H NMR σ 0.8-0.9 (d, 6H), 1.15 (ddd, 1H)1.32 (s, 3H), 1.39 (t, 1H), 1.49 (ddd, 1H), 1.56 (dq, 1H), 1.64 (dt, 1H), 1.69-1.73 (td, 1H), 3.23-3.37 (m, 1H), 3.41 (td, 1H), 3.92 (ddd, 1H).

Tetrahydropyran derivatives **9-12** (obtained as a racemic diastereoisomeric mixture) were synthesized by *method II*

2-(4-methoxyphenyl)-4-methyltetrahydro-2*H*-pyran-4-ol (**9**)
Obtained by reaction with 4-methoxybenzaldehyde (**5**) R_f = 0.23, R_f = 0.44 (R_f lit. = 0.31 and 0.46 [3]); RT = 5.63; 5.73; GC-MS: 223 (*M+1*).

4-methyl-2-(4-nitrophenyl)tetrahydro-2*H*-pyran-4-ol (**10**)
Obtained by reaction with 4-nitrobenzaldehyde (**6**) R_f = 0.52, R_f = 0.61 (R_f lit. = 0.42 and 0.61 [3]); RT = 5.62; 5.72; GC-MS: 238 (*M+1*).

2-(3-bromophenyl)-4-methyltetrahydro-2H-pyran-4-ol (**11**)
Obtained by reaction with 3-bromobenzaldehyde (**7**) R_f = 0.18, R_f = 0.28 (R_f lit. = 0.22 and 0.28 [3]); RT = 5.62; 5.72; GC-MS: 271 (*M+1*).

2-(4-ethenylphenyl)-4-methyltetrahydro-2H-pyran-4-ol (**12**)
Obtained by reaction with (2E)-3-phenylprop-2-enal (**8**) R_f = 0.58, R_f = 0.71 (R_f lit. = 0.56 and 0.73 [3]); RT = 5.62; 5.73; GC-MS: 219 (*M+1*).

4. Conclusions

During the research, two methods of synthesis of florol (1) were evaluated. In the solvent-free method, the impact of catalyst and the duration of the process to yield of 1 were also estimated. The universality of this method was confirmed in the reactions leading to a variety of tetrahydropyran derivatives. In each case, the compounds were obtained in the form of two diastereomers.

References

[1] Abate A., Brenna E., Fronza G., Fuganti C., Gatti F.G., Serra S., Zardoni E., *Preparation of the Enantiomerically Enriched Isomers of the Odorous Cyclic Ethers Clarycet®, Florol® and Rhubafuran® by Enzymatic Catalysis*, Helvetica Chimica Acta, 2004, 765–780.

[2] Sprecker M.A., Bright S., Greene R.E., *2,4,4-Trisubsituted Tetrahydro Pyranyl Esters And Organoleptic Uses Thereof*, International Flavors and Fragrances Inc. N.Y., US4963285, 16.10.1990.

[3] Macedo A., Wendler E.P., Dos Santos A.A., Zukerman-Schpector J., Tiekink E.R.T., *Solvent-free Catalysed Synthesis of Tetrahydropyran Odorants: The Role of SiO_2:p-TSA Catalyst on the Prins-Cyclization Reactio*, Journal Of The Brazilian Chemical Society, 2010, 1563–1571.

[4] Gupta P., Sethi V.K., Taneja S.C., Shah B.A., Andotra S.S., Koul S., Chimni S.S., Qazi G.N., *Odoriferous Cyclic Ethers via Co-Halogenation Reaction: Facile Preparation of Nerol Oxide, Florol®, Florol® Methyl Ether, and Pityol® Methyl Ether*, Helvetica Chimica Acta, 2007, 196–204.

[5] Biermann U., Lutzen A., Metzger J., *Synthesis of Enantiomerically Pure 2,3,4,6-Tetrasubstituted Tetrahydropyrans by Prins-Type Cyclization of Methyl Ricinoleate and Aldehydes*, European Journal of Organic Chemistry, 2006, 2631–2637.

[6] Olier C., Kaafarani M., Gastaldi S., Bertrand M.P., *Synthesis of tetrahydropyrans and related heterocycles via Prins cyclization; extension to aza-Prins cyclization*, Tetrahedron, 2010, 66, 413–445.

[7] Crosby S.R., Harding J.R., King C.D., Parker G.D., Willis C.L., *Oxonia-Cope rearrangement and side-chain exchange in the Prins cyclisation*, Organic Letters, 2002, 4, 577–580.

[8] Hiebel M.A., Pelotier B., Piva O., *Total synthesis of (+/–)-diospongin A via Prins reaction*, Tetrahedron, 2007, 63, 7874–7878.

[9] Yadav J.S., Reddy B.V.S., Maity T., Kumar G.G.K.S., *In(OTf)3-catalyzed synthesis of 4-thiocyanotetrahydropyrans via a three-component reaction*, Tetrahedron Letters, 2007, 8874–8877.

[10] Rove D.J., *Chemistry and technology of Flavour and fragrances*, De Monchy Aromatics LtdPoole, UK; Blackwell Publishing Ltd., 2005, 5.3, 88.

[11] Murty M.S.R., Rajasekhar K., Harikrishna V., Yadav J.S., *Bismuth triflate Catalyzed Prins-Type Cyzylization in Ionic Liquid: Synthesis of 4-Tetrahydropyranol Derivatives*, Heteroatom Chemistry, 2008, 104–106.

[12] Umada A., Ataka Y., Tanaka S., Naito K., Mine K., Kao Corporation; 2005, US20050004210A1.

TECHNICAL TRANSACTIONS | CZASOPISMO TECHNICZNE
CHEMISTRY | CHEMIA
1-Ch/2015

ALEKSANDER KOZAK*, MARCO BONOPERA**

PERFORMANCE ANALYSIS OF REINFORCED POLYMER CEMENT MORTARS "RPCMS" USED FOR REPAIRING CONCRETE STRUCTURES

ANALIZA PORÓWNAWCZA ZAPRAW CEMENTOWO-POLIMEROWYCH STOSOWANYCH DO NAPRAWY BETONU

Abstract

Concrete structures operating under different environmental conditions are subject to the action of aggressive gaseous and liquid media, which leads to their degradation. Even well-designed buildings, after time, can have problems to fulfil appropriate requirements concerning their further service life. Fiber reinforced mortars based on cement modified with different types of polymers are commonly used materials for renovating concrete structures. They should fulfil requirements concerning their high adhesion to concrete, minimum tensile strength, compatibility with repaired concrete and low shrinkage. The aim of the work was to compare the performance of three reinforced PCMs based on various polymers. The following features were tested: adherence to concrete, shrinkage and flexural strength.

Keywords: concrete structures; polymer modified mortar, concrete degradation

Streszczenie

Konstrukcje betonowe eksploatowane w różnych warunkach środowiskowych narażone są na działanie agresywnych mediów gazowych i ciekłych, co prowadzi do ich stopniowej degradacji. Nawet dobrze zaprojektowane budowle mają z czasem problemy ze spełnieniem odpowiednich wymagań dotyczących ich bezpiecznej eksploatacji. Powszechnie stosowanymi materiałami naprawczymi są zaprawy cementowe z dodatkiem włókien i polimerów. Muszą one spełniać odpowiednie wymagania dotyczące ich odpowiedniej adhezji do podłoża betonowego, minimalnej wartości wytrzymałości na zginanie, kompatybilności z naprawianym betonem oraz małego skurczu. Celem pracy było porównanie trzech materiałów naprawczych zawierających różne polimery. Badano następujące cechy: przyczepność do betonu, skurcz oraz wytrzymałość na rozciąganie.

Słowa kluczowe: konstrukcje betonowe, zaprawy modyfikowane polimerem, degradacja betonu

DOI: 110.4467/2353737XCT.15.103.4051

* Ph.D. Eng. Aleksander Kozak, Institute of Building Materials and Structures, Faculty of Civil Engineering, Cracow University of Technology.

** Ph.D. student, Marco Bonopera, Department of Engineering, University of Ferrara.

1. Introduction

Concrete is the most frequently structural material because of the following features:
- ease of concrete placement,
- good durability,
- high mechanical strength,
- relatively low cost [1].

It has been used for many years to build a great number of structures such as houses, large buildings and bridges. A period of dynamic growth in concrete use came during the 1960s as a result of an application of superplasticizers, ready-mix concrete and boarding. The common outlook that concrete is a durable, maintenance-free construction material has changed in recent years. Some examples can be given to show that concrete has not fulfilled assumed requirements [2]. Although a lot of concrete structures are successfully constructed worldwide each year, there are a great numbers of structures that deteriorate or become unsafe due to the following factors: incorrect design, poor workmanship and maintenance, overloading, chemical attacks, corrosion of rebar, foundation settlement, abrasion, fatigue effect, atmospheric contamination, floods etc. These factors affect the durability of concrete structures. In recent years, the growing need to repair structures has led to a significant increase in the expenditure for restoration in comparison with costs of new structures. It has been estimated that, currently in Europe (particularly in Italy), the cost of maintenance and repair works of old structures is around 50% of the total expenditure on construction [3]. Repair and rehabilitation of deteriorated concrete structures are crucial for their service life. An appropriate repair method improves the performance of the structure (prolongs serviceability), increases its strength and stiffness, enhances the appearance of the concrete surface, provides water tightness and prevents from attacks of aggressive media on reinforcement [4]. Currently, Reinforced Polymer Cement Mortars "RPCMs" are commonly used to renovate old concrete. The materials consist of cement and addition of polymer, oligomer or monomer to mortar mix. The chemical modifier may polymerize both after mixing (post-mix), i.e. the polymerization takes place during the hydration of Portland cement or polymerize before mixing (pre-mix). In latter case, chemically inactive polymers are introduced into concrete mix and their action is predominantly physical-chemical. Repair materials should be characterized by the following properties: high tensile strength and adhesive strength to steel and/or old concrete, good corrosion and chemical resistance, low shrinkage etc. The increase of these properties, in comparison with ordinary concrete, is achieved by an addition of some polymers such as sulfonated melamine-formaldehyde resin, styrene-butadiene rubber, polyvinyl alcohol and methylcelullose [5, 6].

2. Materials and test methods

The selected RPCMs for these studies were one-component mortars commonly used as repair materials. They consisted of cement, fibers and different types of polymer. RPCM-A contained two polymers: melment F10, which was a product based on melamine and methylcellulose as well as set retarding admixtures. The properties of the melamine-based polymer are as follows: an increase in concrete strength, waterproof and resistance to chemicals. As far as methylcellulose is concerned, it is characterized by high water retention

for proper curing and improved mortar workability. A polymer addition in RPCM-B was methylcellulose while, in the case of RPCM-C, it was a melamine based polymer together with polyvinyl alcohol (PVA). PVA polymer is added to mortars, since it allows obtaining a high adhesion as well as a high tensile strength and flexibility of mortar. The mixtures of the three mortars were prepared according to EN 1015-2 [7] and requirements given in the technical sheets of the used materials (mixing time, water-mortar ratio). The samples, before demoulding, were kept under polyethylene foil for 24 hours at 20±2 C and 95% RH and then, after demoulding, were kept for 2 days at 20±2 C and 95 RH under the foil. Afterwards, they were put into a climatic chamber at a temperature of 21±2°C and 65±5% RH for the following 25 days. Unmodified mortar was prepared according to PN-EN 196-1:1996 [8]. Flexural strength of the RPCMs was determined according to EN 1015-11 [9]. Three-point bending tests were done by the means of the Zwick/Roell Z100 universal machine using 40 × 40 × 160 mm samples with a curing period of 7 and 28 days. Pull-off tests were performed according to EN 1542 [10]. For measuring the pull-off forces, a concrete slab (C30/37) of dimensions 1300 × 1300 × 150 mm was prepared according to EN 1766 [11] and then, after an appropriate curing, thickness of the mortars of 10 mm were applied. Then, the mortar thickness was covered using a polyethylene sheet and left to cure for 7 days at around 20°C. The sheet was then removed and the concrete slab was kept in air at around 20°C and 65% relative humidity for the remaining 21 days. After 28 days, pull-off tests were done using the Proceq Z15 dynamometer. Pull-off tests consisted in the measuring of the adhesive strength of the repaired material to the old concrete. The material was loaded at a constant rate and the maximum strength was recorded. The tests were performed after 1 day after installing the steel dollies (disks) on the repair materials. The load was applied at a continuous and even rate until failure. Shrinkage tests and sample preparation were done according to OENORM B 3329:2009 [12]. The test allows analysing the deformations that may occur in a mortar after its application. RPCMs were inserted within U-shaped profiles, previously covered with neoprene sheet. One sample for each RPCM was obtained by filling a U-shaped stainless steel profile with length of 1000 mm and cross section of 60 × 38 mm. Three displacement sensors were connected to the sliding anchors of the moulds. The mortars inside U-shaped profiles were free to shrink or expand, because the container was made of a fixed anchor and a sliding anchor movable on three wheels at both sides. The motion of this anchor was registered by a high sensitive “linear variable differential transformer” (LVDT) probe. A digital probe was used as displacement sensor, which was connected to the probe interface electronics that has converted the analogue signals into a digital format. Shrinkage tests were performed on the three samples for 45 days. Observations of an interfacial transition zone between the old concrete and a bonding slurry as well as between the bonding slurry and a repair material were done using the Zeiss EVO MA 10 microscope.

3. Test results

3.1. Bending results

The obtained flexural strengths of the three RPCMs (A, B and C) after curing periods of 7 and 28 days are presented in Fig 1.

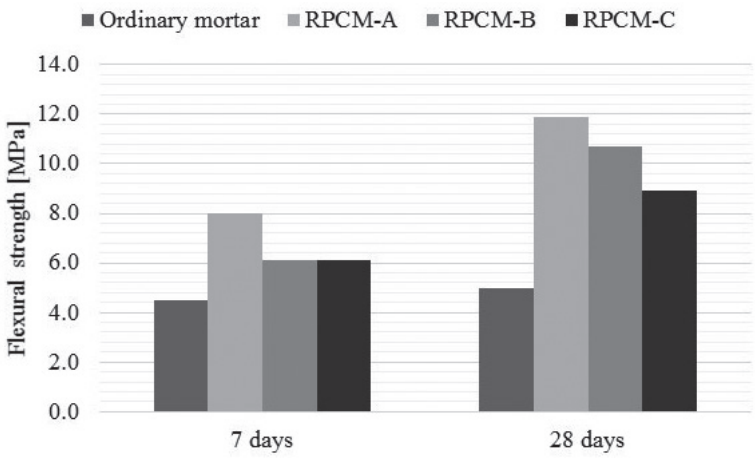

Fig. 1. Bending tests results of the RPCMs and comparison with ordinary mortar

Test results show that the repair materials tested exhibit much higher values of flexural strength than that of ordinary mortar used as a reference sample. The difference is particularly clear in case of the samples cured for 28 days. The flexural strengths of the repair mortars were also higher than values provided in the technical sheets of the companies and are within the range of test results obtained by other authors with reference to similar proprietary repair materials [13].

3.2. Pull-off adhesion tests

The obtained bond strengths of the three RPCMs, using a dynamometer, are presented in Table 1. As a reference, an unmodified mortar, M was also tested using Proceq Z15 dynamometer.

Table 1

Pull-off test results of the RPCMs

	RPCMs	Bond strength MPa	Mean value MPa	Mode of failure
Proceq Z15 dynamometer	A	3.7–4.3	4.0	in concrete
	B	3.8–4.5	4.1	in mortar/in concrete
	C	3.1–3.5	3.4	in mortar/in concrete
	M	1.3–1.6	1.5	in mortar

RPCMs showed very good adhesion to the concrete support and test results were much higher than that of ordinary mortar. In case of polymer mortars, failures occurred in the substrate or in the repair material and in case of unmodified mortar, it took place in mortar.

In all cases, cohesive mode of failure was observed. Bond strengths were homogeneous keeping in mind the tested feature. All values were much higher than 2.0 MPa, which was the minimum recommended value according to EN 1504-3 [14].

3.3. Scanning Electron Microscopy

SEM photograph of one of the repair material systems shows that the repair system was well placed on the old concrete to ensure high adhesion and the pull-off tests confirmed it, Fig. 2. One can see three zones: the layer of the repair material at the bottom, the bonding slurry in the middle, while the old concrete is at the top.

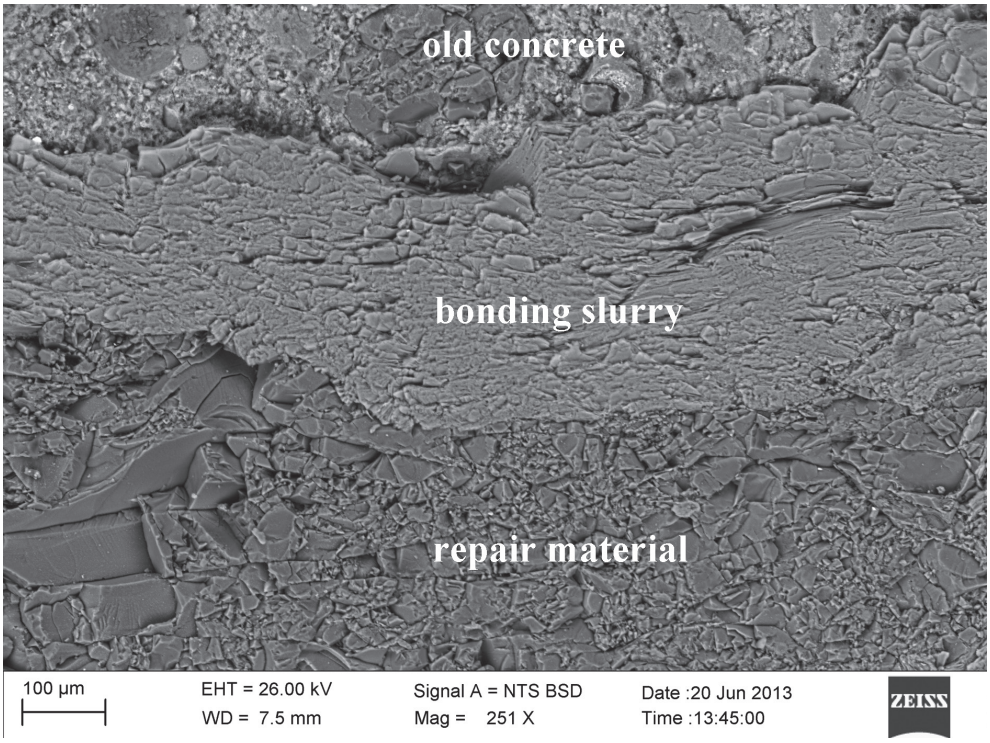

Fig. 2. SEM of one repair material system

3.4. Shrinkage results

Fig. 3 presents samples during shrinkage tests. RPCM-B and RPCM-C showed some expansion in the early stage of setting. RPCM-B showed the expansion within 24 hours after moulding and the maximum value was 0.1 mm/m. In case of RPCM-C, expansion period lasted up to 7 days, reaching the maximum value of 0.26 mm/m after around 48 hours after moulding. Then, progressive contraction of these materials was observed and, after 28 days, the maximum contraction values were 0.52 mm/m and 0.34 mm/m, respectively.

RPCM-A also showed very good volumetric stability. The difference in deformation was only 0.39 mm/m after 28 days and lack of expansion was observed. Micro-cracks did not emerge in any RPCMs samples during the test period.

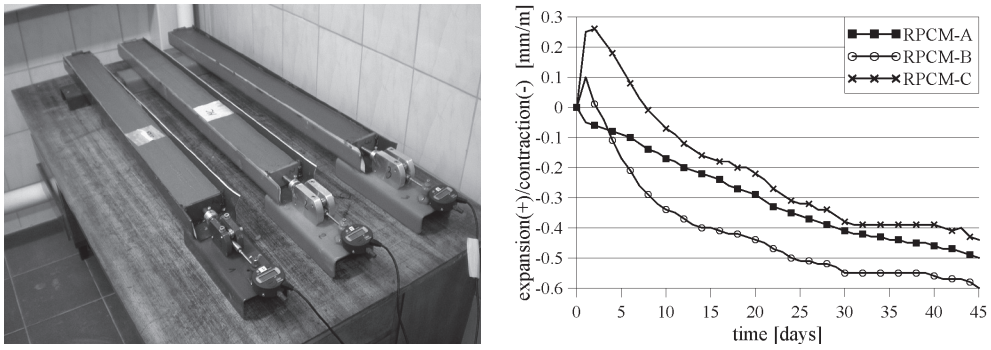

Fig. 3. RPCMs samples during shrinkage tests (a) and the course of shrinkage during 45 days (b)

4. Discussion

4.1. Effective repair related to the presence of micro-fibers

The behavior of the repair system with fibers, up to cracking, is mainly governed by the performance of the cement matrix. RPCM flexural strength increases until 28 days. The porosity can play a major role, since the volume fraction of pores is not the same in the materials after 7 and 28 days. It is known that cement hydration strengthens the cement-based materials by filling the capillary pores with hydrates, especially during the first month of setting [15]. Cement hydration is responsible for the increase in bending strength. During shrinkage tests, micro-fibers present in hardened RPCMs prevent micro-cracks, induced by plastic shrinkage, from developing into macro-cracks. These fibers bridge material and therefore hold together the existing macro-cracks, thus reinforcing the mortar against failure. Good performance of RPCMs can be largely attributed to the crack bridging ability provided by the micro-fibers, which limit crack opening and distribute the stresses to the nearby matrix, thus suppressing strain occurrence. Moreover, the application of polymers in concrete also helps to bridge micro-cracks [16].

Plastic shrinkage occurs up to the moment when concrete is set. It depends on the amount of water lost on the concrete's surface, which in turn is influenced by the temperature, relative humidity and wind speed. Plastic shrinkage is higher, if cement content is higher in the concrete mix and the water to cement ratio is lower [17]. The mortar cracking due to shrinkage depends on three parameters: shrinkage deformation (ε), Young's modulus (E) and tensile strength (f_{Rt}). During plastic shrinkage, low tensile stresses (σ_t) are induced for the very low Young's modulus and it is therefore sufficient, by the addition of micro-fibers, to raise slightly f_{Rt} the cementitious composite until it becomes greater than σ_t induced by the shrinkage. In case of the drying shrinkage, an addition of micro-fibers is not sufficient to reach levels above σ_t, where Young's modulus is higher.

4.2. Effective repair related to the presence of polymer adhesives

The modification of concrete using polymers allows improving some of its properties, such as tensile and flexural strength, adhesion to different substrates and tightness [1]. The polymers may be added in the form of dispersion, often called latexes [6]. Latex adhesives exist as water emulsions and are added to the Portland cement mixtures of the RPCMs. The water reacts with cement and hydration takes place. The latex particles improve the stability of the mortars. Latexes increase tensile and bending strengths and primary adhesive properties on concrete surfaces. Moreover, latex addition allows reducing the formation of voids and cracks during the curing stage [18]. Other forms of additions include emulsions, redispersible powders, water solutions of polymers as well as liquid synthetic resins [5].

4.3. Effective repair related to volumetric stability and adhesion

Shrinkage tests have shown that three mortars exhibited volumetric stability for 45 days. RPCM-B and RPCM-C have had expansion within first days. The expansive binders compensate the shrinkage and prevent the separation of mortar-concrete interface or cracks formation in the mortar due to the shrinkage. The consequence would be a mortar detachment caused by its movement in relation with the old concrete. The situation, that frequently occurs, is when the mortar tends to shrink, but it cannot move because of friction presence: a stress (σ) is established, which leads to cracking of mortar. Because of the expansive binders reaction with water and other products present in the fresh mixture, mortar increases in volume while setting and curing. Currently calcium oxide and magnesium oxides are added to mortars as expansive agents (EXP) together with shrinkage reducing admixtures (SRA) like propyleneglycol ether in order to ensure stable and durable mortars [19]. While drying, shrinkage causes the reduction or decrease in compressive stresses accumulated during the initial expansion. The adhesion of the repair layer is effective if it enables the load transfer (from substrate) and ensures even distribution of stresses. In fact, stress concentration, induced by shrinkage during setting, is mainly located at the mortar-concrete interface.

In this investigation, based on the obtained results, the following parameters were calculated: concrete tensile strength f_{Ct} equal to 2.9 MPa (it was obtained from the formula $f_{ctm} = 0.30 f_{ck}^{\frac{2}{3}}$, according to Eurocode 2 [16] for C ≤ 50/60 classes); repair material tensile strength f_{Rt} equal to 7.6 MPa (it was obtained by $f_{ctm} = \frac{f_{ctm,fl}}{\left(1.6 - \frac{h}{1000}\right)}$, according to Eurocode 2 [20]); repair material adhesion strength f_{Ra} equal to 3.9 MPa. Comparing the above values, it is possible to correlate the following relation:

$$\sigma_t < f_{Ct} < f_{Ra} < f_{Rt}$$

which allows to state that RPCM requirements are higher than those of standard cement concrete ones according to the current standards.

5. Conclusions

Based on the test results and literature data, the following conclusions can be drawn:

- Currently used RPCMs may be successfully applied for repairing deteriorated concrete covers of structures due to their very good mechanical properties.
- The addition of micro-fibers and polymers prevents micro-cracks and helps to resist the induced shrinkage stresses.
- The presence of polymers in repair materials can significantly improve their properties such as the flexural strength and bond strength.

References

[1] Łukowski P., *Adhesion of polymer-cement concretes to the substrate*, Cement Lime Concrete, 3, 2005.

[2] Kovács T., *Deterioration of reinforced concrete repair mortar layers*, Periodica Polytechnica Ser. Civ. Eng. 44:197-206, 2000.

[3] Jumaat M.Z., Kabir M.H., Obaydullah M., *A review of the repair of reinforced concrete beams*, Journal of Applied Science Research 2(6):317-326, 2006.

[4] Guide to concrete repair. United States Department of the Interior Bureau Reclamation. Technical Service Center, 1997.

[5] Czarnecki L., *Polymer Concretes*, Cement Lime Concrete, Issue 2, 2010.

[6] Products and systems for the protection and repair of concrete structure. Definitions, requirements, quality control and evaluation of conformity. General principles for use of products and systems. UNI EN 1504-9:2008.

[7] Methods of test for mortar for masonry. Bulk sampling of mortars and preparation of test mortars. EN 1015-2.

[8] PN-EN 196-1:1996 Methods of testing cement – Determination of strength (in Polish).

[9] Methods of test for mortar for masonry. Determination of flexural and compressive strength of hardened mortar. EN 1015-11.

[10] Products and systems for the protection and repair of concrete structures. Test methods. Measurement of bond strength by pull-off. EN 1542.

[11] Products and systems for the protection and repair of concrete structures. Test methods. Reference concretes for testing. EN 1766.

[12] Grout – Requirements and test methods. OENORM B 3329:2009.

[13] Al-Zahrani M.M., Maslehuddin M., Al-Dulaijan S.U., Ibrahim M., *Mechanical properties and durability characteristics of polymer- and cement-based repair materials*, Cement & Concrete Composites 25 (2003) 527–537.

[14] Structural and non-structural repair. EN 1504-3.

[15] Folliot A., Buil L., *La structuration progressive de la pierre de ciment*, [in:] *Le bétonhydraulique: connaissance et pratique*, Presse de l'ENPC Paris 1982.

[16] Łukowski P., *Polymer-cement mortars with improved adhesion to concrete substrates*, Restoration of Buildings and Monuments, 4/5, 2010

[17] Neville A.M., *Properties of concrete*, Fourth Edition, Wiley, 1996.

[18] Guide for the selection of polymer adhesives with concrete reported by ACI Committee 503. ACI 503. 5R-92, reapproved 2003.
[19] Maltese C., Pistolesi C., Lolli A., Bravo A., Cerulli T., Salvioni D., *Combined effect of expansive and shrinkage reducing admixtures to obtain stable and durable mortars*, Cement and Concrete Research, vol. 35, 2005, 2244–2251.
[20] Eurocode 2. Design of concrete structures – Part 1-1: General rules and rules for buildings. UNI EN 1992-1-1:2005.

TECHNICAL TRANSACTIONS | CZASOPISMO TECHNICZNE
CHEMISTRY | CHEMIA
1-Ch/2015

MARIA KURAŃSKA, ALEKSANDER PROCIAK*

FLAX FIBERS AS NATURAL FILLER FOR RIGID POLYURETHANE-POLYISOCYANURATE FOAMS BASED ON BIO-POLYOL FROM RAPESEED OIL

WŁÓKNA LNIANE JAKO NATURALNY NAPEŁNIACZ DO SZTYWNYCH PIANEK POLIURETANOWO-POLIIZOCYJANUROWYCH Z UDZIAŁEM BIO-POLIOLU Z OLEJU RZEPAKOWEGO

Abstract

The influence of flax fibers on the physical and mechanical properties and the flammability of rigid polyurethane-polyisocyanurate foams obtained from rapeseed oil-based polyol was analyzed. The rigid polyurethane-polyisocyanurate foams with apparent density of 40−48 kg/m^3 were prepared. It has been found that the introduction of flax fiber has a beneficial effect on selected properties of obtained foams.

Keywords: *polyurethane- polyisocyanurate rigid foams, rapeseed oil-based polyols, thermal conductivity, mechanical properties, flammability, thermal stability, cellular structure*

Streszczenie

Analizowano wpływ włókien lnianych na właściwości fizykomechaniczne oraz palność sztywnych pianek poliuretanowo-poliizocyjanurowych otrzymanych z udziałem bio-poliolu z oleju rzepakowego. Otrzymano porowate materiały poliuretanowo-poliizocyjanurowe o gęstościach pozornych w zakresie 40−48 kg/m^3. Stwierdzono, że wprowadzenie włókien lnianych wpływa korzystnie na wybrane właściwości otrzymanych pianek.

Słowa kluczowe: *sztywne pianki poliuretanowo-poliizocyjanurowe, poliole z oleju rzepakowego, współczynnik przewodzenia ciepła, właściwości mechaniczne, palność, stabilność termiczna, struktura komórkowa*

DOI: 10.4467/2353737XCT.15.104.4052

* Ph.D. Eng. Maria Kurańska, Ph.D. D.Sc. Eng. Aleksander Prociak, prof. CUT, Department of Chemistry and Technology of Polymers, Faculty of Chemical Engineering and Technology, Cracow University of Technology.

1. Introduction

Nowadays, polyurethanes (PURs) are everywhere in everyday life, in such applications as car seats, insulation materials, packaging, foot wear, construction, furniture and so on [1]. PUR can be used mainly as foams, surface coatings, elastomers, adhesives, artificial and synthetic leathers and fibers. Polyurethane foams can be divided into three major classes: rigid, semi-rigid and flexible [2].

Rigid PUR foams are useful as insulating materials due to their low coefficient of thermal conductivity, and good physical-mechanical properties [3]. Traditional rigid PUR foams are synthesized by the reaction of polyols and diisocyanates. Both components are derived mainly from petroleum resources which are diminishing rapidly. The current research has been focused on developing polyols synthesis from renewable raw materials [4, 5]. Several methods and their modifications have been reported for converting natural oils (e.g. soybean, rapeseed, palm) into polyols [613]. Other natural renewable products, such as natural fibers, are also used in the modification of rigid PUR foams [14–16]. In previous work, Prociak et al. analyzed the influence of rapeseed oil-based polyol and flax fibers on properties of rigid PUR foams. They have found the possibility to increase the amount of biodegradable raw materials in the formulation of rigid PUR foams without deteriorating their physical-mechanical properties [17]. Yuan et al. modified PUR foams with wood flours to improve their properties and to reduce the cost of foams production. The introduction of wood flour improved the compressive property of PUR foams, whereas its tensile and flexural properties were reduced. The thermal stability of the PUR foams was improved with the addition of wood flour [18].

Another important concern is thermal stability of PUR foams. An improvement of foams, thermal stability can be achieved through introduction, into the PUR matrix, of isocyanurate rings, which are more stable from thermodynamic point of view than urethane bonds [19].

This paper describes the influence of the flax fiber on the properties of rigid PUR-PIR foams based on bio-polyols obtained from rapeseed oil.

2. Experimental part

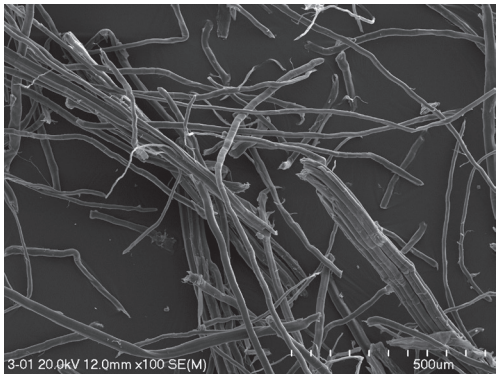

Fig. 1. SEM microphotograph of flax fibers

The polyurethane-polyisocyanurate (PUR-PIR) foams were obtained by mixing two components (A and B). The chemical compositions of component A consisted of a bio-polyol, petrochemical polyol (Lupranol 3422), catalysts (Polycat 5 and potassium acetate 30%), surfactant (L-6915) and chemical blowing agent (water). This formulation was modified with flax fibers (3 and 6 wt.%). Natural fibers, before adding to the polyol premix, were fractionated, and then dried to constant weight. The maximum length of flax fibers was 0.5 mm. The amount

of introduced fibers was limited due to the increasing of component A viscosity. The SEM microphotography of flax fibers was shown in Fig. 1.

In prepared foams 70 wt.% of petrochemical polyol was replaced by rapeseed oil-based polyol (RP). A two-step process was used for the preparation of RP. In the first step, unsaturated fatty acids in triglycerides reacted with acetate peroxyacid to form epoxidized oil. Through the epoxidation, the double bonds of the triglycerides were transformed into oxirane rings. In the second step, the epoxidized oil was converted into a polyol using diethylene glycol (DEG). RP has been prepared in the Department of Chemistry and Technology of Polymers. The isocyanate indices were 150 and 250. The rigid PUR-PIR foams were marked with respect to isocyanate index and content of flax fibres (e.g. RP150/F3, RP250/F3). The foams were obtained using the one-shot and free rise method. Foams were prepared in two different moulds that allowed free rise of reaction mixture in vertical and horizontal directions respectively.

The foams were conditioned at 22°C and in 50% relative humidity for 24 hours, before being cut for analysis. The morphology of cells was analyzed using a scanning electron microscope (HITACHI S-4700). The samples were sputter coated with graphite before testing to avoid charging. The apparent density of PUR-PIR foams was determined according to ISO 845. Thermal conductivity factors – λ values (mW/m·K) were estimated using Laser Comp Heat Flow Instrument Fox 200. The average temperature of measurements was 10°C (the temperature of cold plate was 0°C and of warm plate 20°C). Closed cells content (%) was determined according to ISO 4590. Compressive strength was measured according to ISO 826 and compressive force was applied at the speed of 2 mm/s. Compressive strength has been investigated in two directions: parallel (z) and perpendicular (x) to the direction of the foam rise. Thermal stability was studied by means of thermogravimetric analysis under nitrogen flow and the heating rate of 10°C/min from room temperature to 1000°C. During this test, the following parameters were determined: thermal degradation onset temperature (T_{onset}), the temperature at which thermal degradation reached 25 and 50% by weight of the sample ($T_{25\%}$, $T_{50\%}$). The behavior of rigid PUR-PIR foams under heat flux of 35 kW/m^2 during 300 s was tested using FTT Dual Cone Calorimeter (Fire Testing Technology Ltd., UK). Tests were done according to ISO 5660-1 standard. During the experiments, the time required to initiate the reaction of combustion and such parameters as average heat rate release (HRR), total heat release (THR), and total smoke released (TSR) were measured. The oxygen index (LOI) was determined according to ISO 4589-2.

3. Results and discussion

The basic physical-mechanical properties of PUR-PIR foams are shown in Table 1. The largest change in the apparent density of the foams was observed in the case of foam with isocyanate index of 250 and flax fibers in the amount of 6 wt.%. Changing the foams apparent density may be associated with high viscosity of the polyol premix.

The introduction of flax fiber into PUR-PIR matrix had beneficial effect on the mechanical properties of foams with isocyanate index of 250. Such effect can be associated with the size of foam cells. Rigid PUR-PIR foams obtained with isocyanate index of 250 were characterized by bigger cells in comparison to cells of foams with isocyanate index of 150 (Fig. 2).

Table 1

Physical-mechanical properties of rigid PUR-PIR foams prepared in vertical mould

Symbol	Apparent density, [kg/m^3]	Compressive strength [MPa]		Young' modulus [MPa]	
		z	*x*	*z*	*x*
RP150	43.9	0.32	0.23	5.89	3.94
RP150/F3	42.0	0.26	0.19	5.49	3.89
RP150/F6	39.5	0.21	0.14	4.69	3.24
RP250	43.5	0.26	0.24	6.02	4.36
RP250/F3	43.2	0.28	0.24	6.65	4.79
RP250/F6	48.2	0.30	0.25	6.05	5.00

z, *x* – parallel and perpendicular respectively to foam rise direction.

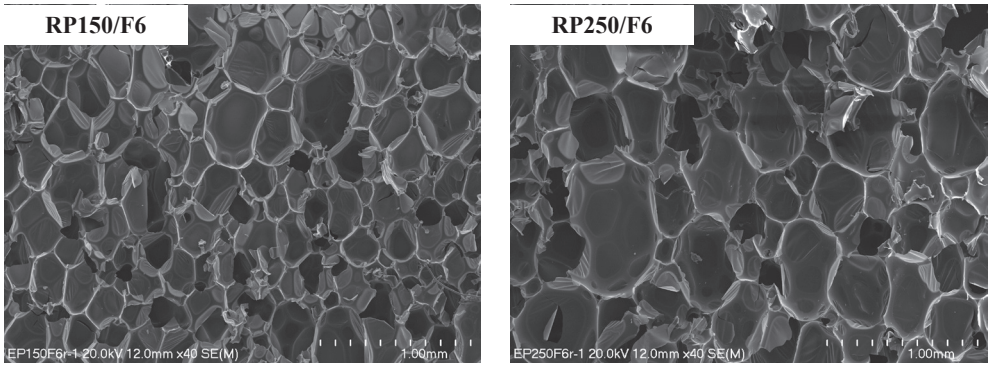

Fig. 2. SEM microphotographs of selected PUR-PIR foams

Larger cell size allows for the incorporation of filler in the cell wall, while in the case of smaller cells, the filler can break down the foam cells (Fig. 3).

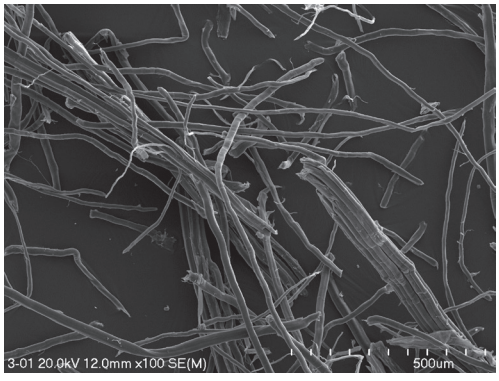

Fig. 3. SEM microphotographs of foams modified with flax fiber

Materials obtained in horizontal mould had higher apparent density than foams shown in Table 2.

Table 2

Selected properties of rigid PUR-PIR foams obtained in horizontal mould

Symbol	Apparent density [kg/m^3]	Content of closed cells [%]	Coefficient of thermal conductivity [mW/m·K]
RP150	49.6	96.5	22.72
RP150/F3	49.0	97.3	23.66
RP150/F6	54.0	94.9	24.00
RP250	48.7	91.9	23.19
RP250/F3	54.3	93.8	23.80
RP250/F6	67.5	94.8	25.12

It is caused by the fact that the apparent density of the materials obtained in the horizontal mould was determined with the so-called "peel" where the concentration of the material occurs. All of the foams are characterized by high content of closed cells, which is very important in the case of heat insulating materials. The incorporation of flax fibers to PUR-PIR matrix caused a slight increase of the thermal conductivity coefficient, what is an effect of foams apparent density increase.

Rigid foams are used in the construction industry. Therefore, it is important to analyze the influence of filler on the flammability of obtained materials (Table 3).

Table 3

Influence of flax fibres on flammability of rigid PUR-PIR foams

	Time to ignition [s]	Total heat release [MJ/m^2]	Heat release rate peak [kW/m^2]	Total smoke release [m^2/m^2]	Oxygen index [%]
RP150	2	15.68	206.5	654.1	22.4
RP150/F3	4	14.75	211.6	705.2	22.0
RP150/F6	3	15.08	215.3	689.7	21.8
RP250	3	16.90	138.3	545.6	23.5
RP250/F3	6	16.34	135.0	433.4	23.2
RP250/F6	4	18.66	152.7	613.0	23.0

In the case of the cone calorimetry test method, there was no significant correlation depending on amount of the flax fiber in PUR-PIR matrix. The oxygen index slightly decreased with an increasing amount of flax fibers.

It is important that the flax fiber has not significantly increased the flammability of obtained materials, as it was also confirmed by the rate of heat release during combustion of the sample (Fig. 4).

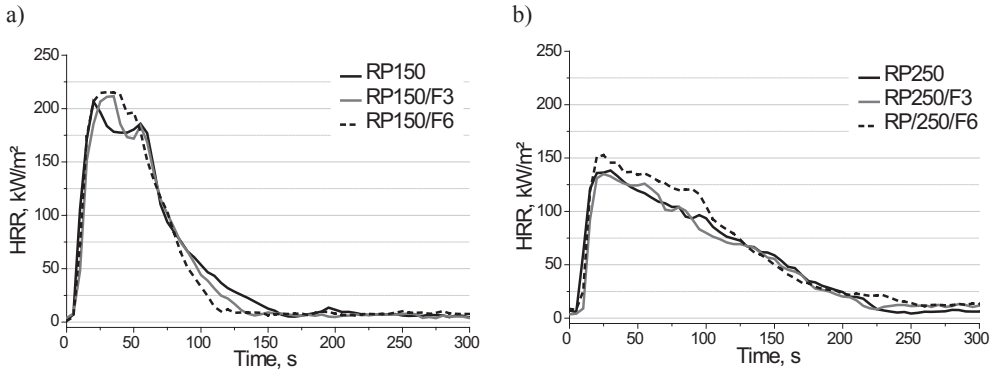

Fig. 4. Influence of flax fibers on heat rate release of rigid PUR-PIR foams with isocyanate index 150 (a) and 250 (b)

The introduction of fiber does not significantly affect the course of thermal degradation, which can be seen on the thermograms (Fig. 5).

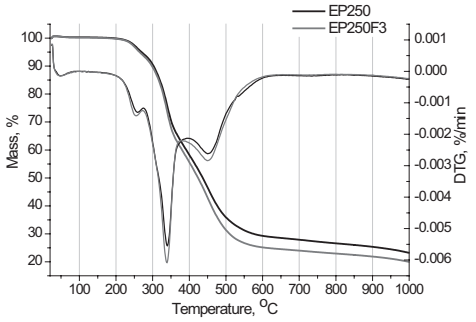

Fig. 5. Thermograms TG and DTG rigid PUR-PIR foams modified and unmodified with flax fibers with isocyanate index 250

Determined from the thermograms, the temperature at which 5 and 25% weight loss occur leads to the conclusion that flax fibers increase thermal stability of the foams (Table 4).

The mechanism of thermal degradation of PURs is a very complex process. The isocyanurate linkage has higher thermal stability than that of the urethane linkage (urethane dissociates at approx. 200°C as opposed to 350°C for polyisocyanurates). Polymers based on isocyanate provide thermal stability in the following order: isocyanurate (350°C) > urea (250°C) > urethane (200°C) > biuret (135–140°C) > allophanate (106°C) [20, 21].

Table 4

Thermal properties of selected samples

Symbol	T_{onset}	$T_{25\%}$ [°C]	$T_{50\%}$ [°C]	Residue [%]
RP250	232	232	341	23.2
RP250/F3	230	337	423	20.0

4. Conclusions

The study has shown that polyol from rapeseed oil and flax fibers are raw materials, which can be successfully used in the synthesis of rigid polyurethane-polyisocyanurate foams. The replacement of petrochemical polyol with the amount of 70 wt.% of rapeseed oil-based polyols and the addition of flax fibers to foams with isocyanate index of 250 allows to increase the compressive strength. The addition of flax fibers slightly increases thermal conductivity, which is the effect of apparent density increase. On the other side the addition of flax fibers improves thermal stability of rigid polyurethane-polyisocyanurate foams.

The research leading to these results has received funding from the ERA-Net MATERA project BBPM. "Bio-Based Polyurethane Materials".

References

[1] Tu Yuan-Chan, Kiatsimkul P., Suppes G., Hsieh Fu-Hungi, *Physical Properties of Water-Blown Rigid Polyurethane Foams from Vegetable Oil-Based Polyols*, Journal of Applied Polymer Science, Vol. 105(2), 2007, 453–459.

[2] Li-Ting Yang, Cheng-Shan Zhao, Chun-Lan Dai, Li-Yu Fu, Shao-Quan Lin, *Thermal and Mechanical Properties of Polyurethane Rigid Foam Based on Epoxidized Soybean Oil*, Journal of Polymers and the Environment, Vol. 20(1), 2012, 230–236.

[3] Yeol L.J., Dukjoon K., *Desaminated Glycolysis of water-Blown Rigid Polyurethane Foams*, Journal of Applied Polymer science, Vol. 77(12), 2000, 2646–2656.

[4] Palanisamy A., Karuna M.S.L., Satyavani T., Rohini Kumar D.B., *Development and Characterization of Water-Blown Polyurethane Foams from Diethanolamides of Karanja Oil*, Journal of the American Oil Chemists' Society, Vol. 88(4), 2011, 541–549.

[5] Ionescu M., Petrovic Z.S., Wan X., *Ethoxylated Soybean Polyols for Polyurethanes*, Journal of Polymers and The Environment, Vol. 15(4), 2007, 237–243.

[6] Pawlik H., Prociak A., Pielichowski J., *Synteza polioli z oleju palmowego przeznaczonych do otrzymywania elastycznych pianek poliuretanowych*, Czasopismo Techniczne, 1-Ch/2009, 111–117.

[7] Prociak A., Rojek P., Pawlik H., Kurańska M., *Synteza poliuretanów z udziałem surowców odnawialnych*, Przemysł Chemiczny, Vol. 90(7), 2011, 1376–1381.

[8] Rojek P., Prociak A., *Effect of different rapeseed-oil-based polyols on mechanical properties of flexible polyurethane foams*, Journal of Applied Polymer Science, Vol. 125(4), 2012, 2936–2945.
[9] Prociak A., *Properties of polyurethane foams modified with natural oil-based polyols*, Cellular Polymers, Vol. 26(6), 2007, 381–392.
[10] Kirpluks M., Cabulis U., Kurańska M., Prociak A., *Three Different Approaches for Polyol Synthesis from Rapeseed Oil*, Key Engineering Materials, Vol. 559, 2013, 69–74.
[11] Kurańska M., Prociak A., Kirpluks M., Cabulis U., *Polyurethane–polyisocyanurate foams modified with hydroxylderivatives of rapeseed oil*, Industrial Crops and Products, Vol. 74, 2015, 887–897.
[12] Cabulis U., Kirpluks M., Stirna U., Lopez M.J., Carmen Vargas-Garcia M., Suarez-Estrella F., Moreno J., *Rigid polyurethane foams obtained from tall oil and filled with natural fibers: Application as a support for immobilization of lignin-degrading microorganisms*, Journal of Cellular Plastics, Vol. 48(6), 2012, 500–515.
[13] Zieleniewska M., Auguścik M., Prociak A., Rojek P., Ryszkowska J., *Polyurethane-urea substrates from rapeseed oil-based polyol for bone tissue cultures intended for application in tissue engineering*, Polymer Degradation and Stability, Vol. 108, 2014, 241–249.
[14] Zhu M., Bandyopadhyay-Ghosh S., Khazabi M., Cai, Correa C., Sain M., *Reinforcement of Soy Polyol-Based Rigid Polyurethane Foams by Cellulose Microfibers and Nanoclays*, Journal of Applied Polymer Science, Vol. 124(6), 2012, 4702–4710.
[15] Kurańska M., Prociak A., *Porous polyurethane composite with natural fibres*, Composite Science and Technology, Vol. 72, 2012, 299–304.
[16] Kurańska M., Prociak A., Kirpluks M., Cabulis U., *Porous polyurethane composites based on bio-components*, Composites Science and Technology, Vol. 75, 2013, 70–76.
[17] Prociak A., Michałowski S., *Sztywne pianki poliuretanowe modyfikowane surowcami odnawialnymi*, Czasopismo Techniczne. Chemia, Vol. 3, 2009, 250–253.
[18] Yuan Jiang, Sheldon Shi Q., *Effect of the Addition of Wood Flours on the Properties of Rigid Polyurethane Foam*, Journal of Applied Polymer Science, Vol. 113(5), 2009, 2902–2909.
[19] Modesti M., Lorenzetti A., Simioni F., Checchin M., *Influence of different flame retardants on fire behaviour of modified PIR/PUR polymers*, Polymer Degradation and Stability, Vol. 74, 2001, 475–479.
[20] Chattopadhyay D.K., Webster D.C., *Thermal stability and flame retardancy of polyurethanes*, Progress in Polymer Science, Vol. 34(10), 2009, 1068–1133.
[21] Mosiewicki M.A., Dell'Arciprete G.A., Aranguren M.I., Marcovich N.E., *Polyurethane Foams Obtained from Castor Oil-based Polyol and Filled with Wood Flour*, Journal of Composite Materials, Vol. 43(25), 2009, 3057–3072.

TECHNICAL TRANSACTIONS | CZASOPISMO TECHNICZNE
CHEMISTRY | CHEMIA
1-Ch/2015

BARBARA LARWA, KRZYSZTOF KUPIEC, TADEUSZ KOMOROWICZ,
KRZYSZTOF NEUPAUER*

HEAT CONDUCTION IN THE GROUND UNDER NATURAL CONDITIONS AND WITH HEAT EXCHANGER INSTALLED

PRZEWODZENIE CIEPŁA W GRUNCIE W WARUNKACH NATURALNYCH I PRZY ZAINSTALOWANYM WYMIENNIKU CIEPŁA

Abstract

The results of calculations of the heat transfer in a horizontal ground heat exchanger are presented. The applied model is based on a one-dimensional equation of the transient heat conduction with an internal heat source. The model was correctly verified by comparison of computational results and experimental measurements presented in literature. Thermal calculations concerning heat transfer in the ground under natural conditions are also presented.

Keywords: horizontal ground heat exchangers, transient heat conduction

Streszczenie

Przedstawiono wyniki obliczeń przenoszenia ciepła w poziomym gruntowym wymienniku. Model użyty w obliczeniach oparto na jednowymiarowym równaniu nieustalonego przewodzenia ciepła z wewnętrznym źródłem. Model został zweryfikowany przez porównanie wyników obliczeń z wynikami pomiarów przedstawionymi w literaturze. Przeprowadzono również obliczenia dotyczące przenoszenia ciepła w gruncie w warunkach naturalnych.

Słowa kluczowe: poziome gruntowe wymienniki ciepła, nieustalone przewodzenie ciepła

DOI: 10.4467/2353737XCT.15.105.4053

* M.Sc. Eng. Barbara Larwa, Ph.D. D.Sc. Eng. Krzysztof Kupiec, prof. CUT, Ph.D. Eng.Tadeusz Komorowicz, PhD. Eng. Krzysztof Neupauer, Department of Chemical and Process Engineering, Faculty of Chemical Engineering and Technology, Cracow University of Technology.

Nomenclature

a (= $k/(c\rho)$)	–	thermal diffusivity of the ground [m^2/s]
A_g	–	surface area of the ground [m^2]
B	–	half of the annual maximum temperature range [K]
Bi	–	Biot number
C_1, C_2	–	constants dependent on the Biot number
c	–	heat capacity of the ground [J/(kgK)]
F	–	heat flux [W/m^2]
h	–	distance between the heat exchanger and the ground surface [m]
h_0	–	heat transfer coefficient [W/(m^{2}K)]
k	–	thermal conductivity of the ground [W/(mK)]
L	–	characteristic length [m]
m	–	number of stages
$\dot{m}$	–	mass flow rate [kg/s]
q	–	total amount of heat per unit area of the ground [J/m^2]
q_y	–	rate of heat generation per unit of volume [W/m^3]
$\dot{Q}$	–	rate of heat transfer [W]
t	–	time [days]
t_c	–	cycle time [days]
t_{max}	–	time from the beginning of the year until the maximum ambient temperature is reached [days]
T	–	temperature [°C]
T_b	–	temperature of the ground at great depth [°C]
x	–	position coordinate [m]
ρ	–	ground density [kg/m^3]
ω	–	frequency [1/s]

Indices

0	–	ground surface
a	–	ambient (environment)
g	–	ground
L	–	working fluid
$\bar{}$	–	average value

1. Introduction

The ground is an advantageous heat source for heat pumps. Compared to air, the ground has a much more stable temperature and a high specific heat.

The heat is transported between a ground surface and the environment (atmospheric air). The direction of heat transfer depends on the relation between the ground temperature and the ambient temperature. In the warmer half of the year, the air temperature is higher than the ground temperature; inversely in the cooler half of the year. The greater the temperature difference between the ground surface and the environment, the greater the heat flux transferred.

Cyclicality of the air temperature changes cause the temperature of the ground below a certain depth (about 10 m) to be equal to the average ambient air temperature. On the other hand, the temperature of the sub-surface of the ground varies both with time as well as with the position (depth). The installation of a ground heat exchanger at the shallow depth of the ground (embedded horizontally) along with receiving or transferring the heat with its utilization disrupts the natural cycle of ground temperature changes. During receiving of the heat from the ground in heating season, the ground temperature lowers. Due to the small installation depth of a horizontal heat exchanger, those temperature changes also apply to the ground surface. The cooling of the ground surface causes an increase in the temperature difference between the air and ground surface and thus the ground then takes more heat than it does under natural conditions. Vertical exchangers do not have this beneficial feature as the cold ground at great depth is not able to compensate the heat loss by receiving heat from the environment.

Horizontal ground heat exchangers have been widely used in many countries as a heat source for ground-source heat pump systems. Therefore, ground heat exchangers are a subject of many experimental and numerical studies [1–6].

The subject of this paper is to present the results of thermal calculations concerning horizontal ground heat exchangers. The calculations were performed on the basis of the solution of equations of the mathematical model of the process. The ground was considered as a semi-infinite body with an internal heat source, wherein, it has been taken into account that atmospheric air has a temperature changing periodically in time. The presented results can be used to simulate ground heat exchangers under different conditions.

2. Analytical solutions of transient heat conduction in the ground

The sub-surface of the ground was considered as a semi-infinite body limited from the top by the ground surface. The heat conduction equation has the form:

$$\frac{\partial T}{\partial t} = a\frac{\partial^2 T}{\partial x^2} + \frac{q_v}{c\rho} \tag{1}$$

If the ground heat exchanger is not installed $q_v = 0$.

It was assumed that the heat between the ground and the environment is transferred by convection; the boundary condition for the surface of the ground is as follows:

$$x = 0 \qquad L\frac{\partial T}{\partial x} = -\mathrm{Bi}\left(T_a - T\right) \tag{2}$$

where Bi is the Biot number characterizing the ratio between the internal and external resistances to heat transfer, defined as follows:

$$\mathrm{Bi} = \frac{h_0 L}{k} \tag{3}$$

The quantity L (with length dimension) is defined as below:

$$L = \sqrt{\frac{2a}{\omega}} \tag{4}$$

A boundary condition relates to the ground at a great depth where the temperature is constant. The condition is following:

$$x \to \infty \qquad T = T_b \tag{5}$$

The ambient temperature T_a changes periodically according to the relationship:

$$T_a = \bar{T}_a + B \cdot \cos\left[\omega\left(t - t_{\max}\right)\right] \tag{6}$$

wherein the values $\bar{T}_a$ and T_b are the same. A frequency ω is equal to:

$$\omega = \frac{2\pi}{t_c} \tag{7}$$

where t_c is the cycle time (365 days). For a cyclic steady state the equation (1) with combination with (2), (5) and (6) has an analytical solution. The relationship of the ground temperature in the function of the time and position has the form [7]:

$$T = T_b + BC_1 \cdot \exp\left(-\frac{x}{L}\right) \cdot \cos\left[\omega\left(t - t_{\max}\right) - \frac{x}{L} - C_2\right] \tag{8}$$

where C_1 and C_2 depend on the Biot number:

$$C_1 = \frac{\mathrm{Bi}}{\sqrt{\left(\mathrm{Bi}+1\right)^2 + 1}} \tag{9}$$

$$C_2 = \tan^{-1}\left(\frac{1}{\mathrm{Bi}+1}\right) \tag{10}$$

In Figs. 1a and b, the temperature profiles in the ground, determined according to relationship (8), are presented. The ground temperature profiles are shown in 3-month intervals (January, April, July, October). The calculations were performed for Bi = 2 and Bi $\to \infty$. As one can see from the Figs. 1a and b for $x/L > 5$, the temperatures change slightly. In addition, for smaller values of Bi the temporal variations of temperatures in the sub-surface layers of the ground become less significant.

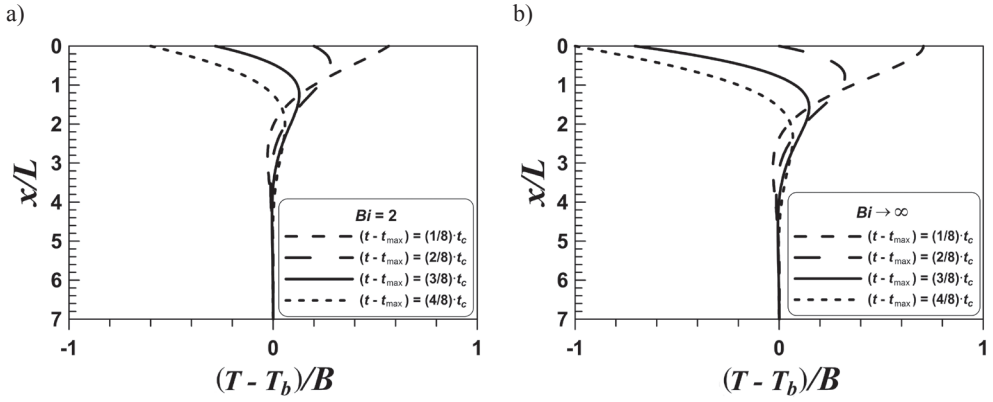

Fig. 1. Ground temperature profiles for a) Bi = 2, b) Bi → ∞

The temperature gradient on the ground surface can be obtained by differentiation of formula (8):

$$L\left(\frac{\partial T}{\partial x}\right)_{x=0} = -\sqrt{2}\,BC_1 \cdot \cos\left[\omega\left(t - t_{\max}\right) - C_2 + \frac{\pi}{4}\right] \tag{11}$$

The heat flux on the surface of the ground, in accordance with the Fourier equation, is:

$$F = -k\left(\frac{\partial T}{\partial x}\right)_{x=0} \tag{12}$$

This flux can be determined by calculation of the temperature gradient at the ground surface. One gets:

$$F = \sqrt{2}\,\frac{kBC_1}{L} \cdot \cos\left[\omega\left(t - t_{\max}\right) - C_2 + \frac{\pi}{4}\right] \tag{13}$$

The maximum heat flux is a follows:

$$F_{\max} = \sqrt{2}\,\frac{kBC_1}{L} \tag{14}$$

The time, after the heat flux reaches the maximum value is following:

$$t = t_{\max} + t_c\left(\frac{C_2}{2\pi} - \frac{1}{8}\right) \tag{15}$$

For a time higher by $t_c/2$ than the time specified above (i.e. after a half-year period), the heat flux reaches the value according to the formula (14), but with the opposite sign (minimum function) − this applies to the transport of heat from the ground to the environment.

Temporal changes in the heat flux between the ground and the environment can be determined from relationship (13) and are shown in Fig. 2. The effect of the Biot number, inversely proportional to the external thermal resistance, was analyzed. The greater the external thermal resistance, the smaller the heat flux between the ground and the environment for certain values of B, k and L. The value of the external thermal resistance affects not only the heat flux, but also the date of occurrence of the maximum flux. For B = 11 K, k = 1.5 W/(mK), L = 2.24 m and t_{max} = 182 days (the warmest day in the year − 1st of July) exemplary values can be read from the graph. If the external thermal resistance can be neglected, the maximum heat flux F_{max} = 9.5 W/m^2 ($F_{max}L/(kB)$ = 1.41) is reached on the 14th of May. This date is 46 days before the warmest day of the year, while for Bi = 2 the maximum value of heat flux is F_{max} = 6.6 W/m^2 ($F_{max}L/(kB)$ = 0.89) and it is reached 24 days later.

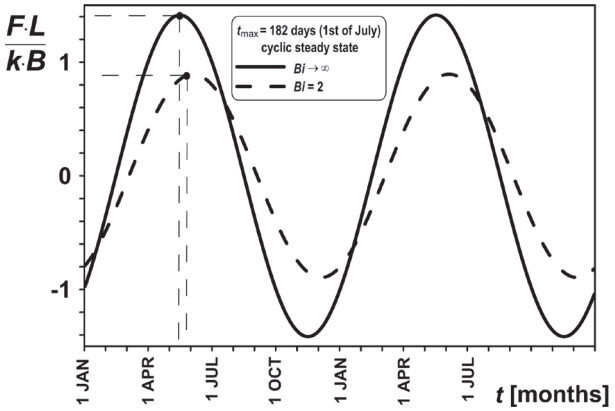

Fig. 2. Temporal variation of heat flux to/from the ground surface

The integration of the heat flux over time leads to the determination of the amount of heat q transported to/from the ground per unit area. The limits of integration for heating the ground (including the half-year period) result from the condition $\left(\partial T/\partial x\right)_{x=0} < 0$. Therefore, the values of the cosine function (13) are positive. In the next half-year period, the temperature gradient at the surface of the ground is positive, the values of cosine function are negative and the ground transfers the heat to the environment ($q < 0$). The resulting lower limit of integration (when the ground is heated) is $t_{max} + (C_2 - 3\pi/4)/\omega$ and the upper is $t_{max} + (C_2 + \pi/4)/\omega$. As a result of integration one gets:

$$q = \int_{t_{max}+(C_2-3\pi/4)/\omega}^{t_{max}+(C_2+\pi/4)/\omega} F \cdot dt = 2BC_1D \tag{16}$$

where:

$$D = \sqrt{\frac{kc\rho}{\omega}} \tag{17}$$

Fig. 3 refers to the total amount of heat per unit area of the ground q, for that half of the year when the direction of heat transfer does not change (in the warmer half of the year). The relationship between q and the product ($kc\rho$) for various values of B and Bi are presented. The calculations were carried out for $\omega = 0.199 \cdot 10^{-6}$ s^{-1}. With the increase in the values of ($kc\rho$), B and Bi the amount of heat taken over by the ground during the warmer half of the year increases. Exemplary for B = 11 K, k = 1.5 W/(mK), $c\rho$ = 6.5 MJ/(m^{3}K)) and Bi = 2 one obtains q = 97.4 MJ/m^2, whereas for Bi → ∞ a higher value is obtained: q = 158 MJ/m^2.

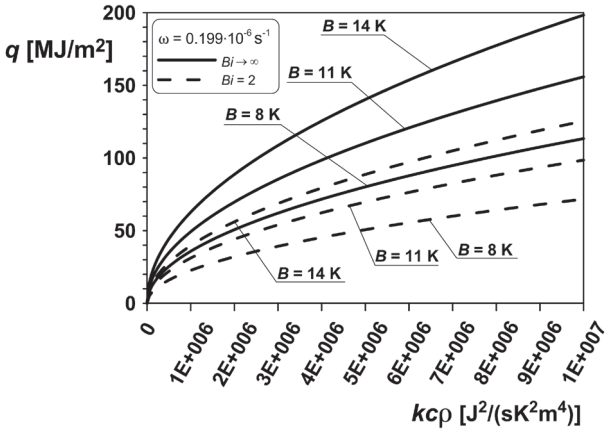

Fig. 3. The effect of product ($kc\rho$), B and Bi on the amount of heat taken over by the ground

By knowing the temperature profiles in the ground, one can determine the average temperature of the sub-surface layer of the ground. This quantity has an apparent sense because its value depends on the depth of the ground layer which is considered to be the sub-surface layer (below the sub-surface layer the ground has a temperature approximately independent of the time and position). It is assumed in calculations that the thickness of the sub-surface layer is 2π-fold higher than the characteristic linear dimension. The average temperature of the sub-surface layer of the ground was calculated according to the formula:

$$\overline{T} = T_b + \frac{1}{2\pi}\int_0^{2\pi} \Delta T \, dX \tag{18}$$

where: $\Delta T = T - T_b$. Substituting (8) to (18) one gets after integration:

$$\bar{T} = T_b + \frac{BC_1}{4\pi}\left\{\sin\left[\omega\left(t - t_{\max}\right) - C_2\right] + \cos\left[\omega\left(t - t_{\max}\right) - C_2\right]\right\} \tag{19}$$

In Fig. 4, the temporal courses of the average ground temperature throughout the year are shown. Also in this case, there is a major impact of the Biot number on the obtained calculation results. For Bi → ∞, the lowest ground temperature appears on the 14th of February and the highest – on the 16th of August. For Bi = 2 the average temperature reaches the extreme value 18–19 days later.

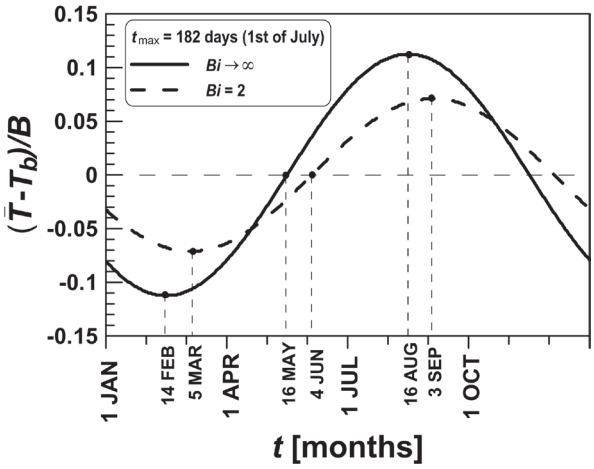

Fig. 4. Courses of average temperature of sub-surface of the ground

In the particular case of absence of the thermal resistance of heat transfer between the surface of the ground and the environment $h_0 \to \infty$ and Bi → ∞. Since then $C_1 = 1$ and $C_2 = 0$ and the above relationships simplify.

3. Mathematical model of a horizontal ground heat exchanger

If a heat exchanger is installed in the ground $q_v \neq 0$ and the heat conduction equation (1) with conditions (2), (5) and (6) should be solved numerically.

In the presented model, the flow through parallel arrangement of heat exchanger pipes is replaced by a flow through a horizontal cuboid channel of small thickness. The heat is transferred into (from) the ground symmetrically by both the lower and the upper surface of the heat exchanger.

In Fig. 5, the ground exchanger is shown as a fictitious cuboid, wherein, the heat is generated. Inside a cuboid of dimensions $L_g \times b \times \delta$, the temperature is equalized along the axis x and z at any time. The temperature variation along the y-axis is taken into account

by dividing the heat exchanger into stages. A working fluid flows in series through the neighboring stages, which are treated in the model as perfect-mixing tanks. One of these tanks is shown demonstratively (Fig. 5).

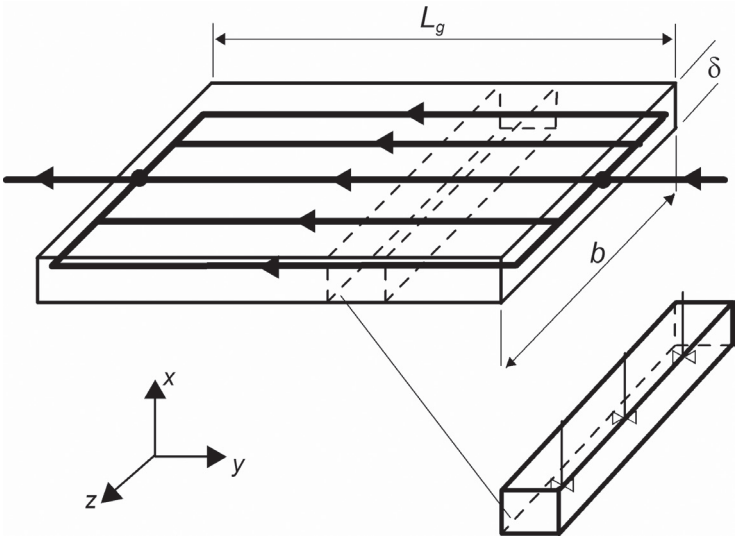

Fig. 5. Ground heat exchanger as a horizontal cuboid channel

In the case of ground heat exchangers, the thermal resistance occurs in working fluid and in walls of pipes but mainly in the ground. Individual resistances are related to areas through which the heat is transported. The presented model only includes the resistance to heat transfer in the ground. The consequence of this is that the surface of the pipes is not used in the model. For the modeled exchanger, it can be assumed that the heat transfer surface is a surface of the ground A_g where the exchanger pipes are installed. The quantity A_g should be treated as an adjustable parameter of the model that depends on the way of arrangement of pipes and the depth of their location under the ground surface.

In this model, the equation for an infinite plate, for which one surface is the surface of ground, and the other is located at a great depth providing the ground temperature stability is used. For transient conduction in an infinite plate with an internal heat source, the relationship (1) is valid; the quantity q_V is a rate of heat generation of the heat source per unit volume:

$$q_v = -\frac{\dot{Q}}{V} \tag{17}$$

where V is the volume of horizontal cuboid. $\dot{Q}$ is related to the transport of heat between the working fluid flowing through the ground heat exchanger and the ground. A detailed description of the model is shown in work [5].

4. Experimental verification of the model

In order to verify the presented mathematical model of the horizontal ground heat exchanger, the ground temperature profiles generated computationally in period of 53 days during the heating season, were compared with the measurement results presented by Wu et al. [6]. The cited authors researched the ground heat exchanger used as a lower heat source of a heat pump for space heating. Horizontal coils of exchanger pipes were arranged in four rows with a width of 1 m and a length of 80 m each, at a depth of 1.14 m. The exchanger operated continuously. Ground temperature was measured at seven depths in the range of 0 to 1.14 m. The measurements were conducted in close proximity to the heat exchanger pipes and, separately, away from any of the heat exchanger pipes (reference hole).

In model calculations it was assumed that the environment temperature periodically varied in time according to the relation:

$$T_a = T_b + B \cdot \cos\left[\omega\left(t - t_{\max,y}\right)\right] + B_d \cos\left[\frac{2\pi}{24}\left(t - t_{\max,d}\right)\right] \tag{18}$$

where B_d is half of the maximum daily temperature range. In the above formula, the second term applies to temperature variability in the annual cycle (y) and the third term – in the diurnal cycle (d).

The model course of the air temperature under measurements conditions (7th Nov– –28th Dec, around London) is presented in Fig. 6.

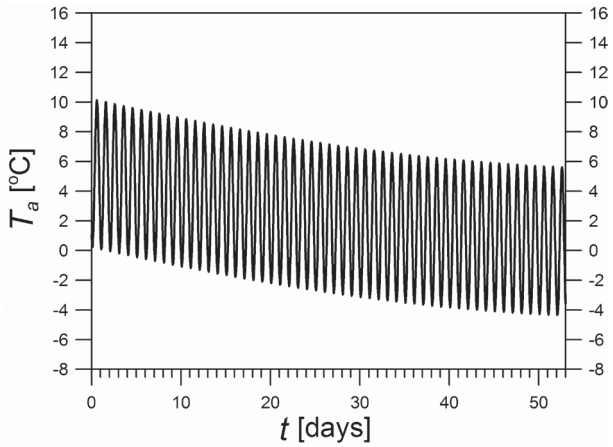

Fig. 6. The air temperature course (Eq. (18))

In the calculations based on the model, the following values of parameters were used: n = 300 (number of calculation nodes), time step Δt = 1 h. The data according to which the calculations were carried out are presented in Table 1.

Table 1

The process parameters used in calculations

Symbol	Value	Symbol	Value
$\dot{Q}$	4220 [W]	m	4
k	1.24 [W/(m·K)]	h_{inf}	20 [m]
c	1465 [J/(kg·K)]	h_0	20 [W/(m^2·K)]
ρ	1588 [kg/m^3]	B	9.0 [K]
$\dot{m}_L$	0.57 [kg/s]	B_d	5.0 [K]
c_L	3700 [J/(kg·K)]	$t_{\max}$	190 [days]
A_g	450 [m^2]	T_b	9.5 [°C]

The measurement results, together with the results of calculations according to the presented model, are depicted in Figs. 7a and b. The symbols represent the experimental values read out from the drawings shown in [6] referred to the 28th of December. Fig. 7a presents temperature profiles for the ground without a heat exchanger, while Fig. 7b refers to temperature profiles around the working heat exchanger in which the working fluid receives the heat from the ground. As one can see, the predictions based on the model are correct, although there are small difference in temperature determined experimentally and computationally.

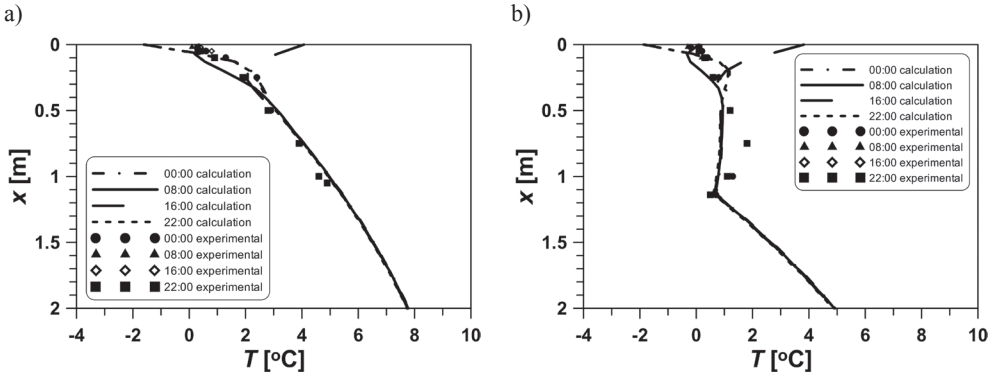

Fig. 7. Comparison of computational and experimental values: a – ground under natural conditions, b – working ground heat exchanger

It should be noted that the compatibility of temperature profiles in Fig. 7a and b depends mainly on the consistency of the actual air temperature in the research (and the preceding) period with the temperature used in the calculations. To generate the data for Fig. 7a, A_g = 450 m^2 was assumed.

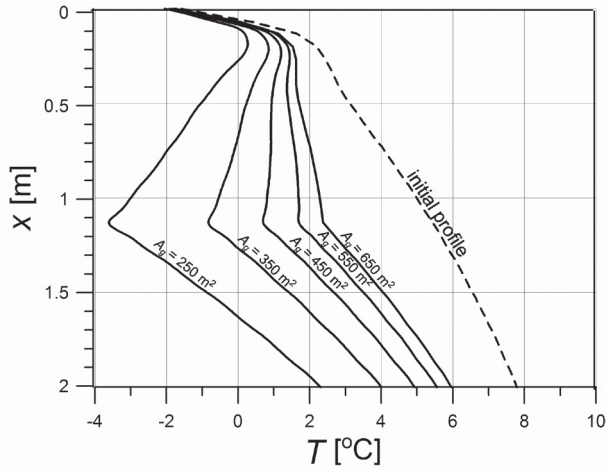

Fig. 8. The effect of the parameter A_g on temperature profiles in the ground

The effect of the adjustable parameter A_g on the temperature profiles in the ground is presented in Fig. 8. The calculations were performed on the basis on the data shown in Table 1. The greater value of A_g the lower the ground temperature drop with respect to initial temperature profile in the ground, determined according to relationship (8). The reason is that the greater value of A_g corresponds to the greater mass of cooled ground. Therefore, the relationship between A_g and the real value (geometric) of the ground area is significant. For a high-density embedded exchanger tubes, the value A_g is close to the geometrical ground area, wherein, the exchanger pipes are installed. For long times of the process duration the amount of A_g might exceed the geometric area (additional heat conduction in horizontal direction). However, the lower packing of tubes along with the shorter time of the heat receiving process from the ground, the more the values of A_g deviate (are smaller) from the geometric area.

For calculations presented in Fig. 7b, the value of A_g is assumed to be approx. 40% higher than the geometric area derived directly from the calculations of the area of trenches dug out for the installation of the heat exchanger pipes: $4 \cdot 1 \cdot 80 = 320$ m^2.

5. Conclusions

- The resistance of heat transfer between the surface of the ground and the environment (external thermal resistance of heat transfer) strongly affects the heat flux and the amount of heat, transferred between the ground and the environment as well as the temperature distribution of the sub-surface layer of ground. Reduction of this resistance is beneficial during receiving of heat by the ground exchangers;
- Heat transfer in a horizontal ground heat exchanger can be described by a model based on one-dimensional transient heat conduction equation with an internal heat source;

– The temperature profiles in the ground determined with the use of the presented mathematical model are consistent with the results of the measurements given in literature;
– The presented model can be used to analyze the effects of various process parameters on the ground heat exchanger efficiency.

References

[1] Demir H., Koyun A., Temir G., *Heat transfer of horizontal parallel pipe ground heat exchanger and experimental verification*, Applied Thermal Engineering, 29, 2009, 224233.
[2] Florides G., Kalogirou S., *Ground heat exchangers – A review of systems, models and applications*, Renewable Energy, 32, 2007, 2461–2478.
[3] Gan G., *Dynamic thermal modeling of horizontal ground-source heat pumps*, International Journal of Low-Carbon Technologies, 8, 2013, 95–105.
[4] Gonzalez R.G., Verhoef A., Vidale P.L., Main B., Gan G., Wu Y., *Interactions between the physical soil environment and a horizontal ground coupled heat pump for a domestic site in the UK*, Renewable Energy, 44, 2012, 141–153.
[5] Kupiec K., Larwa B., Gwadera M., *Heat transfer in horizontal ground heat exchangers*, Applied Thermal Engineering, 75, 2015, 270–276.
[6] Wu Y., Gan G., Verhoef A., Vidale P.L., Gonzalez R.G., *Experimental measurement and numerical simulation of horizontal-coupled slinky ground source heat exchangers*, Applied Thermal Engineering, 30, 2010, 2574–2583.
[7] Carslaw H.S., Jaeger J.C., *Conduction of Heat in Solids*, second ed., Clarendon Press, Oxford 1959, 65–74.

TECHNICAL TRANSACTIONS | CZASOPISMO TECHNICZNE
CHEMISTRY | CHEMIA
1-Ch/2015

HALINA MACHOWSKA*

POWER INDUSTRY – COAL ECOLOGY

ENERGETYKA – WĘGIEL-EKOLOGIA

Abstract

In this work, the fuel structure of electric energy production is presented, and also the coal-based power industry influence on the environment, greenhouse effect, mercury emissions from coal burned by power stations. EU requirements regarding limits of mercury emissions, as well as methods and techniques enabling reduction of mercury emissions originating from coal burning processes.

Keywords: coal, mercury content in coal, mercury emissions, power industry, ecology

Streszczenie

W pracy przedstawiono: strukturę paliwową wytwarzania energii elektrycznej, wpływ energetyki, bazującej na węglu na środowisko naturalne, efekt cieplarniany, emisję rtęci z energetycznego spalania węgla, wymogi Unii Europejskiej w zakresie ograniczenia emisji rtęci, metody i technologie pozwalające na obniżenie emisji rtęci z procesów spalania węgla.

Słowa kluczowe: węgiel, rtęć w węglu, emisja rtęci, energetyka, ekologia

DOI: 10.4467/2353737XCT.15.106.4054

* Ph.D. Eng. Halina Machowska, Institute of Chemistry and Organic Technology, Faculty of Chemical Engineering Technology, Cracow University of Technology.

1. Introduction

For the second half of the XXI century, one should expect serious changes in the structure of natural fuels consumption, resulting from their availability. Fossil fuel, especially coal, will dominate as a result of a constantly growing world demand for electrical energy. Coal is the only raw material ensuring fulfillment of energetic demands for about 200 years, as crude oil resources will be exhausted after about 45 years and natural gas resources after about 60 years. Currently, many EU countries are obtaining electrical energy from coal because of its local availability. Exhausting of natural resources of hydrocarbons could be significantly accelerated, taking into consideration a serious increase in demand for natural energy carriers, mainly in Asian countries, e.g. China and India. This is the main reason for the return to using the most diffused energetic raw material in the world – coal [1].

2. Coal Merkury Emission

Hard coal and brown coal are the warranty of Polish energetic safety.

The structure of electrical energy production in Poland is as follows: hard coal – 56%, brown coal – 36.9%, gas – 2.9%, renewable energy sources – 4.2%.

The structure of coal consumption in Poland is as follows: power industry – 54%, coking plants – 14.2%, heating engineering – 13.5%, food processing industry – 8.2, households 10.1% [2].

The increase in demand for final energy in Poland, till the year 2030, will amount for about 45%, and for primary energy of about 35%.

In Poland, professional electric power engineering is responsible for the emission of: CO_2 of about 45%, SO_2 – 55%, NO_x – 30%, dust 10% [3].

The production of 1 kWh of electric energy is accompanied by the release to the atmosphere of about 1000 grams of CO_2, 8÷12 grams of SO_2, 3÷4 grams of NO_x.

The fuel structure of 15.8 GW of electric energy production in Polish Energy Group (PGE) for 2020 year is as follows: brown coal – 56%, hard coal – 18%, gas – 15%, renewable energy sources (RES) – 11%; for year 2035 with 21.3 GW of energy: brown coal – 33%, hard coal – 5%, gas – 11%, RES – 14%, nuclear energy – 37% [4].

The main source of mercury emitted to the atmosphere as a result of human activities is burning of fossil energetic raw materials, and especially coal, responsible for 45% of total mercury emissions, further 18% is connected to gold extraction from rocks and gold-dust. Two-thirds of total global mercury emissions come from Asia, mainly from China. In China and India, the main mercury sources are coal burning power stations, however, in South Africa mercury emission sources are gold mines.

The condition of coal share increase as energetic and chemical raw material is the introduction of clean coal technologies. It requires greater cost and solution of difficult technical problems – removing, storing and utilization of CO_2 from off-gases and processes.

Poland, after entering the EU, was obliged to transform the Polish power industry in order to meet guidelines given by the Commission Communication for the Council and European Parliament – Union Mercury Strategy – Brussels 28-01-2005. One of the main sources of

mercury release is coal burning. Coal burning in power stations above 50 MW was defined in IPPC Directive (Integrated Pollution Prevention and Control), Council Directive 96/61/WE of 24-09-1996. IPPC Directive regarding integrated pollution prevention and control is the key instrument for mercury and other substances harmful to the environment.

Guidelines describing the best available technologies for individual industry branches contain so called *reference documents* (BREF – BAT – *Beat Available Technology*). For large burning sources, BREF defines that, taking into consideration the reduction of heavy metals share in flue gases from coal burning, the best control level can be achieved by the application of fabric filters (FF) and electrostatic precipitators (ESP) together with the processes of flue gases desulfurization (FGD). In order to reach further reduction in mercury emissions, it is recommended to practice mercury oxidation and adsorption on appropriate materials. An emissions level below 0.05 mg/m^3 is considered as one of the best for currently available technologies.

According to BAT, the reduction of the mercury emissions in the case of hard coal burning should amount to 70÷98%, and for brown coal 30÷70%. Lower admissible mercury emission reduction in the case of brown coal burning results from lower coal content in ashes formed during brown coal burning and higher mercury content in flue gases [5].

In Europe, mercury level in the air is below a value that influences human health, they are not in the Directive regulations regarding mercury.

Mercury is a natural coal component and occurs mainly with pyrite FeS_2, usually as a bivalent mercury forming complexes with humus substances or ferric sulfides [6]. Brown coal burning results in higher mercury emissions into the atmosphere than hard coal burning. During burning, the mineral substance undergoes profound physical and chemical transformations leading to slugs and fly-ashes. Mercury emitted to the atmosphere occurs as elementary mercury adsorbed on small dust particles and in a gaseous form. In the atmosphere, mercury can spread for very long distances (hundreds of kilometers).

The results of research works [6] show that mercury content in hard coals and brown coals exploited in Poland were in the range of several to several hundred ppb. Its average content in coal was: in Low Silesia deposits – 399 ppb, in Lublin deposits 105 ppb and in High Silesia deposits (the lowest mercury content) – 60 ppb.

Average mercury contents in brown coal were higher than mercury content in hard coal. Investigated brown coal deposits contained from a few dozen to over 1000 ppb, and its average content was 322 ppb and was several times higher than its content in hard coal. The highest average mercury content was found in brown coal from Bełchatów deposit – 416 ppb, and the lowest from Lubstów deposit – 199 ppb.

Mercury content in waste rocks, accompanying coal in deposits, was close to the mercury content in coal. The average mercury content in waste rocks found in investigated coal deposits was 129 ppb. Mercury content in waste rocks in brown coal deposits was lower than mercury content in coal samples. Average mercury content in investigated waste rocks accompanying brown coal deposits was 97 ppb – considerably lower than in coal, and also considerably lower than in waste rocks accompanying hard coal deposits.

Investigation of coals used in Polish power stations [7] showed that average mercury content in hard coal was in the range of 50 to 150 ppb, and in brown coal 120 to 370 ppb, which means that mercury quantity introduced with brown coal for burning in professional power stations is about three times greater than of that introduced with hard coal. During coal burning, mercury gathered mainly in fly-ashes, and some minor quantities in slug. When

burning hard coal, the mercury amount in fly-ash was in the range of 130 to 1000 ppb, and in slug 2 to 30 ppb. When burning brown coal, the mercury amount in fly-ash was in the range of 130 to 1400 ppb, and in slug 15 to 90 ppb. These different levels of mercury emissions are caused by different amounts of mercury in different coals, and moreover, greater share of ash in coal causes greater mercury content. Also, different emissions level may depend on the type of furnace used: pulverized-fuel boiler, fluidized, stoker fired, and also of equipping boiler with dust extraction plants: electro-filters, bag filters and desulfurization plants incorporated into flue-gases stream [7].

Mercury emitted as a result of coal burning has a form of metallic mercury Hg^0, oxidized mercury Hg^{+2} and mercury bounded to Hg ash. Both mercury forms Hg^0 and Hg^{+2} have different physical and chemical properties and for this reason they react differently in flue-gases and in the atmosphere. Such a behavior imposes selective treating of each form. Metallic mercury Hg^0 is a durable form, volatile, of low solubility in water and easily spreadable in the atmosphere for long distances. Oxidized mercury Hg^{+2} is a form soluble in water and quickly undergoes wet or dry deposition.

In technical literature, there is relatively little data regarding Hg^{+2} compounds. Generally, it is assumed that $HgCl_2$ dominates, however, it also could be HgO, $HgSO_4$.

Coal enrichment before burning process, especially removing of pyrite, dust removing and gas cleaning can considerably lower harmful substances emission, generated in the burning process, including mercury.

Values of heavy metal emission into the air, determined in Poland for year 2010 show that comparing with year 2009 emissions, took place an increase in global Poland mercury emissions of about 4.4%. This slight increase in mercury emissions was caused, first of all, by a greater consumption of hard coal and brown coal in burning and industrial processes. So, the share of the greatest sectors of Polish economy in mercury emissions in 2010 year, together with Selected Nomenclature for Air Pollution (SNAP) codes, classification of pollutants emission sources is as follows [8]:

SNAP code 01, 59.1% – burning processes in the sector of energy production and transformation;
SNAP code 02, 12.0% – burning processes outside industry;
SNAP code 03, 23.4% – burning processes in industry;
SNAP code 04, 5.3% – production processes;
SNAP code 09, 0.2% – waste management.

Comparison of total emissions for 2010 and 2009 years is as follows:
Hg 104.43% (2010 y. 14.846 metric tons and 2009 y. 14.216 metric tons).
Total Hg emissions 2010/2009 slightly increased to 104.43%.

As an example, emission values for SO_2 and NO_x are also presented:
SO_2 112.99% (2010 y. 973,586.864 metric tons and 2009 y. 861,682.310 metric tons);
NO_x 105.44% (2010 y. 866, 807.452 metric tons and 2009 y. 822,093.748 metric tons).

3. Climate and Energy package

On 23 January 2008, the European Commission presented a package of documents, so called the climate and energy package.

In Poland, problems with climate politics aroused in year 2008, when the European Commission started to push reduction goals, taking as a base the year 2005. Such an approach completely omits reductions introduced in Poland in the last decade of 20th century. Moreover EU forced tightening of climate politics in 2010 year, by introducing new emission accounting system in energy consuming industries, disadvantageous for coal, namely by rising emission prices on the permit market (so called *backloading*).

At present, the climate and energy package is also becoming problematic in other countries. Representatives of all energy-consuming industry branches (paper, glass, steel and chemical industries) think that climate politics is the main cause of high energy prices and a loss of competitiveness. In a time of depression, it is more and more important, but it seems that economic situation for changes could arise; for example, reduction of carbon dioxide emission in Germany was blocked, for new cars produced mainly in Germany [9].

Common European Union energy politics heads towards ensuring, for a long period, energetic safety and energy production abiding rules of sustainable development.

Basic trends of new energy politics are as follows:

– Up to year 2020, share of renewable energy should amount to 20% (average) and should be accompanied by a 20% decrease of carbon dioxide emission, as well as a 20% increase in average efficiency of electrical energy production in EU countries.
– Up to year 2030, production of electrical energy will be based on sources not generating carbon dioxide emissions, and power stations using coal will be forced to remove it and to sequestration.
– By 2050, only non-emitting power stations will be allowed to operate, using mainly hydrogen, renewable fuels and nuclear synthesis.

Eurostat (European Statistical Office) data show that, in 2011, carbon dioxide emissions in Germany *per capita* was higher than in Poland and amounted to 9.976 metric tons, in comparison with 8.573 metric tons in Poland. It was only slightly lower in Great Britain, and average value *per capita* in EU was 7.92 metric tons. In 2012, Germany emitted to the atmosphere 2% more carbon dioxide than in 2011, and in 2013, its emissions was still greater. In Poland, carbon dioxide emissions gradually decreasing.

In Poland, power engineering is based on coal and, for this reason Poland, is criticized, but on the other hand, coal consumption in Germany shows a rising tendency. Brown coal share in energy production in year 2012 rose in 2012 to over 25% in comparison with 22.7% two years earlier. Share of hard coal also rises and many new energy producing investments based on coal are underway. The greatest carbon dioxide emitters – China, United States of America and Russia, taking into account only their economic development, do not accept obligations regarding emissions reduction.

Imposed by EU reduction of carbon dioxide emissions, according to Polish Chamber of Commerce estimation could lead to the rise of electric energy prices in Poland by 35%, already in 2020 year, and to serious drop of Polish industry competitiveness [10].

4. Conclusions

The International Energy Agency claims that, in the oncoming decades, the world will not be able to satisfy its demand for energy without coal. Thanks to new technologies, coal will be more and more of an ecological energetic raw material.

EU climate and energy politics discriminate coal and have nothing against the use of crude oil, although, fuels produced from crude oil are responsible for nearly the same amount of carbon dioxide emissions (car off-gases constitute 65% of all the air pollutants in EU).

These fuels are burned in cars with very low effectiveness, because for the propulsion they use only 1% of energy contained in gasoline or diesel oil. In coal burning power stations, this index is at present between 35% and 45%, which is possible due to modernization of existing power units and the construction of new ones, and as a result of the introduction of new technologies, so called units of supercritical and extrasupercritical parameters.

The main task of recently introduced technologies called "clean coal technologies" and of new methods of energy production from coal is rising the effectiveness of coal power units and reduction of harmful to the environment carbon dioxide, dusts and gases emissions. These new methods and technologies include: pulverized fuel boilers, fluidized boilers, off-gases desulfurization and denitriding units, burning coal together with biomass, burning in an oxygen atmosphere or in the air with a higher oxygen content, coal gasification and underground coal gasification, nuclear-coal synergy, and finally, carbon dioxide capturing and storing with CCS (Carbon Capture and Storage) method. This method arises many doubts because it is unprofitable and markedly lowers energetic effectiveness of power units. Moreover, there is no certainty that carbon dioxide pumped under soil will not negatively influence the environment.

To the goals of climate-energy politics declared by European Commission till 2030 belong, among others, postulates of greenhouse gases emissions reduction by 40% and increase by 30% the use of Renewable Energy Sources – jointly, for all EU countries, and also an obligatory increase by 40% of the energetic effectiveness. Experts of the Polish Chamber of Commerce or Central Europe Energy Partners claim that the adoption of such rigorous goals of emissions reduction and increase of *green energy* share (this type of energy is at present three times more expensive than energy received from coal burning) will cause drastic increase of 1 MWh prices – even by 100%. Final result of such politics will be the relocation of plants to countries which did not adopt the emissions limits, like USA, where the price of gas is the basis for 60% of energy used in USA, it is five times lower [11]. The European Union is responsible for only 12% of global carbon dioxide emissions and the EU reduction plans, without similar decisions of other countries, will not contribute to climate improvement, and what's worse, it will cause the EU economy to be less competitive.

References

[1] Ściążko M., *Conditions of implementation of zero-emissions coal technologies in power engineering*, 2007, Zabrze, Ed. IChPW (Institute of Chemical Coal Processing).
[2] Szczepaniuk M., Dziennik Gazeta Prawna, 2013-07-29.
[3] Polityka Energetyczna Polski do 2013 r. (Polish Energy Politics till 2013).
[4] Szczepaniuk M., Dziennik Gazeta Prawna, 2013-05-09.
[5] Reference Document on BAT for the Large Combustion Plants, Seville-Spain, 2003.
[6] Bojakowska I., Sokołowska G., Bulletin of Polish Geological Institute, 2001, 394, 5–54.

[7] Wojnar K., Wisz J., Energetyka (Power Engineering), 2006, 4, 280–283.
[8] www.kobize.pl, Polish Centre of Emissions Balancing and Management, 2014.
[9] Szymański K., Rzeczpospolita (newspaper), 2013-07-16.
[10] Arendarski A., Rzeczpospolita (newspaper), 2013-11-19.
[11] Rzeczpospolita (newspaper), 2014-02-06.

TECHNICAL TRANSACTIONS | CZASOPISMO TECHNICZNE
CHEMISTRY | CHEMIA
1-Ch/2015

ELŻBIETA MALEWSKA, ALEKSANDER PROCIAK*

MODIFICATION OF EXPANDABLE POLYSTYRENE BEADS

MODYFIKACJA PEREŁEK EKSPANDOWANEGO POLISTYRENU

Abstract

This paper presents the effect of modification of expandable polystyrene beads (PSB) with an additional amount of physical blowing agent and the addition of ethylene wax on their properties. Three different sizes of PSB beads were analyzed. The bulk density and thermal properties – thermogravimetric and differential scanning calorimetry were evaluated.

Keywords: expandable polystyrene, bulk density, DSC, TG

Streszczenie

W artykule przedstawiono wpływ modyfikacji perełek ekspandowanego polistyrenu (PSB) za pomocą dodatkowej ilości poroforu fizycznego oraz dodatku wosku etylenowego na ich właściwości. Analizie gęstości nasypowej oraz właściwości termicznych – termograwimetrycznej oraz skaningowej kalorymetrii różnicowej poddano 3 różne wielkości perełek PSB.

Słowa kluczowe: polistyren ekspandowany, gęstość nasypowa, DSC, TG

DOI: 10.4467/2353737XCT.15.107.4055

* Ph.D. Eng. Elżbieta Malewska, Ph.D. D.Sc. Eng. Aleksander Prociak, prof. CUT, Department of Chemistry and Technology of Polymers, Faculty of Chemical Engineering and Technology, Cracow University of Technology.

1. Introduction

Polystyrene (PS) is one of the earliest discovered synthetic thermoplastics. It is obtained by free radical polymerization of styrene (Fig. 1) [12]. Polystyrene can be obtained by bulk, suspension, emulsion and solution polymerization.

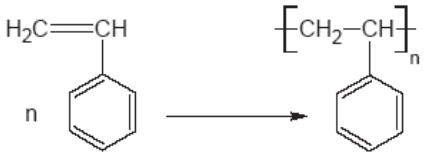

Fig. 1. Styrene polymerization reaction scheme

PS is a hard, brittle, transparent, easy-to-form material. In a commercial form, this material is known as a granulate, which is generally used for injection molding [12]. Additionally, the PS is one of the most commonly used plastics for the preparation of porous materials. In order to give it a cellular structure, foaming agents are used. Depending on the method of homogenizing of a polymer with blowing agent, there are two basic types of porous PS – expanded polystyrene (EPS) and extruded polystyrene (XPS).

Basic raw materials used for the preparation of a porous PS are monomeric styrene and blowing agents. Blowing agents suitable for the production of this material comprise of organic or inorganic substances, solid, liquid, or gaseous [8]. Currently, low-boiling, non-solvent polymer liquid having a high vapor pressure, such as isomers of pentane and hexane, are the most commonly used for the preparation of EPS. They are added in an amount of approx. 6% by mass. The use of liquid blowing agent is more effective than solid blowing agents because they can be uniformly distributed in the polymer. Through the use of low-boiling liquid, it is possible to obtain products with a low density and a uniform structure. However, the use of pentane isomers also has drawbacks. Pentane plasticizes the PS matrix, thus lowering its glass transition temperature [15]. The biggest disadvantage is its flammability and volatility. Therefore, in order to reduce the flammability of EPS, it is necessary to use flame retardants.

In literature of the subject, there is also a suggestion to replace pentane with water as an ecological blowing agent. EPS expanded by water (WEPS) can be prepared by a two-step suspension polymerization. The addition of 2–10 wt. % of water with a suitable surfactant is enclosed in the solid PS in the form of small droplets [6]. So far, WEPS has not been widely used and is not obtained on an industrial scale. It requires the use of special foaming conditions due to the small difference between the boiling point of water and the glass transition temperature of PS [11, 15].

A wider range of physical blowing agents is used in the preparation of extruded polystyrene. Generally, organic or inorganic inert gases are preferred [9]. The first blowing agents used for the preparation of XPS were chlorofluorocarbons (CFCs) and hydrochlorofluorocarbons (HCFCs) [4]. Later, they were replaced by new and more environmentally friendly blowing agents hydrofluorocarbons (HFCs) such as HFC-245 fa [16] or HFC-134a [5]. Carbon dioxide [9], and nitrogen [7] are also very often used.

1.1. The methods of EPS preparation

EPS is a porous material, which is obtained by foaming of PSB containing a blowing agent. The basic method of preparation of PSB is suspension polymerization conducted at elevated temperature and a pressure of approx. 1 MPa. As a result of this process, beads obtain a diameter of 0.3 to 5.0 mm [10].

Producers offer a large selection of PSB for expansion, which differ in size fraction, content and the type of blowing agent and flame retardants. These features of PSB determine their subsequent use (Table 1). The size of obtained granules can be controlled by varying the speed of agitation and the addition of an appropriate amount of suspension stabilizers [13].

Table 1

PSB application according to the size of beads [13]

PSB size [μm]	Size classification	Application
800–2000	Large	Insulation board
500–1000	Medium	Packaging, objects with complex shapes
300–800	Small	Containers with thin walls e.g. cups

PSB processing, in order to obtain final products, involves three-stages: the initial expansion, seasoning and final expansion coupled with the formation of finished products [3]. Pre-expansion can be carried out using hot air, hot water or steam [12] at a temperature of about 100°C. As a result, PS softens and the blowing agent closed inside beads evaporates giving a porous structure [14]. Pre-expanded polystyrene beads (P-EPS) are white, have regular shapes with dimensions up to several millimeters. During expansion, the bulk density of the beads is gradually decreased and after a period of about 5–10 min. reaches approx. 10–20 kg/m^3. The final formation of EPS products takes place in metal molds having perforated double walls. Through the holes in the walls steam is provided to the mold [14]. The steam makes further expanding of P-EPS possible, their sticking together and final forming in the mold shape.

Due to the cellular structure, EPS gains completely new, different properties, and therefore, new applications. The low cost of production and good properties of EPS allow this material to compete with polyurethane foams and mineral wool.

1.2. Properties and applications of EPS

EPS belongs to the group of rigid porous materials. PS foams are characterized by [8] application temperature range from –180°C to 75°C, resistance to fresh and salt water and moisture, resistance to acids, alkalis and alcohols, solubility in esters, ketones, ethers, aromatic hydrocarbons, resistance to microorganisms and lack of photostability – yellowing in the sun.

In Poland, EPS is the most commonly used heat insulating material. The share of EPS is up to 45–50% in the domestic market of thermal insulations [1]. EPS apparent density is in the range of 13–160 kg/m3. Due to the use of EPS as heat insulating material in the

construction, mechanical and insulating properties are also important, primarily compressive strength and thermal conductivity. Depending on the EPS apparent density, compressive strength has a value of 100–500 kPa, while thermal conductivity is in the range from 0.032 to 0.045 W/m·K [2]. Thanks to the easy formation even very complex shapes from EPS, all kinds of shock absorbers packaging, containers, trays or cups of different shapes and sizes are produced by the use of it.

The aim of this study was to obtain modified beads with better ability to be expanded than in the case of typical commercial PSB. Such beads may have other applications, e.g. for the preparation of polyurethane-polystyrene composites by co-expansion. Therefore, modification of PSB was performed by increasing the amount of pentane and polyethylene wax. Obtained beads were analyzed and bulk density as well as thermal properties were determined, and compared with the properties of commercial beads.

2. Materials

Owipian® FS is an expandable polystyrene, which is in the form of beads. It is produced by Synthos Sp.o.o. from Oświęcim. Owipian FS contains flame retardants (hexabromocyclododecane in an amount up to 0.5 wt.%) and a mixture of isomers of pentane as a blowing agent (6.0% by weight). Commercial beads were marked with the symbol S. Table 2 presents three EPS commercially available fractions and their characteristics.

Table 2

EPS commercially available fractions

	Fraction symbol		
	0513	0816	1325
Diameter of beads [mm]	0.7–1.0	1.0–1.6	1.6–2.4
Content of fraction [%]	≥ 95	≥ 95	≥ 95
Basic control sieves size [mm]	0.50–1.25	0.80–1.60	1.25–2.50

In this study, commercial PSB (type S) were compared with modified PSB. Modified beads were prepared according to the same formulation as commercial beads (detailed formulation is a company secret), but the concentration of certain ingredients in the formulation was increased. Firstly, PSB recipe was modified by increasing the amount of physical blowing agent. The content of pentane isomers was increased from 6.0 % to 7.5% by weight in the Owipian FS formula. These PSB were marked with the symbol P.

Another modification of PSB was saturating them (during the synthesis) substance capable to loosening of polymer chains cohesion. The synthesis was carried out on the basis of the Owipian FS recipe. The quantity of polyethylene wax increased by five times. These PSB were marked with the symbol W. Solid polyethylene wax has a molecular weight of 1000–2000 g/mol. Polyethylene wax is added to standard beads in order to improve their ability to foam. In addition, polyethylene wax is a nucleating agent substance.

All kinds of PSB (S, P and W) were divided into three fractions and marked with symbols: 0513, 0816, 1325.

3. Methods

3.1. EPS bulk density

The measurements of P-EPS bulk density were carried out according to PN-90/C-89298. This method involves placing a specified quantity of PSB in the heating medium under a given temperature for a specific period of time. Approx. 2.0 g PSB was thrown into water at temperature of 100°C. The beads were left in the water for 1, 2, 3, 5, 7 or 10 min. and then retrieved and dried at room temperature. Then the P-EPS were weighed and transferred into a measuring cylinder to determine the volume. A bulk density was calculated from the formula (1):

$$\rho_N = \frac{m}{V} \left[\frac{\text{kg}}{\text{m}^3} \right] \tag{1}$$

where:

ρ_N – bulk density [kg/m^3],
m – P-EPS mass [kg],
V – P-EPS volume [m^3].

3.2. EPS thermal properties

DSC analysis was performed using the analyzer MettlerDSC 823. Samples were heated at 10°C/min to a temperature of 300°C. The measurement was carried out under an inert atmosphere. The mass of the sample was approx. 5 mg.

Thermogravimetric analysis (TG) was done using a Netzsch TG209. The measurement was carried out in the air. The samples were heated at 10°C/min to a temperature of 600°C.

4. Results

This experiment shows that, with the increase of pre-expansion time, the bulk density of the P-EPS achieves smaller values. This relationship is observed for the 0513 and 0816 fractions. For the largest beads (1325), the bulk density reaches a minimum after expanding time of approx. 3 min. and then increases. PSB remaining at heating medium increase their volume until the break in the outer layer of the PS. After interruption of the layer, blowing agent escapes outside, the beads collapse, and the bulk density of P-EPS increases. It was also observed that then the larger initial size of the PSB then the lower bulk densities of P-EPS and the shorter time in which it is obtained.

It was also found that the modification of PSB affected their bulk density. Regardless of the fraction size the lowest bulk density was reached by the PSB containing an increased amount of pentane isomers (Fig. 2–4). In addition, minimum bulk density of PSB type P is achieved in shorter time than minimum bulk densities of commercial PSB and PSB type W. It was observed that the increased amount of blowing agent in the modified beads allows for a faster and more efficient expansion.

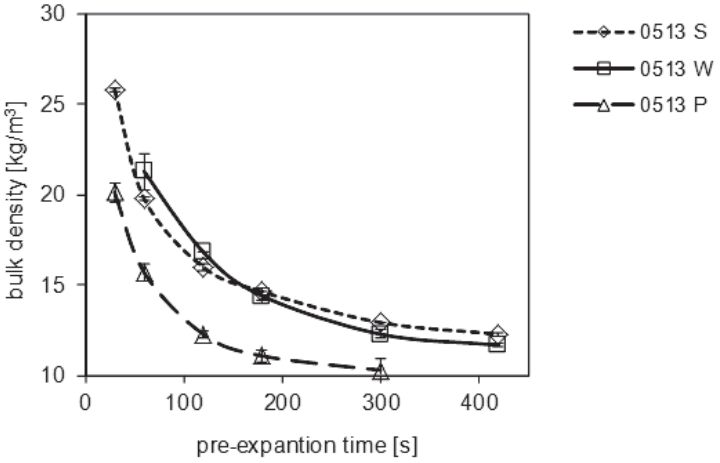

Fig. 2. Bulk density of commercial and modified PSB, fraction 0513 depending on the pre-expansion time

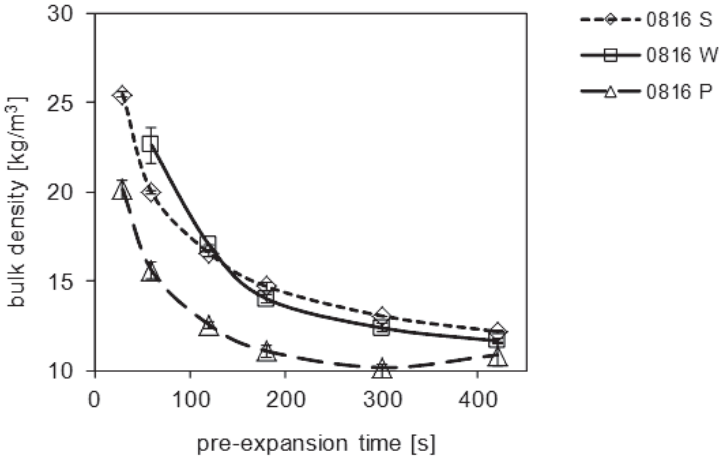

Fig. 3. Bulk density of commercial and modified PSB, fraction 0816 depending on the pre-expansion time

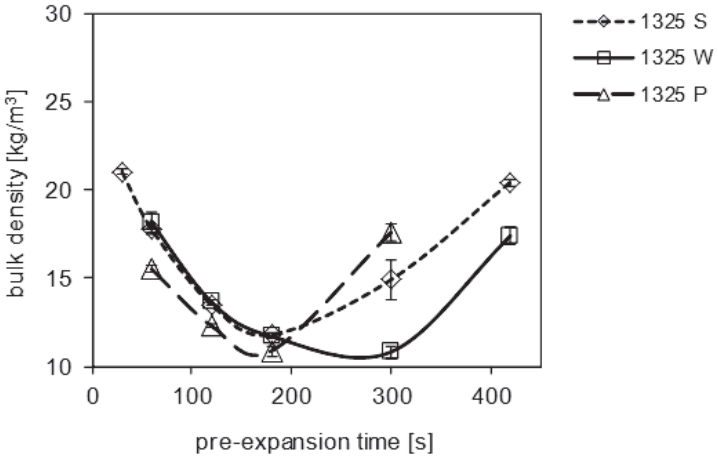

Fig. 4. Bulk density of commercial and modified PSB, fraction 1325 depending on the pre-expansion time

Commercial PSB (0513 and 0816 fractions) and PSB with the addition of polyethylene wax have similar expansion characteristic. In contrast, the expansion curve for fraction 1325 is characterized by a minimum after which the bulk density starts to rise again. Such behavior is observed regardless of the modification type. Commercial beads and beads modified with pentane have reached minimum bulk density after expanding time of approx. 3 min. On the other hand, PSB modified with polyethylene wax achieved minimum bulk density after the time of approx. 5 min. (Fig. 4). Accordingly, it was found that the addition of polyethylene wax in the case of the largest fraction makes it necessary to extend the time of pre-expansion, to achieve the minimum bulk density.

In order to know the phase transitions temperature of PSB, DSC analysis was performed. In all DSC thermograms, for the different fractions, as well as the types of PSB two peaks were observed. The example of the DSC thermogram for the PSB (fraction 1325) is shown in Fig. 5.

Phase transitions during expansion of PSB cause that on the thermogram are two endothermic peaks. The first peak starts at approx. 49°C, ends at approx. 63°C, and the peak falls at a temperature of approx. 54°C. The blowing agent that is enclosed within the PSB is a mixture of pentanes, with a boiling range of 40 to 60°C. Therefore, it was concluded that the first peak on the thermogram corresponds to the evaporation of physical blowing agent.

Despite the phase changes from liquid to gaseous, the blowing agent does not come out from the inside of the PSB. This is evidenced by TG analysis, which results are shown in Fig. 6. The beginning and the end of the weight loss was indicated by dotted lines. The beginning of this process was registered at a temperature of 64°C, while it is ended at 135°C. Upon heating, the sample lost approx. 6% of its weight. This is a value corresponding to the content of the blowing agent in the PSB. However, the loss of weight begins at a temperature higher than evaporation temperature of the blowing agent. This is due to the fact that the first blowing agent is trapped in the solid PS. After exceeding the softening temperature of the PS (about 75°C), the blowing agent may get out.

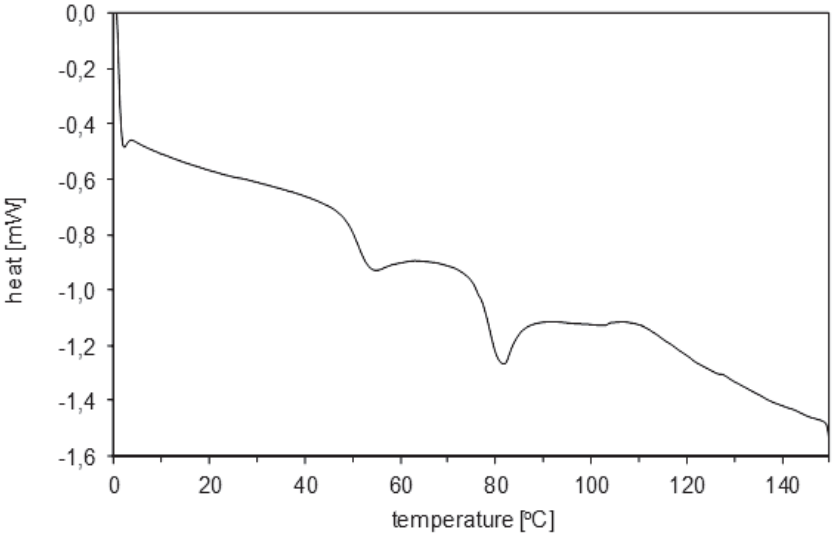

Fig. 5. The DSC thermogram of the PSB, fraction 1325

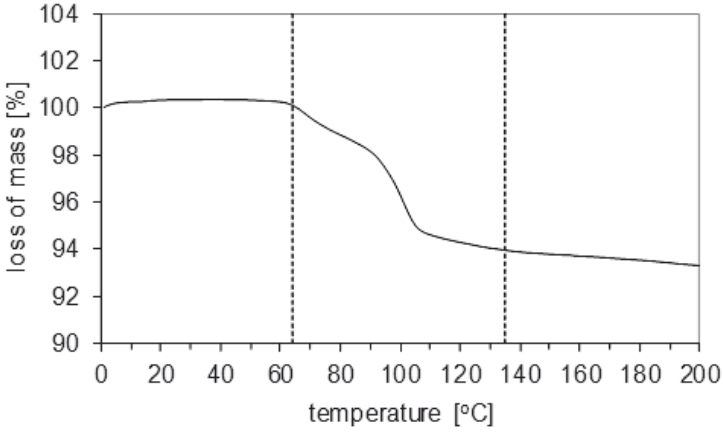

Fig. 6. Thermogravimetric curve of PSB, fraction 1325

The second peak in the DSC thermogram is observed at a temperature of approx. 80°C. The transformation starts at approx. 75°C and ends at approx. 86°C. In order to verify which changes are responsible for the presence of the second peak in the thermogram, DSC analysis was performed for P-EPS. P-EPS was cooled in liquid nitrogen, pressed and cut. In this way, P-EPS without blowing agent was analyzed. The result of the analysis is shown in Fig. 7. In a given DSC thermogram two endothermic peaks were not observed, as it was in the case of PSB with the blowing agent. However, there was a characteristic temperature collapse between 99 and 102°C. Such collapse occurs at the glass transition temperature, which for PS is equal to approx. 100°C.

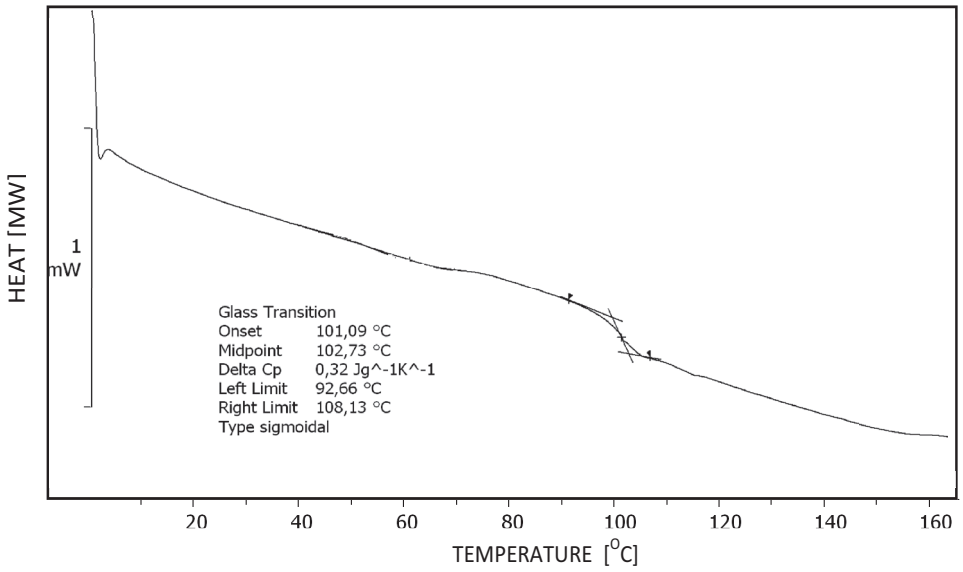

Fig. 7. DSC thermogram of free blowing agent P-EPS

Table 3

DSC analysis results for different fractions of modified and commercial PSB

Type of PSB	I onset temperature [°C]	I peak temperature [°C]	I end temperature [°C]	II onset temperature [°C]	II peak temperature [°C]	II end temperature [°C]
1325 S	49	54	63	76	80	86
0816 S	49	58	65	80	84	90
0513 S	51	62	69	82	86	92
1325 P	54	58	63	77	81	87
0816 P	54	58	63	78	82	88
0513 P	55	59	63	80	84	92
1325 W	55	60	67	80	84	90
0816 W	57	61	69	80	85	91
0513 W	60	66	71	85	90	97

It was found that the second peak appearing in the DSC thermogram of PSB is connected (like the first peak) to the presence of a blowing agent. The endothermic peak in DSC thermogram can be observed during desorption of various substances from different

polymers. Therefore, it is possible that second peak in the DSC curve is associated with the release of blowing agent from the PSB. Table 3 shows the results of DSC analysis of commercial and modified PSB.

The analysis shows that the larger the fraction of PSB is, the temperature of the second peak is lower. PSB of 1325 fraction is characterized by the lowest temperature change for all the examined beads, regardless of whether they are commercial or modified. Larger fractions of PSB can contain a higher amount of blowing agent that plasticized PS [6]. Therefore, the higher amount of pentane in large PSB fractions lowers their softening temperature. It was also observed that the fraction size of PSB does not significantly affect the evaporation temperature of blowing agent. The blowing agent within the beads, regardless of fraction size was the same in all fractions and, therefore, the phase transition temperature was the same.

PSB modification by the additional amount of pentane also reduced the temperatures at which the phase transitions occur in comparison with commercial PSB. This is also due to the presence of pentane plasticizing PS. On the other hand, the addition of polyethylene wax results in an increase of temperature at which phase changes occur.

5. Conclusions

The analyses show that the changes in the composition of polystyrene beads affects the selected properties of their pre-expanded forms. The bulk density of the pre-expanded beads, and the time at which a minimum value is reached depend on content of physical blowing agent and polyethylene wax.

Due to applied modifications, polystyrene beads were obtained, which may have new applications. The beads modified with the addition of more pentane have lower temperature of phase transformation, so that they are expanding more efficiently at lower temperatures than the commercial polystyrene beads. In contrast, the addition of polyethylene wax increases the permissible exposure time of beads at high temperatures, so that they do not collapse as quickly as commercially available beads.

References

[1] Anonym, *Rynek materiałów izolacyjnych w Polsce 2010, Prognozy rozwoju na lata 2010–2012*, PMR Publications, 2010.

[2] Anonym, *Styropianowe materiały izolacyjne w budownictwie – poradnik projektantów*, Stowarzyszenie Producentów Styropianu, 2005.

[3] Bering M.L., *Plasitcs Engeenering Handbook of the Society of the Plastics Industry*, Springer, 1991.

[4] Chau V., *Advences in thermal insulation of extruded polystyrene foams*, Blowing Agents and Foaming Processes 2011, Confrence Proceedings, 10–11.05.2011, Dusseldorf, Germany.

[5] Chau V., *Blowing agent emission from Styrofoam extruded polystyrene foams a simplified model to calculate the residual blowing agent*, Blowing Agent and Foaming Processes 2010, Confrence Proceedings, 19–20 maj 2010, Cologne.
[6] Crevecoeur J.J., Nelissen L., Lemstra P.J., Polimer, 1999, **40**, 3685.
[7] Faridi N., Dey S., Wan C., Xanthos M., *Use of Polyolefin Additiwes in Inert Gas Extrusion Foaming of Polystyrene*, ANTEC 2000 Plastics: The Magical Solution, Volume 2, Conference Proceedings, 7–11.05.2000, Orlando, USA.
[8] Hertz Z., Krajewski B., Penczek I., Płochocki A., Wiecheć T., Polistyren, Wydawnictwo Naukowo-Techniczne, Warszawa 1962.
[9] Kaemmerlen A., Asllanaj F., Jeandel G., Baillis D., Journal of Quantitative Spectroscopy & Radiative Transfer, 2010, **111**, 865.
[10] Maciaszek S., *Syntetyczne tworzywa porowate*, Wydawnictwo Naukowo-Techniczne, Warszawa 1963.
[11] Pallay J., Kelemen P., Berghmans H., Dommelen D., Macromol. Matter. Eng., 2000, **275**, 18.
[12] Pielichowski J., Puszyński A., *Technologia tworzyw sztucznych*, Wydawnictwo Naukowo-Techniczne, Warszawa, 2003.
[13] Shen J., Cao X., Lee L.J., Polymer, 2006, **47**, 6303.
[14] Sikora R., *Przetwórstwo tworzyw wiekocząsteczkowych*, Wydawnictwo Edukacyjne Zofii Dobkowskiej, Warszawa 1993.
[15] Snijders E.A., *Water expandable polystyrene (WEPS): computational and experimental analysis of bubble growth*, Technische Universiteit Eindhoven, Eindhoven 2003.
[16] Vachon C., *Foaming polystyrene with HFC-245fa and blend sof hfc-245fa and* CO_2, ANTEC Plastics: Annual Technical Conference, Volume 2, Conference Proceedings, 1–5.05.2005, Boston, USA.

TECHNICAL TRANSACTIONS | CZASOPISMO TECHNICZNE
CHEMISTRY | CHEMIA
1-Ch/2015

KLAUDIA PLUTA, DAGMARA MALINA, AGNIESZKA SOBCZAK-KUPIEC*

SCAFFOLDS FOR TISSUE ENGINEERING

RUSZTOWANIA KOSTNE DLA INŻYNIERII TKANKOWEJ

Abstract

The paper presents the current trends in medicine of regenerative tissue defect caused by resection of tumors or fractures. Although it is a relatively young field of science, it creates new possibilities for the reconstruction of pathologically altered tissue with the use of three-dimensional scaffolds. Tissue engineering places particular emphasis on the type of scaffold from which they are made because of a number of requirements of medical materials including biocompatibility, mechanical strength and porosity.

Keywords: scaffolds, tissue engineering, biomaterials

Streszczenie

Artykuł przedstawia trendy panujące w medycynie w regeneracji ubytków tkankowych powstałych na skutek resekcji nowotworów bądź złamań, skupione na wykorzystaniu inżynierii tkankowej. Ta stosunkowo młoda dziedzina nauki stwarza nowe możliwości odbudowy patologicznie zmienionych tkanek z wykorzystaniem trójwymiarowych rusztowań – skafoldów. Inżynieria tkankowa kładzie szczególny nacisk na rodzaj materiału, z jakiego produkowane są skafoldy, gdyż musi on spełniać szereg wymagań, m.in. biozgodność, wytrzymałość mechaniczna i porowatość.

Słowa kluczowe: skafoldy, rusztowania kostne, inżynieria tkankowa, biomateriały

DOI: 10.4467/2353737XCT.15.108.4056

* M.Sc. Eng. Klaudia Pluta, Ph.D. Eng. Dagmara Malina, Assoc. Prof. Ph.D. Agnieszka Sobczak-Kupiec, Institute of Inorganic Chemistry and Technology, Faculty of Chemical Engineering and Technology, Cracow University of Technology.

1. Introduction

The definition of tissue engineering was delineated in 1993 by Robert Langer and Joseph Vacanti. They identified it as an interdisciplinary field that combines various aspects of biology, materials science, engineering, and medicine [4, 17]. The main goal of this discipline is to develop biological substitutes that restore, maintain, or improve tissue function or a whole damaged organ [7].

Formerly, it was thought that damaged tissues should be replaced only by allogenic transplantation or artificial implants. However, these methods are not able to intercept all functions of lost tissue or organ. Concerned about the health of the patient, scientist began research on innovative biohybrid implants, which could be a temporary biological substitute for the loss of bone tissues. They are based on a combination of three-dimensional scaffolds made of a biocompatible material and cells cultures grown in the laboratory sterile conditions. The main aim was to get the information about the chemical, physical and mechanical properties of biomaterials and choose the material with specific, functional properties that favor the reconstruction of damaged tissues. It was also necessary to know the phenomena associated with the proliferation and differentiation of cells in their natural environment and under laboratory conditions [5, 19].

It is predicted that development in tissue engineering can eliminate the problems related to organ transplantations, such as rejection or lack of suitable donors. It also eliminates the use of materials with a relatively low biocompatibility, and therefore, a decrease in post-operative complications is observed [5].

2. Tissue engineering

The first achievement of tissue engineering is based on the generation of skin substitutes for burned patients. Over the past 20 years, the tissue engineering field has allowed the development and testing of artificial cartilage, bone, blood vessels, pancreas, heart valves, breast, nerves, trachea, bowel, kidney, lung and liver. Much of the research focuses on understanding and utilizing the potential of cells and improving materials to control cell behavior [13, 19].

The basic steps of tissue engineering are illustrated in Fig. 1. The first step involves the seeding of donor cells and growth factors on 3D scaffold which provides a framework and initial support for the cells to adhere proliferate and differentiate. To induce the growth of new, healthy tissue matrix is cultured in *in vitro* conditions in bioreactor. The final stage includes the implantation into the patient. It is desirable for scaffold to be a biodegradable because, after fulfilling, newly growing tissues can intercept its function [19, 25, 27].

Many different types of cells can be use in tissue engineering. The choice of cells is determined by their availability and the ability to multiply. The most attention is focused around stem cells which have the remarkable potential to differentiate into specialized cells. After division, every new cell can remain as a stem cell or become another type of cell like a muscle cell, a red blood cell, or a brain cell [15].

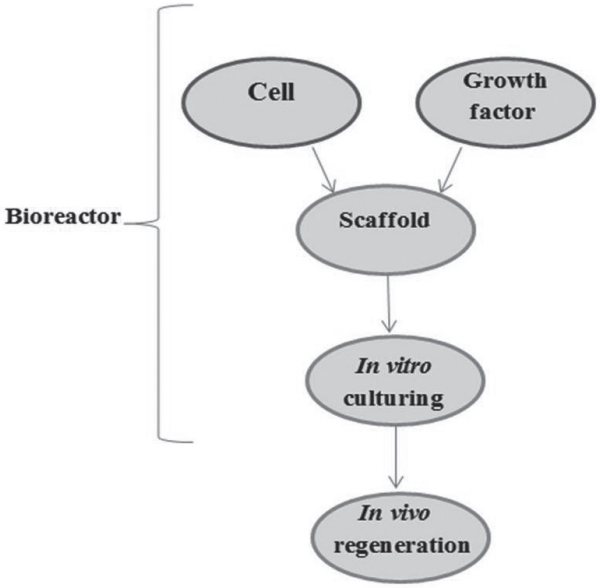

Fig. 1. Basic steps in tissue engineering [19]

Due to the potential for differentiation, there are the following types of stem cells:

- totipotential – cells that can differentiate into any cell type and give rise to whole organism,
- pluripotential – they can differentiate into any cell type, except germ cells,
- multipotential – somatic (adult) cells that are capable of replenishment new cells, often with similar properties,
- unipotential – progenitor cells, their differentiation is restricted for the manufacture of only one type of cell.

Mesenchymal stem cells – MSC isolated from the bone marrow are promising material used for the regeneration of damaged tissues. These multipotential cells have unique properties which make able to differentiate into specialized cells to form other tissues and organs and release substances that stimulate the surrounding cells to regeneration. MSC have also potential to *in vitro* into osteoblasts and chondrocytes, therefore, they can be used to reconstruction of damaged cartilage, bones, ligaments and tendons. Cells are seeded into artificial structure which provides supporting 3D tissue formation. Scaffolds should make cell attachment and migration possible, allow diffusion of vital cell and deliver and retain cells and biochemical factors [29].

3. Scaffolds

The key role of scaffolds is to provide temporary mechanical integrity at the defect site until the damaged tissue is repaired or regenerated, and normal biomechanical function is restored. Therefore, to fulfil the function, scaffolds should meet some specific requirements [8, 21].

At first, scaffolds must provide appropriate conditions to promote cell viability, proliferation and differentiation. A sufficiently high porous architecture of scaffold and an adequate pore size are necessary to facilitate cells seeding and diffusion throughout the whole structure of both dividing cells and nutrients. A large surface area is desirable for cell adhesion, therefore, the volume of the pores should be relatively high (50–90%) [20, 21].

Scaffold should be characterized by a high open porosity in which the pores are connected with each other and with the surface of the material. Interconnected porous structure of scaffold is required for cell penetration, tissue ingrowth, nutrient and waste transport. The presence of isolated pores prevents the diffusion of gases and fluids between cells. Most research shows that the best bone tissue ingrowth occurs in materials with a pore size of 100–500 μm, however, the high porosity and pore size affects the strength scaffold parameters. Therefore, it is necessary to evaluate the optimal value of the mentioned properties [21, 30].

Biodegradability and biocompatibility are important features for tissue engineering. The ideal scaffold made from a suitable biomaterial should be absorbed by the surrounding tissues without the necessity of a surgical removal and minimal degree of immune and inflammatory. It is important that the rate of degradation must be coincided as much as possible with the rate of tissue formation. That means that while cells fabricates their own natural matrix structure around themselves, the scaffold is able to provide structural integrity within the body and eventually break down leaving the neotissue, newly formed tissue which will take over the mechanical load [22, 23].

To provide tight integration with surrounding tissue, scaffold should be characterized by high bioactivity which is responsible for chemical bond formation. Osteoconductivity is another desirable scaffold property which support the regeneration process of damaged bones by assisting cells to adhere to the graft surface and to proliferate [28].

Scaffold should have mechanical properties compatible with the anatomical location and it must be strong enough to allow surgical handling during implantation. Production of scaffolds with appropriate mechanical and physical properties is one of the biggest challenges in tissue engineering [20].

4. Biocomposites applied for tissue engineering

Many types of biomaterials can be used to generation of 3D scaffolds for tissue engineering. Requirements for these materials are non-antigenic, non-carcinogenic, non-toxic, non-mutagenic actions and high cell biocompatibility. Such properties significantly affect to the quality of scaffolds like cell survival, growth, propagation and reorganization. Fig. 2. presents general groups and examples of biomaterials such bioceramics, polymeric materials and composites. Typically, ceramics, synthetic and natural polymers are used in the fabrication of scaffolds for tissue engineering. Each of these materials has specific advantages and disadvantages, consequently, the use of composite scaffolds is becoming increasingly common [18, 24].

In tissue engineering, composite materials are increasingly being used, about 30% of currently applicable biomaterials are composites. Interest in composites results from the biomimetic approach, which tries to understand and mimic the structure and mechanisms of natural tissue [1, 6, 31]. In tissue engineering, the most commonly used type of composite is

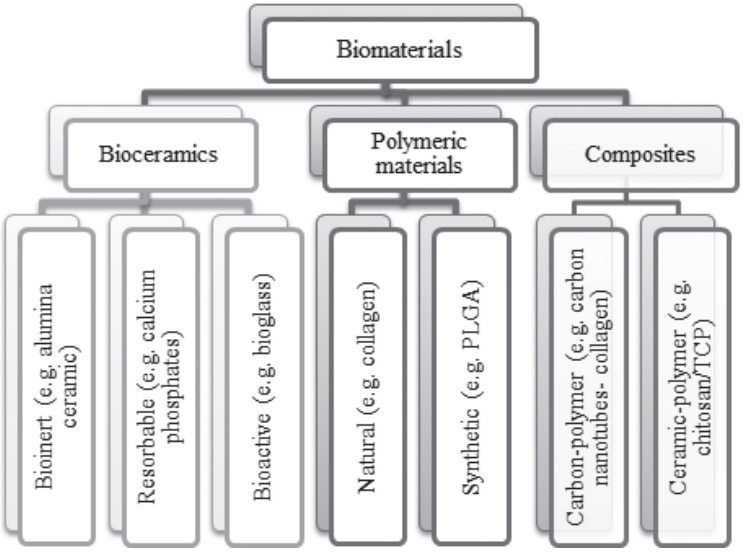

Fig. 2. The general group of biomaterials

combination of polymers with ceramics. Scaffolds made only from polymers have insufficient mechanical properties, mainly mechanical strength, Young's modulus and toughness. Another problem is low bioactivity of the polymer scaffolds, however, it can be eliminated by the addition of ceramic material, like hydroxyapatite or tricalcium phosphate. The connection of flexible polymer with active ceramic supports the regeneration of tissues [2, 6, 14, 32].

An exemplary material for scaffold production is a composite consisting of biodegradable polyurethane matrix and calcium carbonate (calcite). Preparation of three-dimensional scaffold is based on a combination of polymer coagulation technique with eluting of particles. In this method, the polymer solutions in 20% of 1-methyl-2-pyrrolidone and calcium chloride as porogenic particles are used in experiment. The obtained composite was cooled in liquid nitrogen, ground, dissolved and mixed with NaCl particles size of 300–420 microns (ratio PUR/NaCl – 1:1). Next, the material was poured into forms immersed in distilled water and left to maturate for the next 24 h. During the process, the polymer precipitation and eluting of porogen particle were observed. The final stage of scaffold preparation was dried at 37°C under vacuum for 24 h. Fig. 3. presents obtained scaffolds [10–12].

The resultant three-dimensional matrices exhibits improved properties compared with scaffolds made of pure PUR allowing the transport of gases, proliferation and cell differentiation. The research on PUR/calcite composites demonstrate that they fulfill the requirements for tissue engineering applications in bone defects repair [10–12].

It is also worth mentioning about research into the production of scaffolds based on chitosan and calcium – phosphate ceramics. They mainly focus on several preparation methods, i.e. rapid prototyping, freeze-drying, microgranules agglomeration and foaming. Using these methods, it is possible to construct spatial scaffolds with diversified structure, properties and thus different application. Fig. 4. shows chitosan/TCP composites prepared by varied techniques.

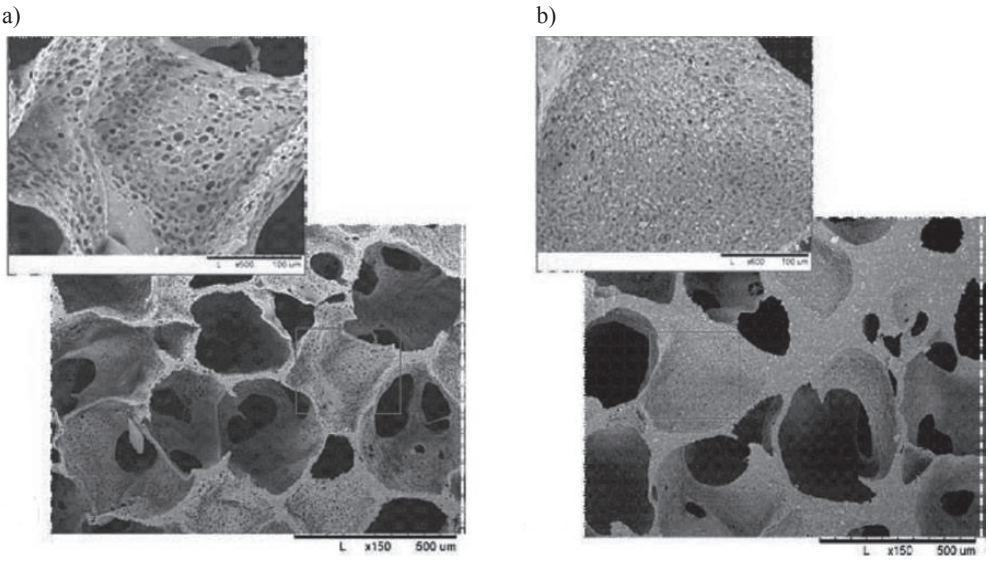

Fig. 3. The structure of scaffolds: (a): PUR + 20% calcite; (b): PUR + 40% calcite [11]

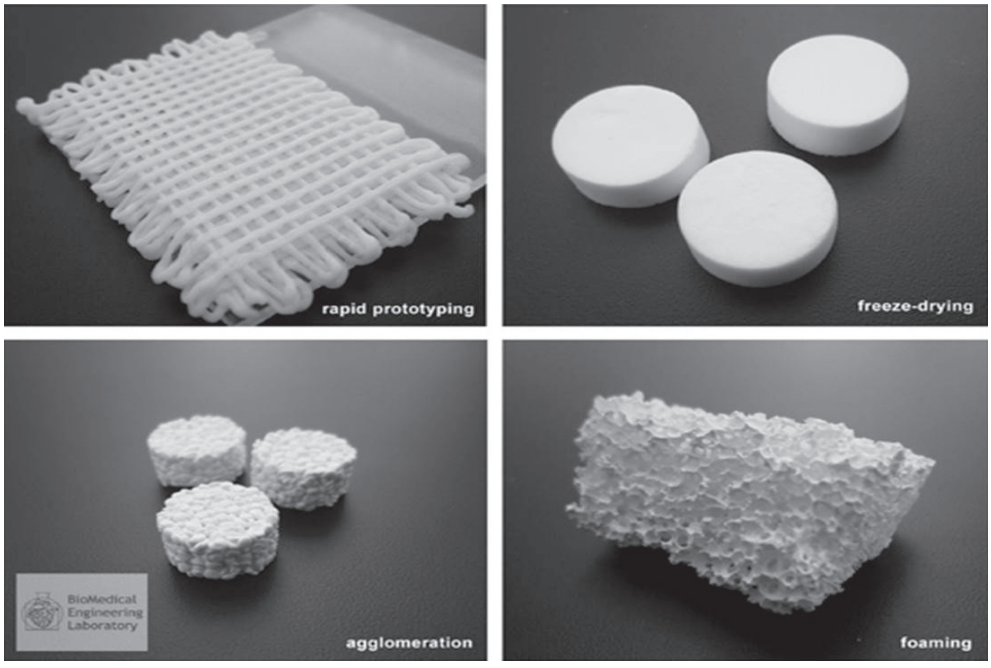

Fig. 4. Chitosan/TCP scaffolds prepared using varied techniques [33]

For example, production of scaffold by foaming method involves adding an acidic solution of chitosan to the TCP powder with particle size ranging between 3–5 μm. The quantity of introduced TCP determines the type of the results matrix structure. The formulation is mixed until a homogenous phase and then a foaming agent – $NaHCO_3$ is added. The resulting porous material was lyophilized, and after drying, washed with distilled water. The tests carried out on the obtained sponges exhibit the porosity at nearly 90%. This is possible due to gas production according to following reaction:

$$CH_3COOH + NaHCO_3 \rightarrow CH_3COONa + CO_2 + H_2O \quad (1)$$

In addition, the concentration of TCP added to the polymer affects the size of pores produced and degradation time. A low content of TCP makes distribution and pore size is irregular, but with increasing concentration of the ceramic phase, architecture of material is better organized. Moreover, the weight loss of composites with lower content of TCP (15%) is much greater than for the material with 50% of TCP [16].

An interesting group of composites, increasingly used in tissue engineering, are hydrogels. Due to its hydrophilicity, they have the ability to retain a large amount of water in its structure, without dissolution of the polymer. More important advantages of these materials are high biocompatibility, low friction coefficient, softness and plasticity, which imitate them to the natural structure of the soft tissue. In addition, hydrogels allow for the free flow of oxygen and nutrients, and therefore can be used as a scaffold [3, 9, 16]. For the preparation of hydrogels, researchers applied natural and synthetic compounds, i.e. poly (ethylene oxide), polyacrylic acid, poly (vinyl alcohol), chitosan, collagen or hydroxyapatite. One of many examples may be a hydrogel composite based on polyacrylic acid (PAA), polyethylene glycol (PEG), and HAp obtained in a few minutes [9, 26]. These type of materials are also used successfully for the production of hydrogel wound dressings or matrix for drug delivery [9].

5. Conclusions

Tissue engineering based on biology, materials engineering and medical knowledge strives to create an alternative method for the regeneration of damaged body tissues. By modifying the chemical composition of implant materials, engineers try to change and improve the functional properties of implants. Due to the fact that the architecture of scaffold plays an important role in its physicochemical characteristic, researchers develop innovative methods for the production of them. These methods ensure the obtaining matrices with desired mechanical or structural properties.

Composite materials appear to be promising biomaterial used for the production of three-dimensional matrices. A combination of at least two different properly selected phases improves properties of resulting material compared with the characteristics of the each component. Scaffolds made of polymer-ceramic materials simulated bone tissue ensure an adequate immune response, good strength, and the active bioceramic ingredient preferably affects a connection of matrix with the surrounding tissue. A major problem

faced by engineers is the time of scaffold resorption - modification of the implanted material when the material is located in the body can be changed, which may differently affect the human body.

This work was financially supported by The National Centre for Research and Development (Grant No. LIDER/037/481/L-5/13/NCBR/2014).

References

[1] Arafat M.T., Lam C.X.F., Ekaputra A.K., Wong S.Y., Li X., Gibson I., *Biomimetic composite coating on rapid prototyped scaffolds for bone tissue engineering*, Acta Biomaterialia, 7, 2011, 809–820.

[2] Bieniaś J., *Struktura i właściwości materiałów kompozytowych*, Politechnika Lubelska, Katedra Inżynierii Materiałowej, Lublin 2002.

[3] Butcher A.L., Offeddu G.S., Oyen M.L., *Nanofibrous hydrogel composites as mechanically robust tissue engineering scaffolds*, Trends in Biotechnology, 32, 2014, 564570.

[4] Chapekar M.S., *Tissue Engineering: Challenges and Opportunities*, Journal of Biomedical Materials Research Part B: Applied Biomaterials, 53, 2000, 617–620.

[5] Chen G., Ushida T., Tateishi T., *Scaffold Design for Tissue Engineering*, Macromolecular Bioscience, 6, 2002, 67–77.

[6] Chłopek J., *Biomateriały kompozytowe*, Kompozyty, 9, 2009, 3–18.

[7] Cui Z.F., *Tissue Engineering*, Department of Engineering Science, University of Oxford, United Kingdom 2004.

[8] Dias M.R., Guedes J.M., *Optimalization of scaffold design for bone tissue engineering: A computational and experimental study*, Medical Engineering & Physics, 36, 2014, 448–457.

[9] Drury J.L., Mooney D.J., *Hydrogels for tissue engineering: scaffold design variables and applications*, Biomaterials 24, 2003, 4337–4351.

[10] Dulińska-Molak I., Ryszkowska J., *Kompozyty PUR/CaCO3 do zastosowań jako podłoża do hodowli tkanek kostnych*, Czasopismo Techniczne, Mechanika, 1-M, 2009, 81–85.

[11] Dulińska-Molak I., Ryszkowska J., Kurzydłowski K., *Biozgodne kompozyty poliuretanowe z kalcytem do zastosowania w inżynierii tkankowej*, Przemysł Chemiczny, 89, 2010, 1614–1620.

[12] Dulińska-Molak I., Ryszkowska J., *Poliuretanowe pianki kompozytowe z kalcytem przeznaczone do hodowli tkanek kostnych*, Kompozyty 9, 2009, 228-233.

[13] Horch R.E., *New Developments and Trends in Tissue Engineering: An Update*, Journal of Tissue Science & Engineering, 3, 2012, e110.

[14] Hu X., Shen H., Yang F., Liang X., Wang S., Wu D., *Modified composite microspheres of hydroxyapatite andpoly(lactide-co-glycolide) as an injectable scaffold*, Applied Surface Science, 292, 2014, 764772.

[15] Kaźnica A., Joachimiak R., Drewa T., Rawo T., Deszczyński J., *Nowe trendy w inżynierii tkankowej*, Artroskopia i Chirurgia Stawów, 3, 2007, 11–16.

[16] Kucharska M., Butruk B., Walenko K., Brynk T., Ciach T., *Fabrication of in-situ foamed chitosan/b-TCP scaffolds for bone tissue engineering application*, Materials Letters 85, 2012, 124–127.
[17] Langer R., *Tissue Engineering*, Molecular Therapy, 1, 2000, 12–15.
[18] Leong K.F., Cheah C.M., *Solid freeform fabrication of three-dimensional scaffolds for engineering replacement tissues and organ*, Biomaterials, 24, 2003, 2363–2378.
[19] Liu C., Xia Z., Czernuszka J.T., *Design and development of three-dimensional scaffolds for tissue engineering*, Chemical Engineering Research and Design, 85, 2007, 1051–1064.
[20] O'Brien F.J., *Biomaterials & scaffolds for tissue engineering*, Materials Today, 14, 2011, 88–95.
[21] Pamuła E., *Biomateriały dla inżynierii tkankowej: badania nad kształtowaniem struktury i właściwości biologicznych poliestrów alifatycznych*, Wydawnictwo Naukowe „Akapit", Kraków 2008.
[22] Patel H., Bonde M., Srinivasan G., *Biodegradable polymer scaffold for tissue engineering*, Trends in Biomaterials & Artificial Organs, 25, 2011, 20–29.
[23] Patnaik A.K., Menzemer C., Srivatsan T.S., *On the Use of Titanium Alloys for Aerospace and Non-Aerospace Applications*, 17th International Symposium on Processing and Fabrication of Advanced Materials XVII, Eds. N. Bhatnagar and T.S. Srivatsan, 2008, 3–22.
[24] Sachlos E., Czernuszka J.T., *Making tissue engineering scaffolds work. Review on the application of solid freeform fabrication. Technology to the production of tissue engineering scaffolds*, Europeans Cells and Materials, 5, 2013, 29–40.
[25] Sengupta D., Waldman S.D., Li S., *From in vitro to in situ Tissue Engineering*, Annals of Biomedical Engineering, 42, 2014, 1537–1545.
[26] Sobczak-Kupiec A., Piątkowski M., Bogdał D., Wzorek Z., Tyliszczak B., *Synthesis of biomimetic HAp-PAA/PEG hydrogel composites*, Czasopismo Techniczne, 1-Ch/2011, 157161.
[27] Vacanti J.,*Tissue engineering and regenerative medicine: from first principles to state of the art*, Journal of Pedriatic Surgery Lecture, 45, 2010, 291–294.
[28] Wagoner Johanson A.J., Herschler B.A., *A review of the mechanical behavior of CaP and CaP/polymer composites for applications in bone replacement and repair*, Acta Biomateriala 7, 2011, 16–30.
[29] Wojno K., Kocki J., *Mezenchymalne komórki macierzyste w medycynie regeneracyjnej*, Samodzielna Pracownia Genetyki Klinicznej UM w Lublinie, http://www.rsi2004.lubelskie.pl/doc/sty5/art/Wojno_K_art.pdf, dostęp: 06.11.2014.
[30] Wu X., Yeung K.W.K., *Biomimetic porous scaffolds for bone tissue engineering*, Materials Science and Engineering, R, 80, 2014, 1–36.
[31] Wua S., Liu X., Yeung K.W.K., Liu C., Yang X., *Biomimetic porous scaffolds for bone tissue engineering*, Materials Science and Engineering R, 80, 2014, 1–36.
[32] Zhou C.C., Ye X.J., Fan Y.J., Qing F.Z., Chen H.J., Zhang X.D., *Synthesis and characterization of CaP/Col composite scaffolds for load-bearing bone tissue engineering*, Composites: Part B, 62, 2014, 242248.
[33] http://www.biomedlab.ichip.pw.edu.pl/content/view/14/8/lang,polish, dostęp: 06.11.2014.

TECHNICAL TRANSACTIONS | CZASOPISMO TECHNICZNE
CHEMISTRY | CHEMIA
1-Ch/2015

RYSZARD WÓJTOWICZ*, ANDREY A. LIPIN**

THE COMPUTATIONAL-FLUID-DYNAMICS STUDY OF AN UNBAFFLED STIRRED VESSEL WITH ECCENTRICALLY POSITIONED IMPELLER

SYMULACJE CFD MIESZALNIKA BEZ PRZEGRÓD Z NIECENTRYCZNIE SYTUOWANYM MIESZADŁEM

Abstract

The paper presents the results of *CFD* simulations of liquid flow in an unbaffled stirred vessel with an eccentrically positioned impeller. The influence of the impeller's distance from the tank axis (eccentricity) on the generated flow circulation was analyzed. Based on numerical modelling, the flow pattern, vortex formation as well as turbulence parameters in selected stirred vessel zones were determined. Obtained results were presented as vector/contour maps, and iso-surfaces of *Q*-criterion for identification of vortex cores. Additionally, for each investigated stirred vessel power consumption was calculated.

Keywords: mixing, stirred vessel, liquid flow, CFD simulations, impeller eccentricity

Streszczenie

W pracy przedstawiono wyniki symulacji *CFD* ruchu cieczy w mieszalniku mechanicznym bez przegród z niecentrycznie usytuowanym mieszadłem. Analizowano wpływ zmian odległości mieszadła od osi aparatu (niecentryczności) na generowaną w mieszalniku cyrkulację. Na podstawie modelowania numerycznego wyznaczono model przepływu cieczy, strefy tworzenia się wirów oraz parametry turbulencji w wybranych obszarach mieszalnika. Uzyskane wyniki przedstawiono w postaci wektorowych i konturowych map rozkładu, do identyfikacji położenia rdzeni wirów wykorzystano powierzchnie stałych wartości *Q*-kryterium. Dodatkowo w każdym z badanych mieszalników wyznaczono zapotrzebowanie mocy.

Słowa kluczowe: mieszanie, mieszalnik, przepływ cieczy, symulacje CFD, niecentryczność mieszadła

DOI: 10.4467/2353737XCT.15.109.4057

* Ph.D. Eng. Ryszard Wójtowicz, Institute of Thermal and Process Engineering, Faculty of Mechanical Engineering, Cracow University of Technology.

** Ph.D. Eng. Andrey A. Lipin, Faculty of Chemical Engineering and Cybernetics, Ivanovo State University of Chemistry and Technology, Ivanovo, Russia.

1. Introduction

Mechanically stirred vessels are commonly used in industry for the production of multiphase systems [1, 2]. The choice of a proper configuration of a vessel–impeller set and an optimal geometry of stirring elements is of crucial importance at the design stage. It directly influences the course of a process and power consumption.

In industrial practice, multiphase systems are most frequently produced using classic stirred vessels, which have a flat or elliptical bottom, and additional baffles. The role of baffles is the partial elimination of an excessive liquid rotation that is unproductive for the process. Moreover, baffles counteract central vortex formation that destabilises phases dispersion by – often unfavourable – gassing of the liquid. Baffles differ by construction, length and location inside a stirred vessel.

Alternative designs for stirred vessels with baffles include unbaffled reactors. Their impellers should not be positioned along the tank axis (which results in whole volume liquid rotation), but they should have a certain eccentricity, obtained by moving the impeller shaft towards the tank wall. Impeller displacement changes the flow pattern in the vessel. Distinct, asymmetric circulation loops are inducted, different liquid flow is observed also in the impeller discharge stream.

The influence of an eccentrically positioned impeller on stirred vessel performance was the focus of investigations conducted by a number of researches. The effect of impeller eccentricity on mixing time, power consumption and results of phase dispersion was reported in [3–11]. Experiments were conducted for a laminar and transient flow regimes [5, 6], at various power input levels. Scholars used one or two impellers, located in the same shaft as well as up-pumping or down-pumping pitched blade turbines [5–7].

Local momentum-transfer coefficients [7] or convective heat-transfer coefficients [8] were determined empirically, for different scale reactors with non-standard impellers, of various dimensions [9, 10].

Little attention was focused on the influence of eccentricity of an impeller on the changes of flow circulation generated in a stirred vessel. Only few scholars [9, 11] presented preliminary and fragmentary results of such experiments, obtained usually on the basis of complex, expensive and labor-consuming methods, e.g. PIV or LDA anemometry.

2. Experimental

The stirred vessel used in the numerical investigations is shown in Figure 1. It consisted of an unbaffled cylindrical tank 1 (internal diameter D = 0.286 m) with a flat bottom, and a single, high-speed impeller 2 located inside of the tank. Two different types of turbine impellers were examined: the standard *Rushton* turbine (Fig. 1b), generating radial circulation and the down-pumping pitched blade turbine (blade angle α = 45°) (Fig. 1c), inducing axial flow. The impellers had the same diameter $d = D/3$ and the impeller off-bottom clearance was set at $h = d$. The impellers rotated clockwise at n = 300 [1/min], in a range of fully turbulent flows ($\mathrm{Re}_m \approx 4.5 \cdot 10^4$).

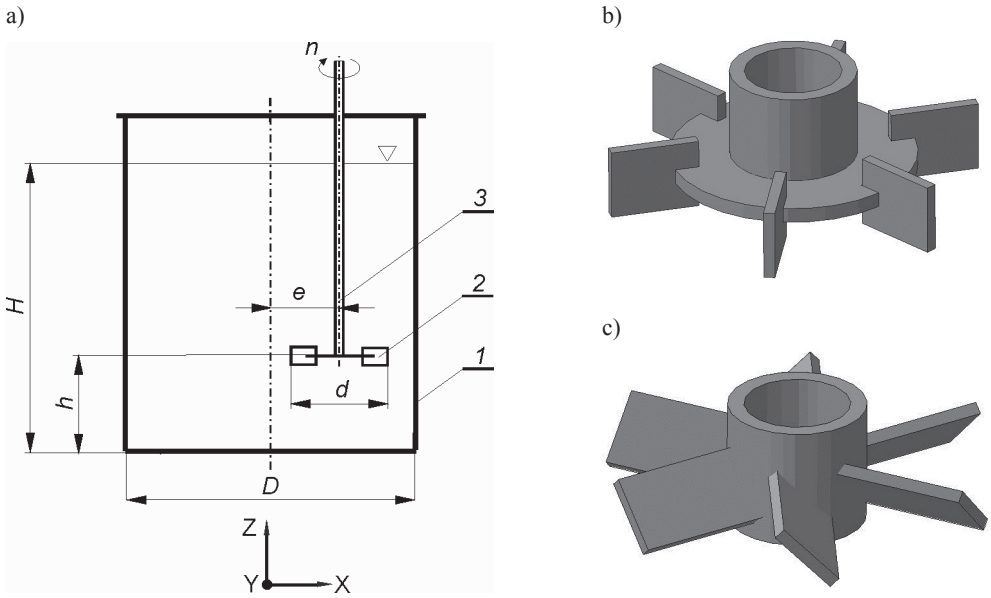

Fig. 1. Stirred vessel with an eccentrically positioned impeller; a) stirred vessel geometry: 1 – cylindrical tank, 2 – impeller, 3 – shaft, b) *Rushton* turbine, c) down-pumping pitched blade turbine (α = 45°)

Distilled water (ρ = 998 kg/m^3, η = 0.001 Pa·s (at 20°C)) was taken as the tested liquid. The liquid height for all simulations was set at $H = D$. Impellers were located in three, different positions inside of the tank. Their distances from the tank axis were e=0 (central position, along the tank axis), $e = 0{,}25R$ and $e = 0{,}5R$, where R is the tank radius.

Flow identification in a stirred vessel was carried out based on the results of numerical modeling. A popular mesh generator *GAMBIT 2.4* was used as the preprocessor (model geometry creation, mesh generation, boundary conditions selection). For all tested stirred vessels an unstructural numerical mesh consisting of approximately $7.5 \cdot 10^5$ tetrahedral cells was generated. The model equations were solved using a numerical solver *FLUENT 6.3.26* and the finite volume (FV) method. The movement of an impeller was modeled with the multiple reference frames (MRF) mode. For mathematical description of the turbulent liquid flow in a stirred vessel the standard *Navier – Stokes* equations were averaged using the *Reynolds* averaging (RANS) approach [12]. Modelling of turbulence was carried out using – recommended for stirred vessels [13] – the *Realizable k–*ε turbulence model with the standard wall functions. Computations were carried out until the normalised sum of residuals fell below 10^{-5}.

3. Results and discussion

Figure 2 shows vector maps of liquid flow obtained for unbaffled stirred vessels with *Rushton* turbine. As seen in Fig. 2, this impeller generates various flow circulations in the

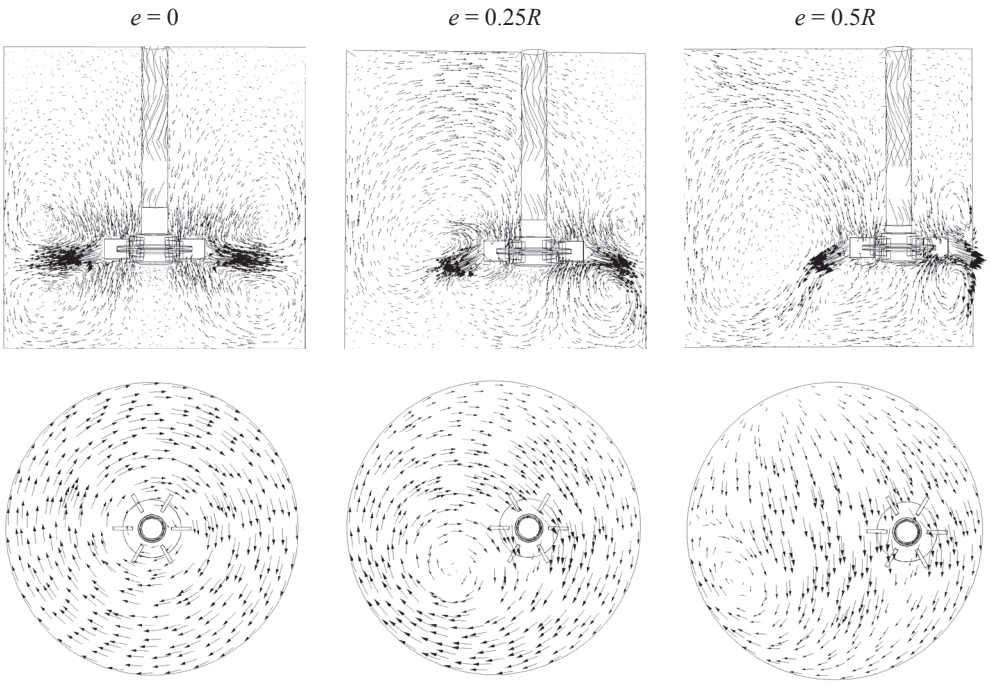

Fig. 2. Vector maps of liquid flow in a stirred vessel with an eccentrically positioned *Rushton* turbine: vertical cross-section plane (top row); horizontal cross-section plane on the liquid free-surface (bottom row)

vessels, depending on its eccentricity. When the impeller is located at the tank axis ($e = 0$), the liquid flow is symmetric with visible radial impeller discharge streams towards tank walls. The most intensive flow is observed at the impeller level, with two, independent circulation loops above and below the impeller. Insignificant displacement of shaft towards tank wall ($e = 0.25R$) causes changes in circulation. The flow becomes unsymmetrical and the main liquid stream is deflected to the bottom, as was the case for axial impellers. Circulation loops are deformed. For the most eccentricity ($e = 0.5R$), a large, distinct loop behind an impeller is generated, as well as small ones in the gap between the impeller and tank wall.

Interesting observations were made on the basis of analysis of liquid free-surface. As shown in Figure 2 (bottom row), the impeller displacement causes an introduction of an additional large-scale vortex, which is a circular ($e = 0.25R$) or elliptical in shape ($e = 0.5R$), and located opposite to impeller.

For precise and exact analysis of this phenomenon, the Q-criterion [14] was used. The criterion is defined by:

$$Q = \frac{1}{2}\left[\left|\Omega\right|^2 - \left|S\right|^2\right] > 0 \tag{1}$$

where:

S – is the rate-of-strain tensor,

Ω – is the vorticity tensor.

It is used to identify the location of vortex cores in the whole (3D) volume of a stirred vessel. Sample iso-surfaces of Q-criterion determined for the stirred vessel with *Rushton* turbine are presented in Fig. 3.

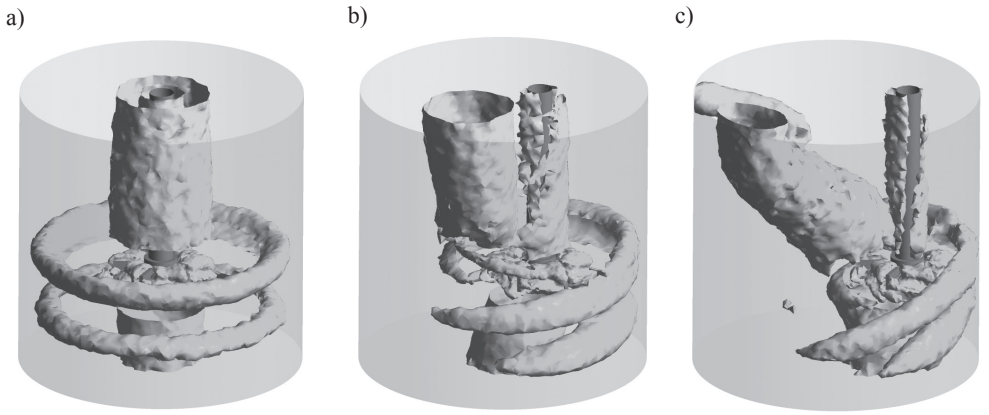

Fig. 3. Iso-surfaces of Q-criterion for stirred vessel with *Rushton* turbine a) $e = 0$, b) $e = 0.25R$, c) $e = 0.5R$ ($Q = 15$ [s^{-2}])

The visualizations presented above confirm the tendencies described above. First of all, the rotation of the whole liquid volume in the stirred vessel with a centrally positioned impeller (Fig. 3a). At this impeller location we can see a large-scale vortex around the shaft and under the impeller, as well as ring vortex cores representing circulation loops. Meanwhile, for eccentrically positioned impellers, a large-scale vortex involving the region from the free-surface to the impeller zone is seen (Fig. 3b, c). Smaller scale, unsymmetrical vortices are seen in zones around the impeller with irregular vortical structures behind the blades.

Somewhat different changes in flow circulation were observed for a stirred vessel equipped with an axial impeller, the pitched blade turbine. In this case, for impeller location at the tank axis (Fig. 4 $e = 0$), it generates symmetrical axial flow with shaped circulation loops; impeller discharge streams are inclined towards the tank bottom. The eccentricity of impeller (Fig. 4 $e = 0.25R$, $e = 0.5R$) changes a flow regime. An intensive liquid circulation is observed in the top (above impeller) part of the vessel, with small vortices generated under the impeller. The above changes in flow circulation confirmed visualizations presented in Fig. 5. As with the radial impeller, the eccentrically located pitched blade turbine induces a large-scale vortex in the opposite part of the vessel. An interesting vortex formation is observed for eccentricity $e = 0.5R$ (Fig. 5 $e = 0.5R$). In this case, at the top part of the tank, the main vortex splits into two smaller ones and one of them is directed not to free-surface but to the tank wall.

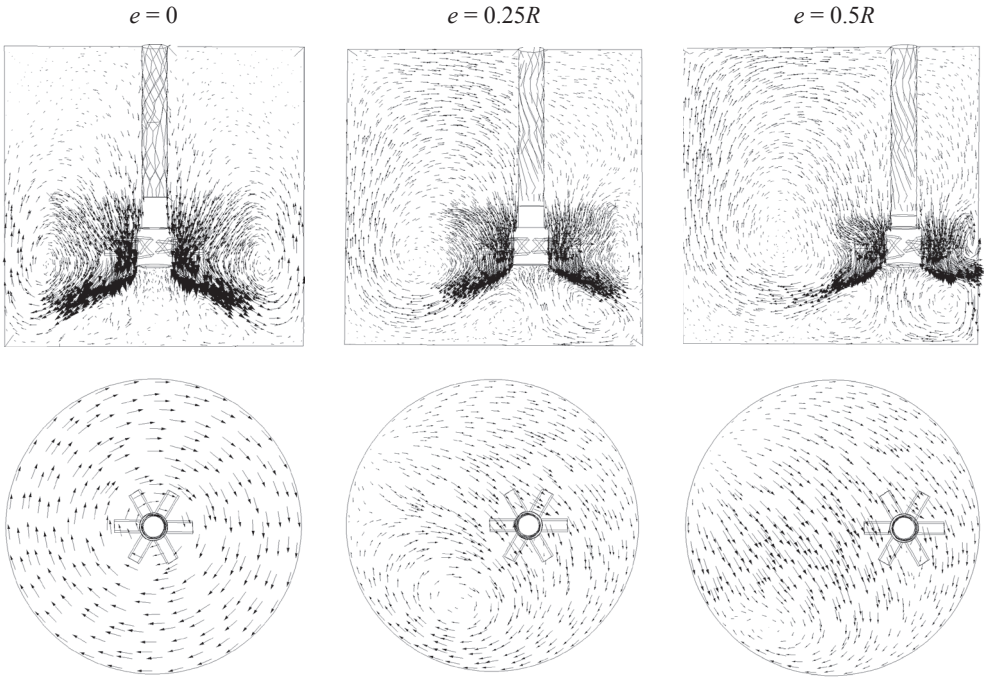

Fig. 4. Vector maps of liquid flow in a stirred vessel with an eccentrically positioned pitched blade turbine: vertical cross-section plane (top row); horizontal cross-section plane on the liquid free-surface (bottom row)

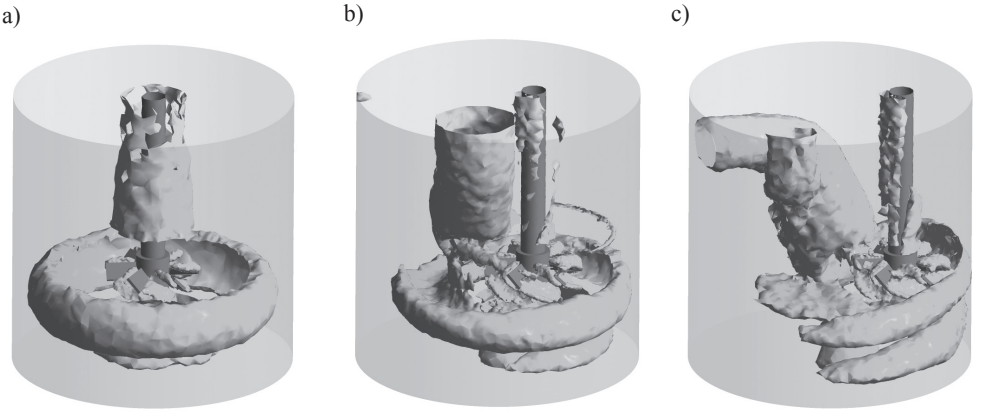

Fig. 5. Iso-surfaces of Q-criterion for stirred vessel with pitched blade turbine a) $e = 0$, b) $e = 0.25R$, c) $e = 0.5R$ ($Q = 10$ [s^{-2}])

During the numerical simulations, the influence of an impeller eccentricity on the turbulence of liquid flow in stirred vessels was also analysed. Turbulence intensity is the main parameter for which comparative analysis was carried out. It is defined as the ratio of the magnitude of *RMS* turbulent fluctuations to the impeller tip speed ($u_{tip} = 2\pi n$):

$$I = \frac{\sqrt{\frac{2}{3}k}}{u_{tip}} \tag{2}$$

where k represents the turbulence kinetic energy.

Simulation results are presented in Table 1 and Figure 6. For comparison purposes, contour maps were drawn in the same scale.

Table 1

The general range of turbulence intensity *I* [%] for liquid flow in investigated stirred vessels

Impeller/ eccentricity	*Rushton* turbine			Pitched blade turbine		
	$e = 0$	$e = 0.25R$	$e = 0.5R$	$e = 0$	$e = 0.25R$	$e = 0.5R$
Turbulence intensity *I* [%]	2.2–35.9	1.9–37.8	1.8–36.2	1.6–15.9	1.5–23.1	1.6–22.1

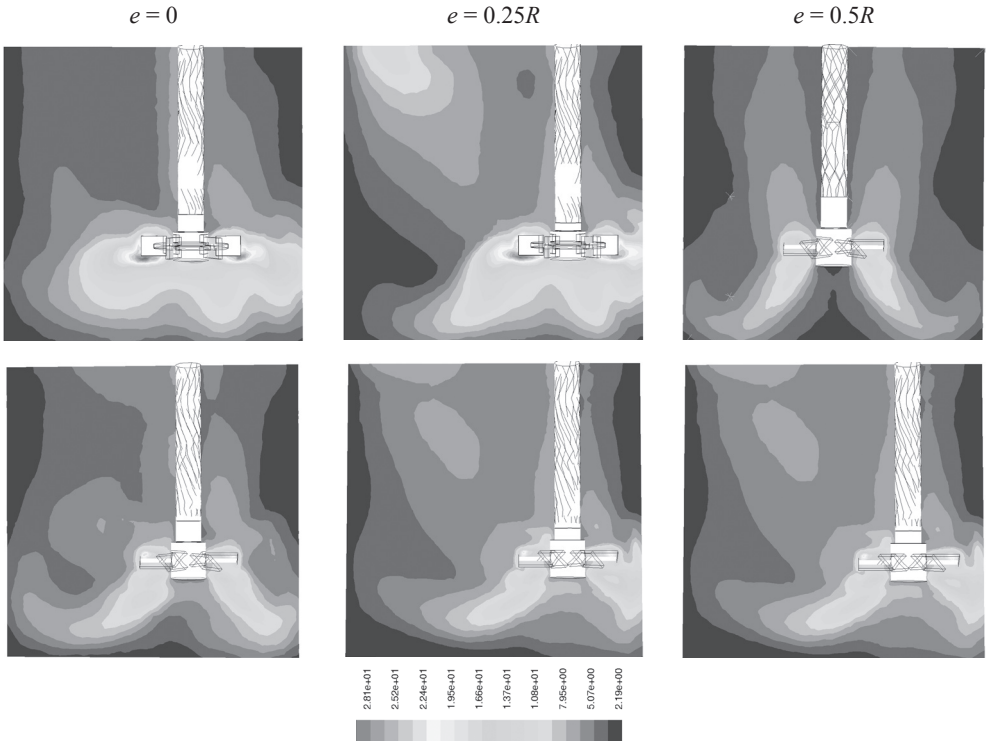

Fig. 6. Contour maps of turbulence intensity *I* [%] obtained for investigated stirred vessels: *Rushton* turbine (top row), pitched blade turbine (bottom row)

The presented maps confirm a significant influence of the impeller location on the liquid flow turbulence inside a stirred vessel. The maximum values of turbulence intensity are observed in the vicinity of impeller blades, regardless of impeller type and its location in the vessel. Larger (even about two times) maximum values are seen for the radial impeller (*Rushton* turbine) (see Table.1), it confirms – well known [1, 2] – high operating efficiency of this kind of an impeller.

For both cases, the impeller eccentricity does not change turbulence conditions in the impeller zone essentially, but the flow patterns in the whole vessel are different. In the case of the *Rushton* turbine, an impeller displacement disturbs flow symmetry and narrows down zones of intensive turbulence. We can see a relatively broad zone of low turbulence even at the impeller level (Fig. 6 $e = 0.5R$ RT).

For a pitched blade turbine, the regions of intensive flow close to the impeller have – in comparison with *Rushton* turbine – a smaller area, but impeller displacement intensifies flow in the whole vessel, including the zone under the impeller (Fig. 6 $e = 0.5R$ PBT). For both impellers, the maximum impeller eccentricity causes more intensive flow close to the free-surface (large-scale vortex formation).

An important quantity, characterizing the mixing processes is the *Newton* number. It is useful for the estimation of the power consumption and also for the strength calculations of mixing vessel elements, e.g. shaft dimension, impeller design etc. For mixing, this criteria number is defined as:

$$\mathrm{Ne}_m = \frac{P}{n^3 d^5 \rho} \tag{3}$$

where P is the power delivered to the liquid by an impeller, calculated as a product of the impeller tip speed ($u_{tip} = 2\pi n$) and torque M:

$$P = 2\pi n M \tag{4}$$

For simulations, the torque values were calculated by integration of the pressure on the impeller blade.

The *Newton* numbers values determined numerically for the stirred vessels are presented in Table 2 and Figure 7.

Table 2

The *Newton* number values determined in numerical simulations

Impeller/ eccentricity	*Rushton* turbine			Pitched blade turbine		
	$e = 0$	$e = 0.25R$	$e = 0.5R$	$e = 0$	$e = 0.25R$	$e = 0.5R$
Newton number Ne_m	2.64	2.95	3.03	1.24	1.37	1.45

As can be seen, an increase of impeller eccentricity causes a slight increase of *Newton* number values. This tendency was observed for both radial and axial impellers. A displacement

of an impeller in a vessel from the central axis causes deformation of originally symmetric flow field and generates nonstationary vortices whose core location depend on eccentricity value. As a result, mixing power also tends to increase. A similar conclusion was drawn and described elsewhere, e.g. in [3].

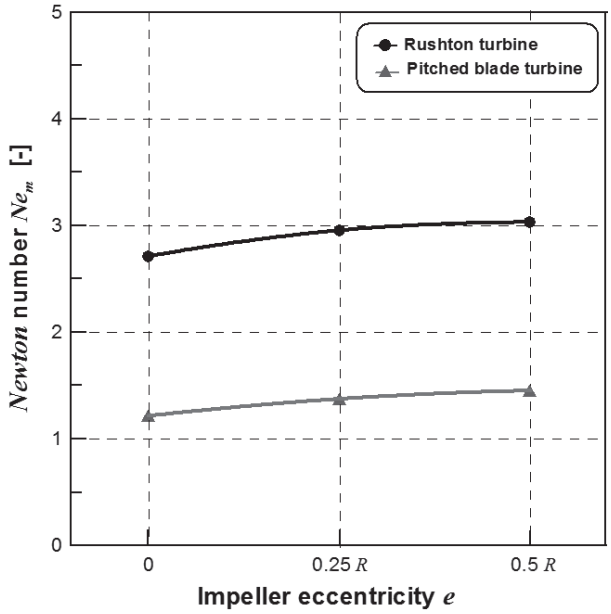

Fig. 7. The values of *Newton* number determined on the basis of simulations for various impeller eccentricity

The presented study is the first part of research into dispersion of multiphase systems in stirred vessels with eccentrically positioned impeller. Therefore, the results mainly have a descriptive and qualitative form. In next stages of investigations, CFD simulations will be verified and validated by means of LDA measurements. It will give the complete quantitative and qualitative description of a mixing process conducted in this kind of mixing equipment.

References

[1] Paul E.L., Atiemo-Obeng W.A., Kresta S.M., *Handbook of Industrial Mixing*, Wiley & Sons Inc., New Jersey 2004.
[2] Kamieński J., *Mixing of multiphase systems*, WNT, Warszawa 2004 (in Polish).
[3] Dyląg M., *Analysis of selected issues of a stirred vessel performance during dispersed systems formation*, Cracow University of Technology, Cracow 1979.
[4] Nishikawa M., Ashiwake K., Hashimoto N., Nagata S., *Agitation power and mixing time in off-centering mixing*, International Chemical Engineering, 19, 1979, 153–160.

[5] Woziwodzki S., Jędrzejczak Ł., *Effect of eccentricity on laminar mixing in vessel stirred by double turbine impellers*, Chemical Engineering Research and Design, 89, 2011, 2268–2278.
[6] Woziwodzki S., Broniarz-Press L., Ochowiak M., *Effect of eccentricity on transitional mixing in vessel equipped with turbine impellers*, Chemical Engineering Research and Design, 88, 2010, 1607–1614.
[7] Cudak M., Karcz J., *Momentum transfer in an agitated vessel equipped with an eccentrically located HE 3 impeller*, Chemical and Process Engineering, 29, 2008, 1071–1082.
[8] Karcz J., Cudak M., *An effect of the type of an eccentrically located impeller on the efficiency of heat transfer process*, 12th European Conference on Mixing, Bologna 2006, 727–734.
[9] Hall J.F., Barigou M., Simmons M.J.H., Stitt E.H., *Comparative study of different mixing strategies in small high throughput experimentation reactors*, Chemical Engineering Science, 60, 2005, 2355–2368.
[10] Galletti C., Pintus S., Brunazzi E., *Effect of shaft eccentricity and impeller blade thickness on the vortices features in an unbaffled vessel*, Chemical Engineering Research and Design, 87, 2009, 391–400.
[11] Montante G., Bakker A., Paglianti A., Magelli F., *Effect of the shaft eccentricity on the hydrodynamics of unbaffled stirred tanks*, Chemical Engineering Science, 61, 2006, 2807–2814.
[12] Jaworski Z., *Computational fluid dynamic in chemical and process engineering*, EXIT, Warszawa 2005 (in Polish).
[13] Marshall E.M., Bakker A., *Computational fluid mixing*, Fluent Inc, Lebanon 2002.
[14] Hunt J.C.R., Wray A.A., Moin P., *Eddies, streams and convergence zones in turbulent flow*, CTR-S88, 1988, 193–208.

CONTENTS

M. G w a d e r a, K. K u p i e c: Modeling of adsorption in a mixing tank 3
M. G w a d e r a, K. K u p i e c, A. M a r s z a ł e k: On adsorption of water vapor on silica gel 17
J. J a ś k o w s k a, K. C h o r a b i k, Z. M a j k a: Efficient methods for synthesis of florol and its derivatives..... 29
A. K o z a k, M. B o n o p e r a: Performance analysis of reinforced polymer cement mortars "RPCMs" used for repairing concrete structures..... 37
M. K u r a ń s k a, A. P r o c i a k: Flax fibers as natural filler for rigid polyurethane--polyisocyanurate foams based on bio-polyol from rapeseed oil 47
B. L a r w a, K. K u p i e c, T. K o m o r o w i c z, K. N e u p a u e r: Heat conduction in the ground under natural conditions and with heat exchanger installed 55
H. M a c h o w s k a: Power industry – coal ecology..... 69
E. M a l e w s k a, A. P r o c i a k: Modification of expandable polystyrene beads 77
K. P l u t a, D. M a l i n a, A. S o b c z a k - K u p i e c: Scaffolds for tissue engineering..... 89
R. W ó j t o w i c z, A.A. L i p i n: The computational-fluid-dynamics study of an unbaffled stirred vessel with eccentrically positioned impeller..... 99

TREŚĆ

M. G w a d e r a, K. K u p i e c: Modelowanie adsorpcji w zbiorniku z mieszaniem 3
M. G w a d e r a, K. K u p i e c, A. M a r s z a ł e k: Badanie adsorpcji pary wodnej na silikażelu 17
J. J a ś k o w s k a, K. C h o r a b i k, Z. M a j k a: Opracowanie wydajnej metody syntezy florolu i jego pochodnych..... 29
A. K o z a k, M. B o n o p e r a: Analiza porównawcza zapraw cementowo-polimerowych stosowanych do naprawy betonu 37
M. K u r a ń s k a, A. P r o c i a k: Włókna lniane jako naturalny napełniacz do sztywnych pianek poliuretanowo-poliizocyjanurowych z udziałem bio-poliolu z oleju rzepakowego..... 47
B. L a r w a, K. K u p i e c, T. K o m o r o w i c z, K. N e u p a u e r: Przewodzenie ciepła w gruncie w warunkach naturalnych i przy zainstalowanym wymienniku ciepła 55
H. M a c h o w s k a: Energetyka – węgiel-ekologia 69
E. M a l e w s k a, A. P r o c i a k: Modyfikacja perełek ekspandowanego polistyrenu 77
K. P l u t a, D. M a l i n a, A. S o b c z a k - K u p i e c: Rusztowania kostne dla inżynierii tkankowej..... 89
R. W ó j t o w i c z, A.A. L i p i n: Symulacje CFD mieszalnika bez przegród z niecentrycznie sytuowanym mieszadłem..... 99